Summer 2019

Non-invasive microwave and millimeter wave reflectometry and imaging for human skin diagnosis and materials characterization

Yuan Gao

Department: Electrical and Computer Engineering

NON-INVASIVE MICROWAVE AND MILLIMETER WAVE REFLECTOMETRY AND IMAGING FOR HUMAN SKIN DIAGNOSIS AND MATERIALS CHARACTERIZATION

by

YUAN GAO

A DISSERTATION

Presented to the Faculty of the Graduate School of the

MISSOURI UNIVERSITY OF SCIENCE AND TECHNOLOGY

In Partial Fulfillment of the Requirements for the Degree

DOCTOR OF PHILOSOPHY

in

ELECTRICAL ENGINEERING

2019

Approved by:

Dr. Reza Zoughi, Advisor
Dr. Mohammad Ghasr
Dr. Kristen Donnell
Dr. R. Joe Stanley
Dr. Daryl Beetner
Dr. Julie Semon

PUBLICATION DISSERTATION OPTION

This dissertation consists of the following four articles, formatted in the style used by the Missouri University of Science and Technology:

Paper I: Pages 10-37, Y. Gao, R. Zoughi, “Millimeter wave reflectometry and imaging for noninvasive diagnosis of skin burn injuries”, has been published in IEEE Transactions on Instrumentation and Measurement, vol. 66, no. 1, pp. 77-84, 2017.

Paper II: Pages 38-82, Y. Gao, M. T. Ghasr, M. Nacy, R. Zoughi, “Towards Accurate and wideband *in vivo* measurement of skin dielectric properties”, has been published in IEEE Transactions on Instrumentation and Measurement, vol. 68, no. 2, pp. 512-524, 2018.

Paper III: Pages 83-109, Y. Gao, M. T. Ghasr, R. Zoughi, “Effects of and compensation for translational position error in microwave synthetic aperture radar imaging systems”, has been accepted by IEEE Transactions on Instrumentation and Measurement.

Paper IV: Pages 110-142, Y. Gao, M. T. Ghasr, R. Zoughi, “Complex permittivity extraction from synthetic aperture radar (SAR) images”, has been submitted to IEEE Transactions on Instrumentation and Measurement.

ABSTRACT

Microwave and millimeter wave reflectometry and synthetic aperture radar (SAR) imaging techniques have been successfully applied in many applications, such as nondestructive testing and evaluation (NDT&E), security inspection and medical diagnosis. In this dissertation, the feasibility of using microwave and millimeter reflectometry and SAR imaging for burn diagnosis is investigated through both simulations and measurements, with promising results. To correctly model the interaction between electromagnetic waves and skin, the proper knowledge of the complex permittivity of healthy skin is critically important. To this end, the common used measurement methods for *in vivo* skin complex permittivity are reviewed and analyzed in this study, subsequent to which a more accurate method is proposed and verified. Furthermore, when applying SAR imaging algorithm with handheld or high-frequency imaging systems, the translational position error can lead to significant image quality degradation. A comprehensive approach is proposed for analyzing this problem, resulting in an effective position error compensation method. Although SAR imaging is an effective tool for nondestructive testing and diagnosis, the imaging results only show the reflectivity contrast in a material-under-test, and does not give information about the absolute complex permittivity. Thus, the SAR imaging technique can only be used as a qualitative evaluation tool. To overcome this limitation, a novel approach is proposed to extract complex permittivity from SAR images. The simulation and measurement results show the validity and effectiveness the proposed method. In addition, the proposed method also shows its capability of detecting local inhomogeneity.

ACKNOWLEDGMENTS

First and foremost, I want to express my sincere appreciation to my advisor, Dr. Reza Zoughi, for his guidance, support and encouragement. I am always inspired by his passion and insight.

I would also like to thank Dr. Mohammad Tayeb Ghasr, Dr. Kristen M. Donnell, Dr. Joe Stanley, Dr. Daryl Beetner and Dr. Julie Semon for serving on my committee. Special thanks to Dr. Mohammad Tayeb Ghasr for his help and mentorship during my Ph.D. work.

I would like to thank all my friends and colleagues at Missouri S&T for their help.

I would like to acknowledge the IEEE Instrumentation and Measurement Society for the partial financial support of my Ph.D. work under a 2016 Graduate Research Fellowship.

Last, but not least, I would like to thank my parents for their love and support.

TABLE OF CONTENTS

LIST OF ILLUSTRATIONS

PAPER I Page

PAPER II

PAPER III

PAPER IV

LIST OF TABLES

SECTION

1. INTRODUCTION

1.1. BACKGROUND AND MOTIVATIONS

Skin is the largest organ in human body, and it regulates body temperature and moisture and protects human body from environment. However, skin is susceptible to disease and injuries, such as burn, which is a very common injury. Burn causes ~265,000 deaths globally and more than ~3000 death in US every year [1]. In addition, the estimated annual number of burn injuries receiving medical treatment is ~486,000 in US [2]. Accurate diagnosis of skin burn, particularly in the early stage, can result in a more efficient and reasonable treatment, better pain management and significant reduction in severe scarring. Close estimation of burn degree (i.e., depth of invasion) is a critical issue in burn diagnosis and treatment. Currently, this diagnosis is primarily performed on the basis of a physician's visual assessment of the burn injury. However, visual diagnosis is inaccurate and subjective, and can result in misdiagnosis. The accuracy of clinical visual observation is only ~64%-76% for experienced surgeons and may decrease as low as ~50% for inexperienced surgeons [3]. In addition, misdiagnosis from visual inspection commonly results in overestimating the degree of burn, which may lead to unnecessary excision [4]. Consequently, many researchers have attempted to devise objective diagnostic methods, such as thermography, photometry and laser Doppler imaging, each with its own advantages and disadvantages [3]. Recent investigations also show tremendous potential for skin burn diagnosis using microwave and millimeter wave reflectometry and imaging

techniques [5]-[7]. However, more efforts are still needed to determine the optimal modality for skin burn diagnosis.

Since microwaves and millimeter waves are sensitive to the change of complex permittivity of biological tissues, and the fact that these high frequency signals are significantly affected by the presence of water, causes the water content difference between the healthy skin and the much drier burned skin results in significant differences in their respective dielectric and reflection properties. Moreover, these high frequency signals can interact with different layers of skin, but do not penetrate beyond the subcutaneous fat layer [5]. This advantage ensures that the signal interference from tissues below the subcutaneous fat is minimized. Additionally, high frequency microwave and millimeter wave signals can readily penetrate medical dressing and provide diagnostics capability without the need for removing them. Thus, high frequency microwave and millimeter wave techniques have the potential for becoming effective tools for evaluating skin burn injuries. However, research and applications for millimeter waves for burn diagnosis have been very limited so far, but with encouraging results [6]-[7].

For the purposes of skin burn diagnosis with high frequency and millimeter wave techniques, proper knowledge of the electromagnetic properties of skin, primarily its complex permittivity, is critically important, since changes in this parameter are closely related to changes in its biophysical properties, especially its water content. Currently, the most commonly used method for *in vivo* skin complex permittivity measurement is reflectometry [8]-[9]. This involves measuring the reflection coefficient of skin, in contact with an open-ended coaxial or a rectangular waveguide probe. Subsequently, the measured reflection coefficient is used, in conjunction with an electromagnetic model that describes

the measurement environment, to extract the complex permittivity. For accurately modeling the interaction of the skin with electromagnetic wave, proper skin models must be considered. Usually, a simplified homogenous model is assumed for skin, but it is not appropriate for locations with thick stratum corneum (SC) layer. Moreover, the admittance model used in coaxial probe method is not applicable for multilayer skin model. Thus, when localized open-ended coaxial probe reflectometry method is applied on locations with SC layer, the calculated complex permittivity is generally lower than expected [9]-[11]. In addition, calibration of an open-ended coaxial probe for measuring reflection coefficient of non-liquid material is not a straightforward process, and any error due to calibration can significantly and adversely affect the measurement results [12]. All aforementioned issues limit the application of open-ended coaxial probe for a general multilayer skin model. To this end, to properly model the interaction between open-ended coaxial probe and layered skin structure (i.e. a wave propagation model with multilayer structure) is needed, such as the one developed in [13]. Unfortunately, to-date no such effort has been reported for determining skin complex permittivity.

On the other hand, open-ended waveguide probe method has also been used as an effective tool to obtain thickness and complex permittivity of layered dielectric materials [14]. Many papers in the published literature report the results of skin complex permittivity accomplished with open-ended waveguide probe method [8] [15]-[18]. In these studies, the distribution of electric field at the waveguide aperture is usually wrongly assumed as transverse electromagnetic wave or waveguide dominant mode, and the effects of finite-size flange are also neglected in these investigations. That is to say that these assumptions: i) do not properly account for the complex interaction of electromagnetic fields in the near-

field of a waveguide probe with a layered skin structure, ii) they ignore the ever-important presence of higher-order modes that are generated at the aperture, and iii) they ignore the multiple reflection from flange edges. In addition, because of the soft nature of skin tissue, applied pressure can cause tissue protrusion into the waveguide aperture. Several solutions have been proposed to overcome this critical pressure issue, such as using a plug at the waveguide aperture [15] [18]. However, the effect of the plug is usually not properly accounted for in these investigations. All aforementioned issues result in errors in the measured reflection coefficient, and hence in the calculated complex permittivity.

To summarize, the currently used open-ended coaxial and waveguide probe methods have their respective limitations and approximations that affect the calculation accuracy of complex permittivity of skin to varying degrees. Unfortunately, the influence of these limitations and approximations on calculation results of complex permittivity is seldom accounted for or discussed. Therefore, a more robust and accurate measurement methodology with a comprehensive discussion of calculation accuracy is desired.

Although high frequency reflectometry is a promising approach for non-invasive skin burn diagnosis, the measurement conducted in contact fashion is painful, in most cases impossible and not an optimal solution. An alternative contactless diagnosis method is high-resolution millimeter wave imaging. One of the millimeter wave imaging method that is deemed suitable for this purpose is synthetic aperture radar (SAR) imaging, it has the advantages of producing high resolution 3D images in real-time and in a computationally efficient manner. This imaging approach has been successfully applied for many nondestructive and security applications, such as nondestructive testing and evaluation (NDT&E) inspection [19]-[20]. A typical SAR imaging system uses a transceiver scanning

(mechanically or electronically) over the material under test (MUT) on a two-dimensional plane to collect effective reflection coefficient. Then the collected data is processed by the SAR imaging algorithm to produce a high-resolution image. The resulting image presents the contrast in the effective reflectivity of the imaged MUT, which is directly related to its complex permittivity. Usually, such imaging systems have very good positional accuracies since high-precision positioning mechanisms are employed for mechanical raster scanning systems. However, when operating in the millimeter wave frequency range or when manually scan is performed, then the positioning error (difference between assumed and actual transceiver locations) could be significant and must be analyzed to determine the minimum requirement for location accuracy and the resulting level of image quality degradation. As will be discussed later, position error can cause incorrect phase compensation in the SAR imaging algorithm, thereby leading to image quality degradation primarily in the form of an unfocused image, similar to the error associated with imaging platform trajectories in remote sensing application [21]-[22]. However, if the synthetic aperture with limited size is close to the MUT (i.e., a few wavelengths away), the position error can lead to a more severe image distortion for the same level of position error. Thus, a general methodology for quantitatively evaluating the effects of translational position error on a microwave and millimeter wave SAR imaging system is desired. More importantly, an effective compensation method for position error is needed for improving the performance of SAR imaging systems. This analysis methodology and compensation method will also benefit applications using small unmanned aerial vehicle (UAV) for SAR imaging. In these systems, the position error could become a significant bottleneck. For instance, the position error need to be at centimeter or millimeter scale to enable using

UAV imaging systems in conjunction with a ground penetrating radar (GPR) operating at 3.1-5.1 GHz (center frequency wavelength of ~73 mm) for NDT&E applications [23].

SAR imaging method is computationally efficient and can be implemented on real-time basis rendering high-resolution three-dimensional images, but SAR imaging results (i.e., the complex image value) do not provide the distribution of complex permittivity in MUT. Thus, SAR imaging method is commonly used for qualitative evaluation of a scene/MUT. On the other hand, quantitative imaging methods aim to solve for the complex permittivity distribution of the target are available as well, and often referred as inverse imaging [24]. However, these methods require solving a complicated inverse problem and necessitate extensive computational resources. Therefore, it is highly desirable to have a technique that can combine the accuracy and efficacy of both the imaging methods. A possible solution is that firstly generating the high-resolution image using SAR imaging algorithm and then extract the complex permittivity distribution from SAR images. In this way, the high-resolution distribution of complex permittivity can be achieved with less computational resource. This method is applicable for quantitative skin diagnosis and also a general approach suitable for material characterization and NDT&E applications. Some preliminary efforts have been expended which show promising results [25]-[26].

1.2. OBJECTIVES AND ORGANIZATION OF THE DISSERTATION

As mentioned above, several issues still need to be investigated for using microwave and millimeter wave for skin diagnosis. To this end, several research objectives are proposed to address these problems:

1. Verify and demonstrate the feasibility of using microwave and millimeter wave reflectometry and imaging techniques for skin burn diagnosis.

2. Review currently available *in vivo* skin complex permittivity measurement methods and results. Analyze the potential error sources and then propose an approach for more accurate *in vivo* skin complex permittivity measurement.

3. Analyze the effect of position error in SAR imaging systems and propose an effective compensation method for position error.

4. Propose a method to extract the complex permittivity distribution from microwave and millimeter wave SAR images.

To achieve these above objectives, investigations have been conducted and the results are concluded in the form of four papers in this dissertation and organized as following:

In Paper I, the potential of using localized millimeter wave reflectometry and high-resolution millimeter wave imaging for skin burn diagnosis are shown. Extensive electromagnetic simulations are preformed, at Ka-band (26.5-40 GHz), illustrating the potential for distinguishing among different burn degrees when measuring the complex reflection coefficient of skin with an open-ended rectangular waveguide probe. Similar experiments on a piece of pig skin (porcine) also show the potential for the same. L2-Norm calculations of the simulated reflection coefficient values, in the Ka-band frequency range are performed that show the possibility of using this *metric* as a simple means for distinguishing among different burn degrees both in the presence and absence of medical dressing. Limited measurements on a progressively burned piece of pig skin also closely follow similar results. Finally, the feasibility of high-resolution millimeter wave imaging

is also illustrated by producing several V-band (50-75 GHz) SAR images of a burned pig skin sample with and without medical dressing.

In Paper II, reflectometry-based skin complex permittivity measurement methods are reviewed, indicating their strengths and shortcomings. Subsequently, comprehensive analyses are performed considering important practical issues in open-ended waveguide measurement approach that can significantly and adversely affect complex permittivity calculations, such as aperture field distribution approximation, finite ground plane effects and probe pressure problem. Accordingly, a modified open-end waveguide probe method is proposed to effectively overcome these issues for skin complex permittivity measurement, in conjunction with a full-wave electromagnetic model that properly describes the interaction of the fields at the waveguide aperture with a generally layered structure (i.e., human skin). Extensive analyses are performed to investigate and account for critical sources of error in the proposed measurement method. The discussed error sources include homogenous assumption of skin, effects of addition dielectric layer, instrument noise and (operator) measurement inconsistency. Results show that proposed method can achieve ~85% and ~95% theoretical calculation accuracy for dielectric constant and dielectric loss factor respectively in Ka-band (26.5-40 GHz) skin complex permittivity determination. Using this robust method, skin complex permittivity on multiple body locations of three human subjects are measured and reported. Finally, the effect of thick SC layer in complex permittivity calculation is discussed and a modified method to determine the complex permittivity of layered skin is proposed and verified by simulations.

In Paper III, the effects of translational position error, in particular in the height direction, in microwave SAR imaging system is studied, as the height position error is determined to be the dominant factor of SAR image quality degradation. Three image quality metrics are used to quantify the effects of position error. Subsequently, an extensive set of simulations and measurements are performed. The results show to be in good agreement verifying the effectiveness of the proposed analysis approach. Subsequently, an error compensation method is proposed and verified by both simulation and measurement. The methodology proposed in this study can be used to evaluate the feasibility or help define the required specifications of a microwave SAR imaging system for a specific application.

In Paper IV, a novel method is proposed to extract the complex permittivity distribution from SAR images. The detailed implementation approach is introduced and verified by both simulation and measurement. Extensive electromagnetic simulations are also performed to demonstrate that the proposed method is not sensitive to a particular type of MUT and reference material, and measurement parameter setting. In addition, the capability of proposed method for local defect detection is discussed and verified by measurement.

PAPER

I. MILLIMETER WAVE REFLECTOMETRY AND IMAGING FOR NONINVASIVE DIAGNOSIS OF SKIN BURN INJURIES

ABSTRACT

Accurate assessment of degree of burn in human skin is critically important for burn technicians and physicians when making treatment decisions. Millimeter wave reflectometry and imaging are potential diagnostic tools capable of distinguishing between healthy and burned skin as the dielectric properties of the latter is significantly different from that of the former. In this paper, the commonly-used layered model of human skin is used to simulate the reflection properties of skin with varying degrees of burn, at Ka-band (26.5-40 GHz), to demonstrate the potential for such diagnosis. Measurement of complex reflection coefficient are also conducted on a pig skin with and without medical dressing, which is a close mimic to human skin. Good agreement is obtained, in amplitude and variation trends in the reflection coefficient results, between simulation and measurement results, indicating the potential effectiveness and feasibility of burn degree diagnosis by localized millimeter wave reflectometry and complex reflection coefficient L^2-Norm analysis. Finally, synthetic aperture radar (SAR) imaging technique is used to examine the efficacy of imaging for burn wound at V-band (50-75 GHz). In addition, the effectiveness of localized and imaging methods for evaluating burns covered by medical dressings is also demonstrated.

Index Terms—Electromagnetic measurements; Millimeter wave imaging; Reflectometry; Skin; Medical diagnosis.

1. INTRODUCTION

Burn is a common injury which causes 265,000 deaths globally and more than 3000 deaths in the USA every year. The estimated annual number of injuries receiving medical treatment in the USA is 486,000 [1]-[2]. Accurate diagnosis of burn injuries, particularly early on, can lead to a more efficient treatment, pain management and significant reduction in severe scarring. Close estimation of "depth of invasion" or "burn degree" is a critical issue in burn diagnosis and treatment. Currently, this diagnosis is primarily performed based on a physician's visual assessment of the burn injury. Second column in Table I shows the clinical signs used for visual inspection of different burn degrees [3]-[5]. Visual diagnosis is inaccurate and subjective which can result in misdiagnosis. The accuracy of clinical visual observation is only 64%-76% for experienced surgeons and may decrease to as low as 50% for inexperienced surgeons [6]. Visual diagnosis commonly results in overestimating the degree of a burn, which may lead to unnecessary excision operation [7]. Consequently, many researchers have attempted to devise diagnostic methods that are less subjective, such as: thermography, photometry and laser Doppler imaging each with its own advantages and disadvantages [6].

Since the complex dielectric constant (permittivity and loss factor) of biological tissues, in the millimeter wave frequency range, is dominated by water, the difference between water content of healthy and the much drier burned skin results in significant

differences in their respective reflection properties. Moreover, millimeter wave signals can interact with different layers of skin, but do not penetrate beyond the subcutaneous fat layer, as will be discussed later. This is an advantage of this diagnostics approach since there will be minimal signal interference from tissues beyond the subcutaneous fat. Additionally, millimeter wave signals can readily penetrate medical dressings and provide diagnostics capability without the need for removing them. Thus, millimeter wave reflectometry and imaging have the potential for becoming effective tools for evaluating skin burn injuries, and skin cancer detection [8]-[11]. However, application of millimeter waves for burn diagnosis has been very limited so far, but with encouraging results [11]. Some preliminary research has also been conducted with THz systems [12].

The objective of this investigation has been to demonstrate the efficacy of millimeter wave reflectometry and imaging for human skin burn diagnosis and evaluating degree of burns. First, the electromagnetic model of human skin is constructed as it relates to interaction with millimeter wave signals. Then, a series of electromagnetic simulations are performed, at Ka-band (26.5-40 GHz), to examine the potential for distinguishing among different degrees of burn by studying their reflection coefficient properties. Additionally, measurement of complex reflection coefficient is conducted on burned pig skin samples, a close mimic to human skin, to demonstrate the feasibility of distinguishing between different burn severities by localized millimeter wave reflectometry. Finally, several high-resolution synthetic aperture radar (SAR) images of burned pig skin are produced at V-band (50-75 GHz) to illustrate the potential capability of millimeter imaging to distinguish among different burn levels. The influence of medical dressing, is also electromagnetically simulated and tested.

Table 1. Clinical criteria for different burn degree [3]-[5].

Burn Degree	Clinical Signs *	Burn Depth of Invasion
First Degree	Painful and erythematous, no blister	Epidermis partially destroyed
Superficial Second Degree	Painful and erythematous, blisters, wound is pink, wet and hypersensitive when blister is removed, underlying tissue blanches with pressure	Extends to superficial dermis (papillary layer)
Deep Second Degree	Blisters, wound surface is mottled pink and white and less sensitive, underlying tissue does not blanches with pressure	Extends to deeper regions of dermis (reticular layer)
Third Degree	Brown, black or white, no blister; no sensitivity, do not blanch with pressure	Extends to hypodermis

* Adapted.

2. MODEL OF HUMAN SKIN

2.1. STRUCTURE

The schematic structure of human skin is shown in Fig. 1 consisting of epidermis, dermis and subcutaneous tissue (also referred to as hypodermis) [13]. *Epidermis* is ~0.06-0.1 mm thick and consists of several thinner layers. Its outermost layer, stratum corneum (SC), is ~0.012-0.018 mm thick. The rest of epidermis (called viable epidermis), has a total water content similar to the water content of *dermis* which is ~1.2-2.8 mm thick [14]-[15]. The *subcutaneous tissue* mainly consists of fat.

2.2. SKIN DIELECTRIC PROPERTIES

High frequency complex dielectric constant of materials is represented by its real (i.e., permittivity) and imaginary parts (i.e., loss factor) indicating the ability of the material to store and absorb electromagnetic energy, respectively. When referenced to the permittivity of free-space it is referred to as the relative dielectric constant and denoted by $\varepsilon_r = \varepsilon_r' - j\varepsilon_r''$. The effective dielectric constant of materials, made of a mixture of several different constituents can be closely estimated using effective medium theory (i.e., dielectric mixing formulae) [16]. Among the many and different dielectric mixing formulae, Bruggeman's model is a simple but effective dielectric mixing model for biological tissues [16]-[19].

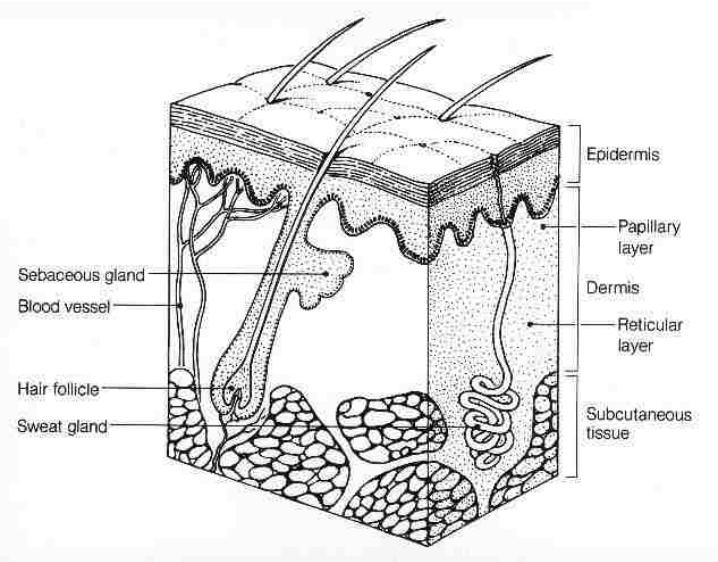

Figure 1. Human skin structure (public domain source: National Cancer Institute, [13]).

Human skin primarily consists of water and biological matter. The former includes free and bound water, but skin permittivity in the millimeter wave frequency band is mainly

determined by free water [14]. The latter, has a low permittivity, low loss and frequency independent dielectric constant [20]. The dielectric constant of bound water is assumed to be similar to the dry biological matter. Then, each layer of skin can be approximated as a binary mixture consisting of free water and dry biological matter. Subsequently, using the aforementioned Bruggeman's dielectric mixing model to estimate the effective dielectric constant of skin layers with different water, results in:

$$(1 - f)\frac{\varepsilon_{rw} - \varepsilon_{reff}}{\varepsilon_{rw} + 2\varepsilon_{reff}} + f\frac{\varepsilon_{rd} - \varepsilon_{reff}}{\varepsilon_{rd} + 2\varepsilon_{reff}} = 0 \quad (1)$$

where f is the volume fraction of biological matter and the equivalent bound water, $(1 - f)$ is the volume fraction of free water, each represented with its respective relative complex dielectric constants of ε_{rd} and ε_{rw} where ε_{reff} represents the relative effective dielectric constant of skin. The dielectric constant of water used here is calculated based on the fully formulated model which is a function of frequency, temperature, etc. [21]. The dielectric constant of dry biological matter is taken to be $\varepsilon_{rd} = 2.5$ [14].

2.3. BURN MODEL

In Jackson's burn model shown in Fig. 2, burn wound is divided into three zones, namely: zone of *coagulation*, zone of *stasis* and zone of *hyperemia* [22]. The coagulation zone is the part in contact or close to the thermal source. The tissue in this part is dead and irreversibly injured. Usually, the burn degree is determined by the depth of coagulation zone [7] [23]. The right column in Table I shows the relationship between burn degree and depth of invasion [3]-[5].

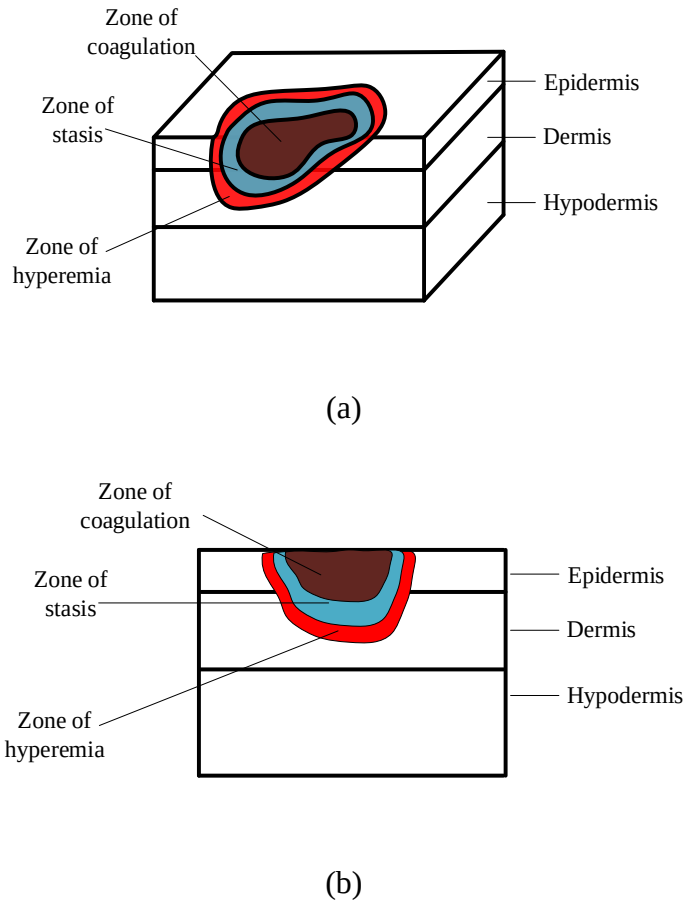

Figure 2. Jackson's burn model: a) perspective view, and b) cross-section view (adapted form [22]).

In the millimeter wave regime, there are two primary approaches for potential evaluation of burn degree, namely: a) localized measurement (using various probes including an open-ended rectangular waveguide [10], [24]) and b) producing high-resolution images of the burned area. In addition, the knowledge gained by the former method can be essential in quantitative interpretation of the results obtained by the latter method, ultimately providing critical information on the capabilities of millimeter wave diagnostics as an effective tool for this purpose.

3. BURN DEGREE DIAGNOSIS BY LOCALIZED MILLIMETER WAVE REFLECTOMETRY

3.1. ELECTROMAGNETIC SIMULATIONS

Open-ended rectangular waveguide probes have shown significant utility in evaluating various geometrical (i.e., thickness) and electrical (i.e., dielectric constant) properties of layered structures [25]. Given that skin is modeled as a layered structure, this probe can be effectively used to evaluate the potential for quantifying different degrees of burn. To evaluate the reflection properties of skin with different degrees of burn, the thickness and dielectric constant of different skin layers must be known or closely estimated as inputs to the model. Fig. 3 shows the schematic of the modeling process employed here. Then, the full-wave electromagnetic analysis method given in [25] is used to simulate a Ka-band (26.5-40 GHz) open-ended rectangular waveguide irradiating into the skin structure. Table II lists the fraction (by weight) of total water, free water and bound water of human palm skin in [14] and gives the equivalent volume fraction of free water shown in parentheses. This number is used as the *average* free water content volume fraction in respective layers, which is 15% free water in SC layer, 45% free water in viable epidermis and dermis, as shown in Fig. 3. Their thickness are set as 0.02 mm, 0.08 mm and 2 mm respectively. The innermost layer is 5 mm of infiltrated fat with its complex dielectric constant (as a function of frequency) given in [26].

According to the definition of coagulation zone, it is reasonable to assume the water content of this zone is lower than that of healthy skin. Therefore, when modeling burned skin in these simulations, volume fraction of free water of the coagulation zone was set at 10%. It must be noted that slightly different values may be used in the model without the

loss of generality for the purpose of detecting burns. Now, different burn degrees can be simulated by replacing layers in the healthy skin (or portions of them) with different coagulation zone thicknesses (i.e., depth of invasion). In the lateral direction the skin model is assumed to be infinite in extent. The dielectric constant of each layer was calculated based on (1) using the respective water contents used for each layer from Table II. The calculated effective relative dielectric constant of skin with different free water content and fat used in the simulations is shown in Fig. 4. Finally, Fig. 5 shows the simulated results for complex reflection coefficient (referenced to the waveguide probe aperture) over the Ka-band frequency range (in polar format). These simulations included all three burn degree scenarios and also different burn levels within the same degree. Two different depths of 1st-degree burn were simulated, namely when: a) the SC is burned (1st-degree *a* in Fig. 5a) and b) the SC and half of viable epidermis is burned (1st-degree *b* in Fig. 5a). 2nd-degree burn was simulated with successive "burning" of dermis with a step size of 1/8 thickness of the dermis (0.25 mm), shown as 2nd-degree *a*-*h*, where *a*-*d* represent superficial 2nd-degree burns (see Fig. 5b) and *e*-*h* represent deep 2nd-degree burn (see Fig. 5c). For the 3rd-degree burn case (see Fig. 5d), the entire epidermis and dermis are assumed burned. In all cases given the high loss factor associated with healthy skin (due to its water content) and fat, the signal is expected not to penetrate beyond the subcutaneous fat layer. This fact was corroborated by using several different fat layer thicknesses ($\geq$2.5 mm), where the simulated reflection coefficient results remained essentially unchanged for all thickness. As will be shown later, similar measurements also corroborated this fact.

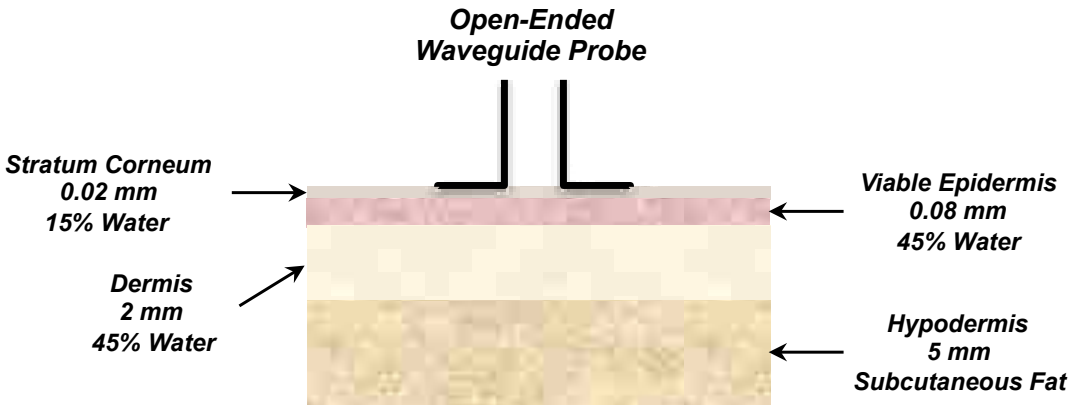

Figure 3. Human skin model used in simulations (not-to-scale).

Table 2. Water content distribution in human palm skin [14].

Skin Layer	Total Water	Free Water	Bound Water
SC	38%-43%	12% (~15%)	26%-31%
Viable Epidermis	65%-70%	39% (~45%)	26%-31%
Dermis	65%-70%	39% (~45%)	26%-31%

Comparing healthy skin complex reflection coefficient with the 1st-degree burn cases in Fig. 5a indicates slight differences, as expected since 1st-degree burn does not significantly alter the skin structure. Fortunately, in practice 1st-degree burn is easy to confirm by visual assessment and it usually heals in 3 to 5 days. For superficial and deep 2nd-degree burn results, shown in Fig. 5b-c, there are clear and substantial differences among different burn depths, by the clear rotation pattern in the complex reflection

coefficient. In clinical diagnosis, distinguishing between these two cases is critically important [6].

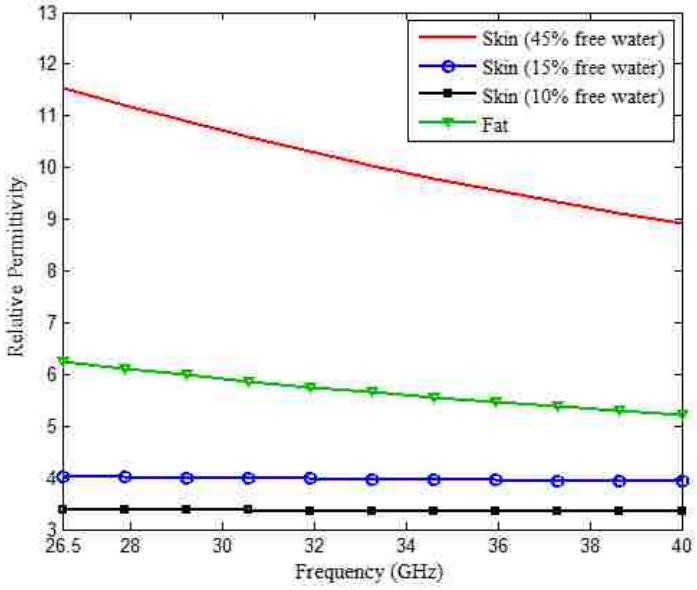

(a)

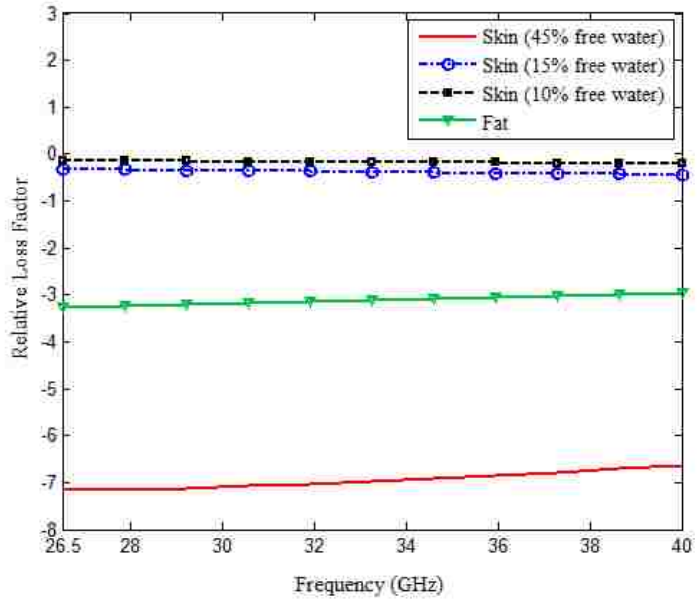

(b)

Figure 4. Calculated effective complex dielectric constant of skin with different water content and fat a) relative permittivity, and b) relative loss factor.

The 3rd-degree burn results (see Fig. 5d) also show significant differences between 3rd-degree burn and the healthy skin (in addition to other burn degrees). Initially, simulations were performed at V-band (50-75 GHz) as well and the results closely followed the trends shown in Fig. 5 [11]. It is worth mentioning that visual inspection can only distinguish among the three different burn degrees with a relatively low level of accuracy (especially for second degree burns). However, these simulation results show the clear potential for distinguishing between superficial and deep 2nd-degree. Also, the substantial difference among the different burn severities, that indicates the promising capability to recognize the variation in severity within a given burn degree.

3.2. PIGSKIN REFLECTION COEFFICIENT MEASUREMENT RESULTS

Pig (porcine) skin is known to be an ideal model for human skin and it is commonly used in burn model research [27]. For these measurements we used pieces of commercially-available pig skin composed of the skin layer (no hair), with an estimated thickness of 2 mm backed by a fat layer with an approximate thickness of 5 mm. Since fire (i.e., flame) burn is the most common burn injury [28], we burned the center of pig skin sample by a small flame torch initially for 10 seconds and successively two more times for 10 additional seconds. The degree of burn could not be exactly established for direct comparison with the simulation results in Fig. 5, in addition to the fact that the moisture content and thickness associated with this skin is not as it would have been on the live animal. Nevertheless, in the absence of measuring this on a live animal, this experiment helps to give a clear indication of the potential for such localized measurements and for evaluating compounding burn episodes. The complex reflection coefficient measurements at the

center of the pig skin sample were conducted using a calibrated Anritsu MS4644A vector network analyzer (VNA), and a modified open-ended rectangular waveguide probe at Ka-band (26.5-40 GHz). The use of modified waveguide flange closely mimics the scenario used for the simulations in which the waveguide flange is assumed infinite in extent (Fig. 3) [29]. Fig. 6 shows the measurement setup and the pig skin sample. During the experiment, the pig skin sample was placed on a uniform plastic sheet to keep it flat. In order to ensure the plastic backing does not contribute to the overall reflection coefficient, measurements were conducted with a metal plate backing as well and the results remained unchanged. This fact also corroborates the simulation results performed as a function of increasing fat layer thickness. As mentioned earlier, the fact that millimeter wave signals do not "see" beyond the subcutaneous fat layer is considered an advantage of this technique since other biological tissues below that layer (i.e., muscle, etc.) do not (or minimally) contribute to the measured reflection coefficient and hence eliminating the need for clutter removal both in these types of measurements and also in the imaging results, as will be shown later.

The average complex reflection coefficient results, of five independent measurements, are shown in Fig. 7, indicating a progressive change as a function of increasing level of burn (i.e., number of seconds burned). Furthermore, the measured results show a similar rotation trend in the complex reflection coefficient to the simulation results, especially to the superficial second degree burn case. These results not only help validate the effectiveness of skin model and but also clearly illustrate the feasibility of burn diagnosis by localized reflection coefficient measurements.

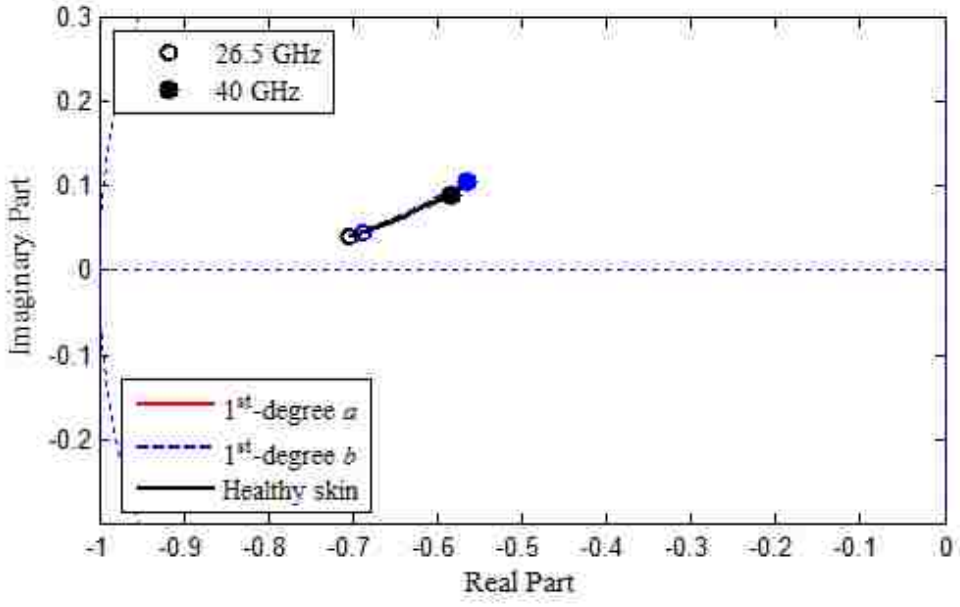

(a)

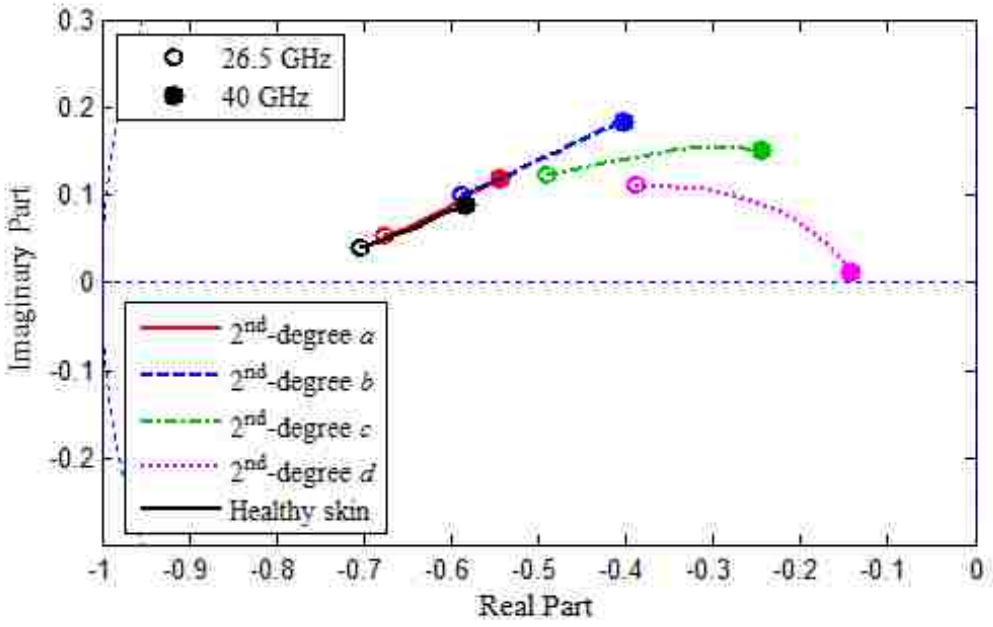

(b)

Figure 5. Simulated Ka-band (26.5-40 GHz) complex reflection coefficient results for different burn degrees: a) first degree burn, b) superficial second degree burn, c) deep second degree burn, and d) third degree burn.

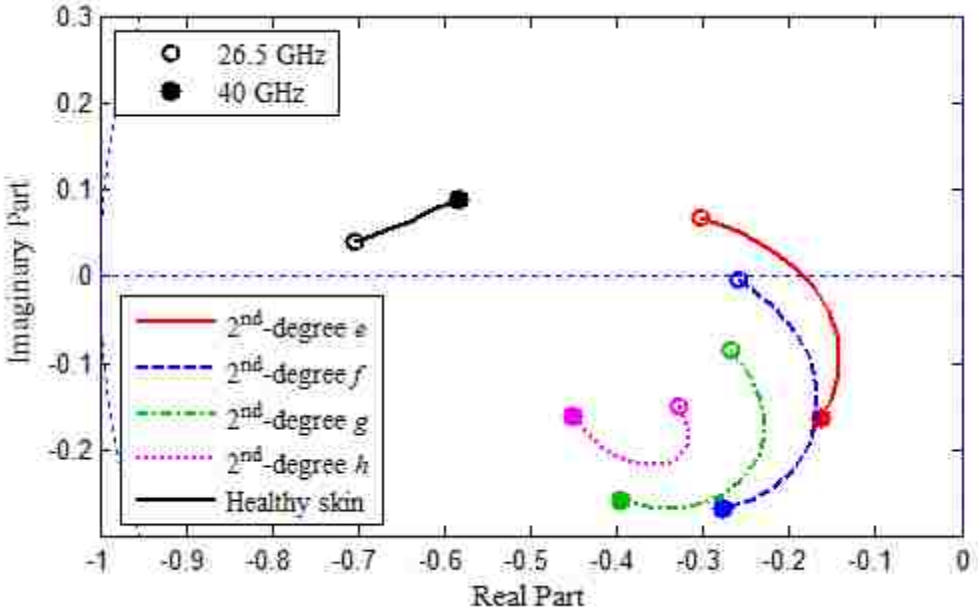

(c)

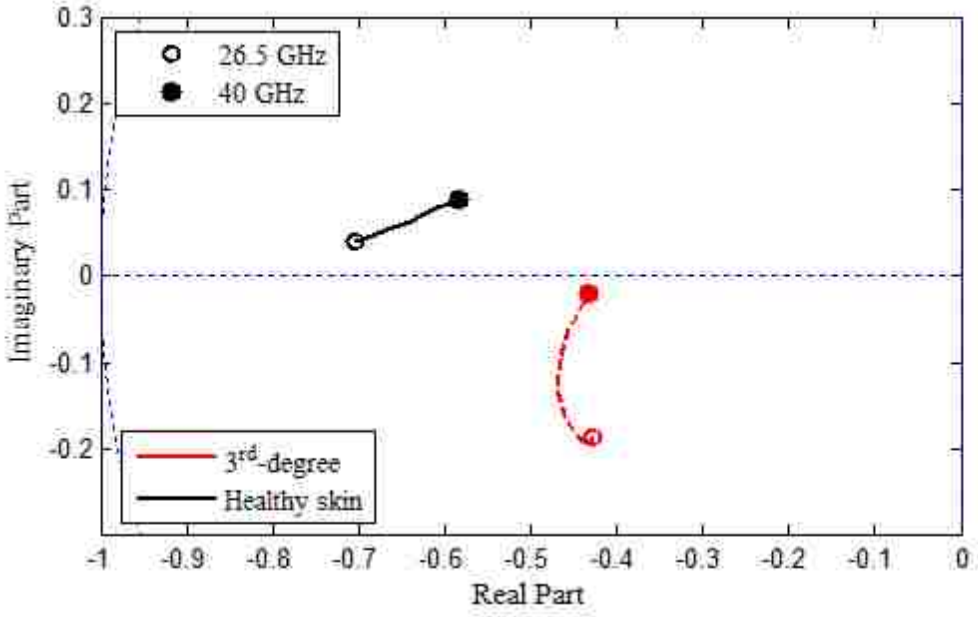

(d)

Figure 5. Simulated Ka-band (26.5-40 GHz) complex reflection coefficient results for different burn degrees: a) first degree burn, b) superficial second degree burn, c) deep second degree burn, and d) third degree burn (cont.).

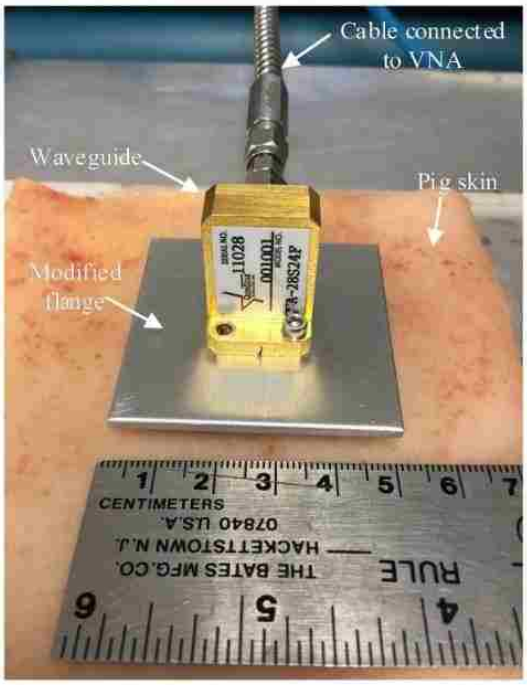

Figure 6. Pig skin sample and reflection coefficient measurement setup using a Ka-band open-ended rectangular waveguide probe.

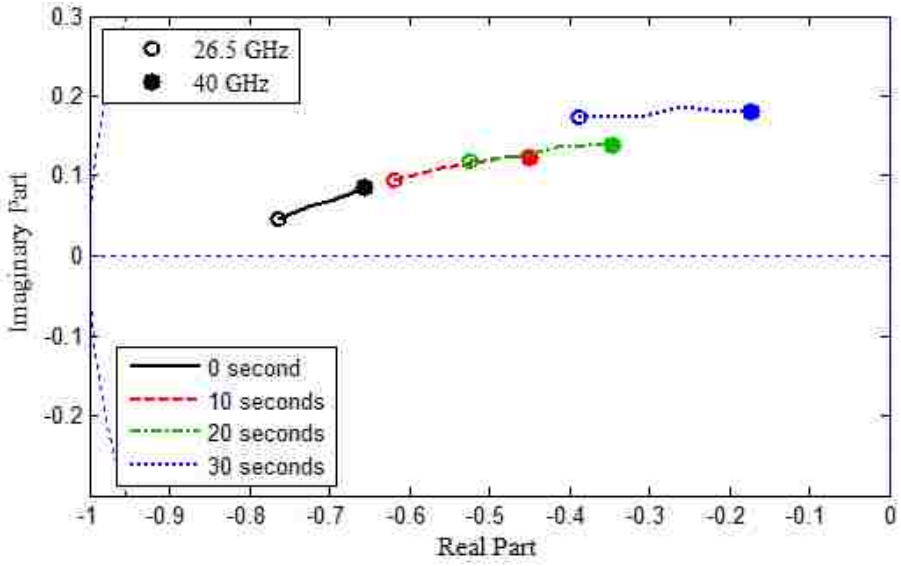

Figure 7. Measured Ka-band complex reflection coefficient of pig skin as a function of compounding burn episodes.

3.3. INFLUENCE OF MEDICAL DRESSING

Compared to the existing burn degree assessment techniques, one major advantage of millimeter wave diagnosis is that millimeter wave signals can readily penetrate medical dressings. This enables detection and evaluation of severity of burn without the need to remove the dressing which is a painful process [30]. We obtained a typical nonstick medical dressing sample and using the same method measured its dielectric constant (in the Ka-band frequency range) to be $\varepsilon_r = 1.09\text{-}j\ 0.01$ [25]. As expected, the dressing is a low loss and low permittivity material nearly similar to free-space. Then, a series of simulations, similar to those outlined in Section 3.1, was performed with the same parameters as those in Fig. 3, except a 1.5 mm-thick medical dressing was added to the layered skin structure. Compare to the simulations results without medical dressing (see Fig. 5), the results shown in Fig. 8 indicate the additional phase shift (rotation in the complex reflection coefficient) caused by the dressing thickness and some signal loss (smaller real and imaginary values) due to the expansion of the millimeter wave signal inside the dressing, as expected. But what is important is that the results with the dressing still show significant differences among different burn degrees corroborating the fact that this type of diagnosis does not require removal of medical dressings.

In addition, reflection coefficient measurements were also performed on another piece of pig skin with ~1 mm thick medical dressing in a similar fashion. The results in Fig. 9 show similar rotation with increasing burn severity and occurrence in similar positions (in the complex plane) compared to the superficial 2nd-degree burns. However, the results for the 10-second burn does not rotate towards location of 20-second burn, as

expected. This may be attributed to the measurement process. However, overall the results follow the expectations reasonably closely.

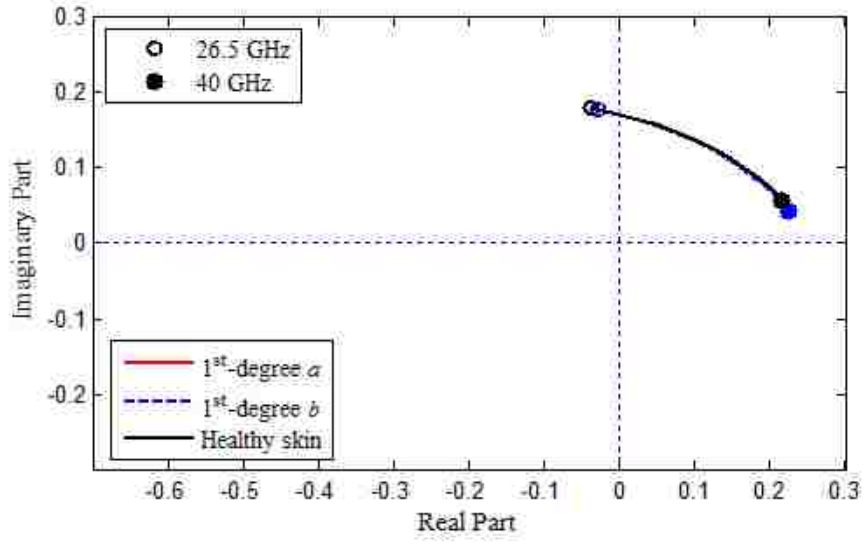

(a)

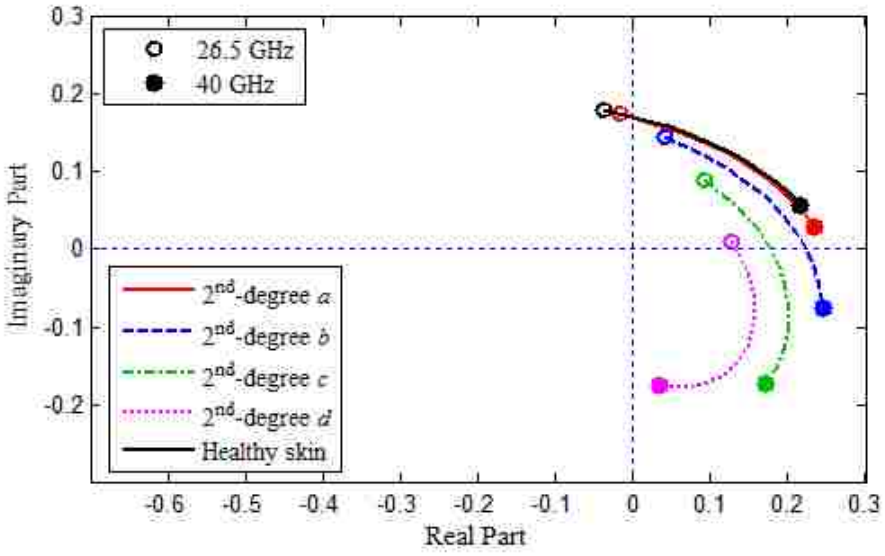

(b)

Figure 8. Simulated Ka-band (26.5-40 GHz) reflection coefficient results for different burn degrees with medical dressing: a) first degree burn, b) superficial second degree burn, c) deep second degree burn, and d) Third degree burn.

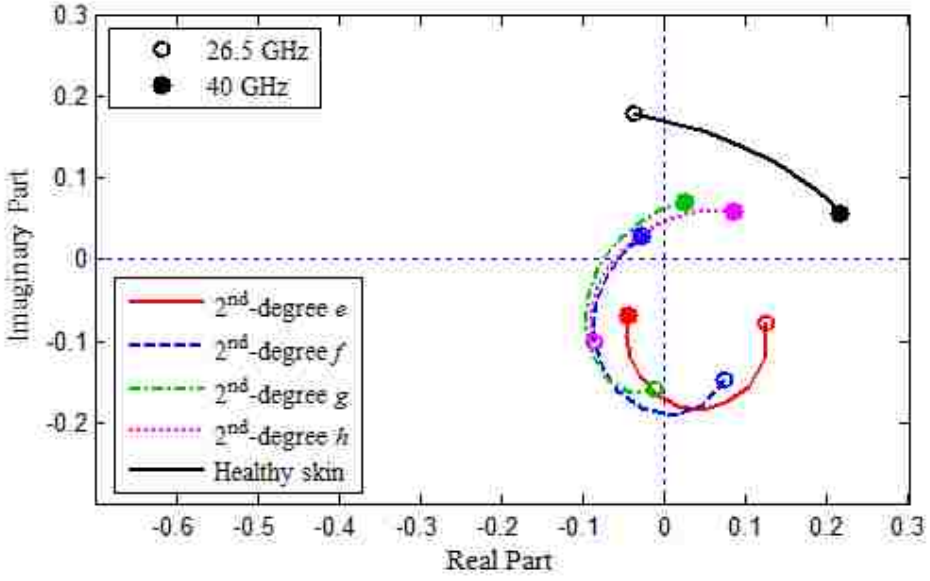

(c)

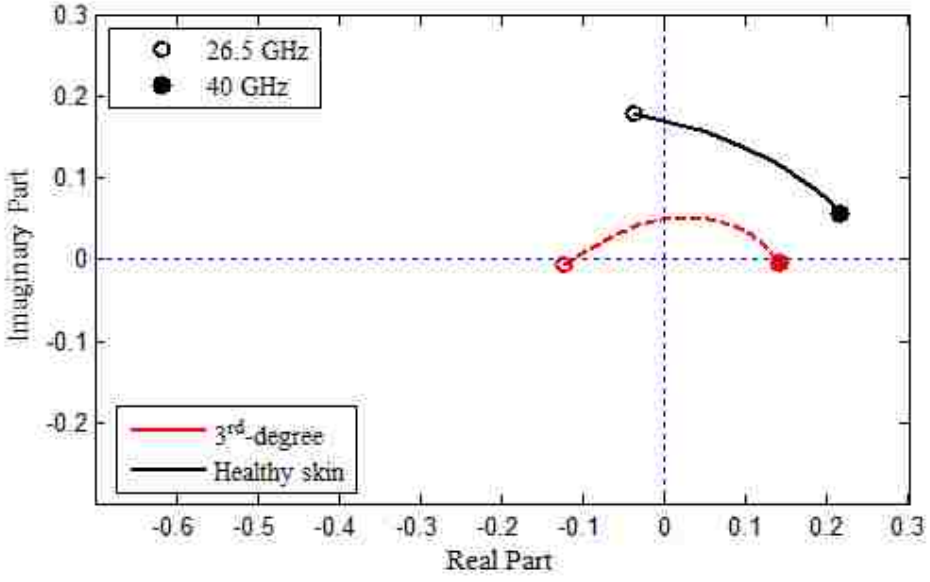

(d)

Figure 8. Simulated Ka-band (26.5-40 GHz) reflection coefficient results for different burn degrees with medical dressing: a) first degree burn, b) superficial second degree burn, c) deep second degree burn, and d) Third degree burn (cont.).

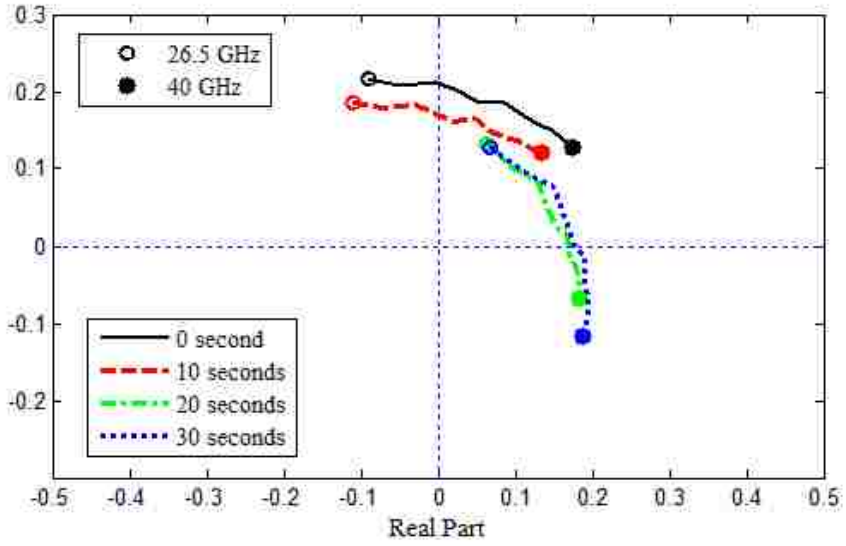

Figure 9. Measured Ka-band (26.5-40 GHz) complex reflection coefficient of pig skin covered with medical dressing as a function of compounding burn episodes.

3.4. L^2-NORM ANALYSIS

In order to quantitatively analyze the reflection coefficient results, it is useful to define a *metric* that readily and comprehensively identifies the differences among these complex reflection coefficients. Here, L^2-Norm is used as this metric, defined as:

$$L^2\text{-Norm} = \sqrt{\sum_f \left(\left| \Gamma_i(f) - \Gamma_0(f) \right|^2 \right)} \tag{2}$$

where f represent the sampled frequency point, Γ_0 is the complex reflection coefficient of unburned skin and Γ_i the same for different burn degrees. Consequently, the value associated with L^2-Norm indicates the *dissimilarity* between two complex (vector) reflection coefficients (i.e., more similar if L^2-Norm is small) over the entire measured frequency range. L^2-Norm for different burn degrees is shown in Fig. 10a. Horizontal axis ranging from 0 to 11 represents all simulated burn degrees in the order of severity, i.e., 0 for unburned skin, 1 for 1st-degree *a*, etc. The calculated L^2-Norm, using the simulation

results with and without dressing, closely follow a similar trend. The dynamic range associated with when incorporating a medical dressing is smaller than the case without the dressing, as expected and explained in Section 3.3. This also indicates a reduction in sensitivity of L^2-Norm to the degree of burns when a dressing is used. However, given the L^2-Norm for both cases follow the same trend indicates the usefulness of using this metric for either case. This can be better seen when considering the normalized L^2-Norm, as shown in Fig. 10b showing the two results very closely match. L^2-Norm (average and standard deviation) for the four measurements made on the pig skin with and without medical dressing for progressive burn episodes was calculated and the results are also shown in Fig. 10a.

Although the burn degree was not known in this case, the measured results fall in the superficial 2^{nd}-degree burn range. However, what is more important here is that the measured results follow the same trend, as a function of progressive burns, as those obtained by the simulations. In addition, L^2-Norm for the simulated results becomes insensitive to the degree of burn beyond the deep 2^{nd}-degree and then decreases for the 3^{rd}-degree burn. This results in an ambiguity when distinguishing between superficial 2^{nd}-degree and 3^{rd}-degree burns. This apparent ambiguity can be significantly minimized when L^2-Norm and actual reflection coefficient data are considered together (see Fig. 5b,d and Fig. 8b,d and the quadrants that the respective reflection coefficients appear). It is also important to note that the L^2-Norm calculated here is based on the skin model presented earlier and actual future measurements may help resolve this apparent ambiguity. Nevertheless, these promising results show the clear potential for using millimeter reflectometry as an effective diagnostics tool for burn degree evaluation.

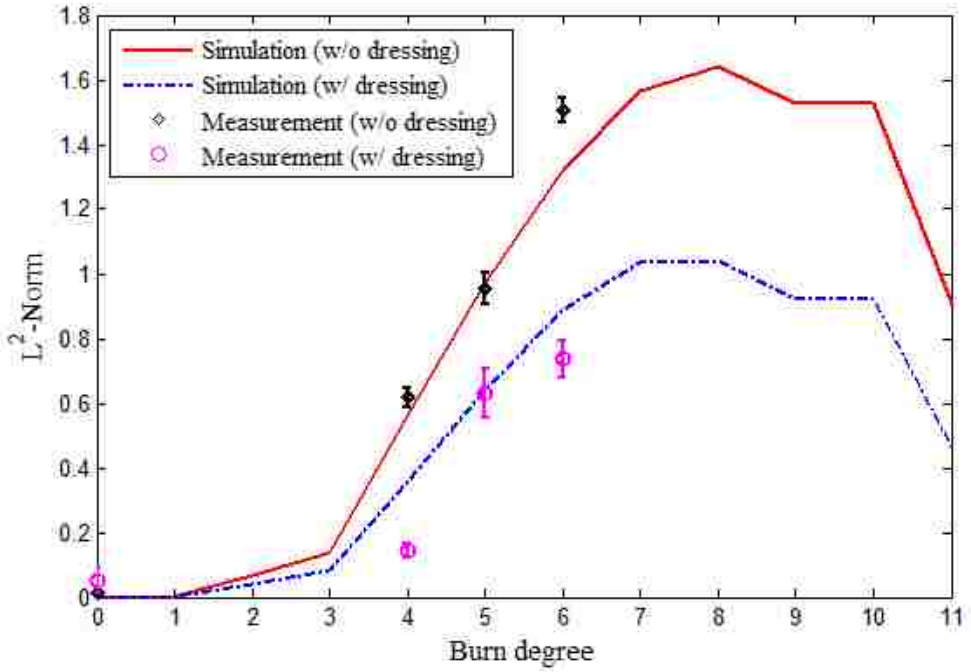

(a)

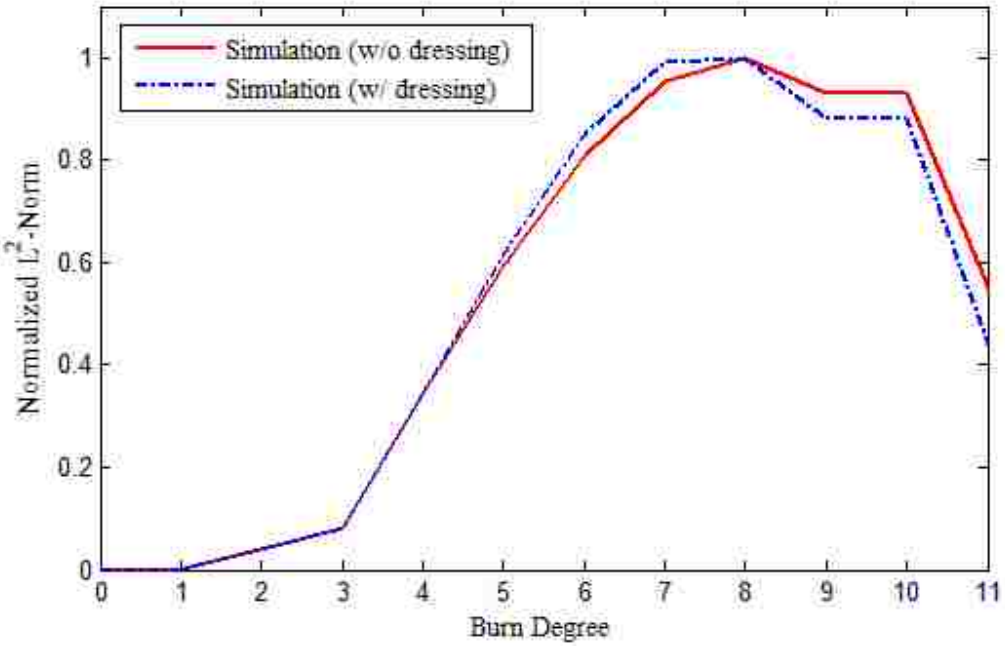

(b)

Figure 10. L^2-Norm for different burn degrees for simulations with and without dressing and for pig skin measurements.

4. BURN DIAGNOSIS BY MILLIMETER WAVE IMAGING

Recent advances in developing imaging systems and algorithms based on synthetic aperture radar (SAR) techniques, for noninvasive inspection of materials, has resulted in *real-time* systems that once optimally designed at a proper frequency range can become an effective diagnostics tool for burned skin evaluation [11], [31]-[33]. Here, several imaging results are provided to effectively illustrate the usefulness of millimeter wave imaging approach for burned skin diagnosis. Determination of actual degree of burn in these images is beyond the scope of this work as this issue will be investigated in the future and on real patients. However, the value of these imaging results cannot be underestimated. To this end, initially an imaging experiment was conducted at V-band (50-75GHz) on a burned piece of pig skin in [11], illustrating the potential of millimeter wave imaging for skin burn evaluation. To further demonstrate the efficacy of this technique, in addition to demonstrating imaging capability in the presence of medical dressings, a V-band (50-75 GHz) imaging system, attached to an automated scanning platform, was used to produce several images of a burned pig skin [34].

The center of a piece of pig skin, ~140 mm x 120 mm, was burned by a small torch (Fig. 11a left) and imaged when exposed and when covered by: a) four stacked thin layers of nonstick medical dressing (~8 mm in total) and b) one layer (~3 mm) of a different nonstick medical dressing. In a similar fashion as [11] and [34], SAR images of these three cases were produced, as shown in Fig. 11b. The burned area in the images can be clearly distinguished from its surrounding tissue when exposed and under the two different types of medical dressing with different thicknesses. The color variation within the burned spot

(indicated by the arrows) indicates subtle differences in burn severity. The influence of each type of dressing is also shown in the respective images. The red spots at the bottom of the images corresponds to local wrinkles in the skin sample.

(a)

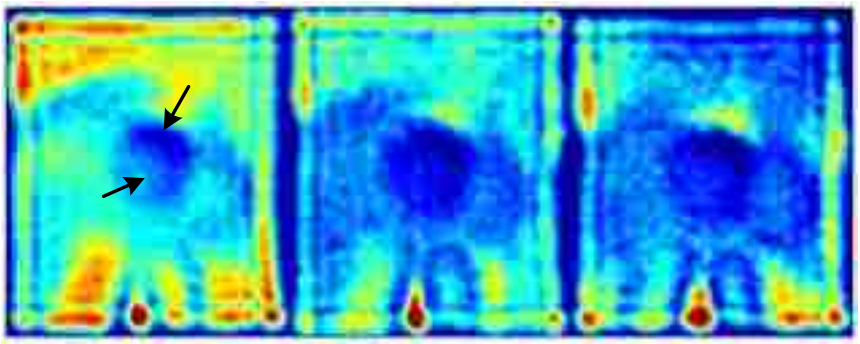

(b)

Figure 11. a) Burned pig skin from left to right: without medical dressing; with 4 layers of thin pads (~8 mm) and with 1 layer of thick pad (~3 mm), and b) corresponding SAR images.

5. DISCUSSION

Burn degree (depth of invasion) evaluation is an important issue in skin burn injury diagnosis and treatment. In this paper, the potential of localized millimeter wave reflectometry and high-resolution millimeter wave imaging were shown for this purpose.

Extensive electromagnetic simulations were preformed, at Ka-band (26.5-40 GHz), illustrating the potential for distinguishing among different burn degrees when measuring the complex reflection coefficient of skin with an open-ended rectangular waveguide probe. Similar experiments on a piece of pig skin (porcine) also showed the potential for the same. L^2-Norm calculations of the simulated reflection coefficient values, in the Ka-band frequency range, showed the possibility of using this *metric* as a simple means for distinguishing among different burn degrees both in the presence and absence of medical dressing. Limited measurements on a progressively burned piece of pig skin also closely followed similar results. Finally, the feasibility of high-resolution millimeter wave imaging was also illustrated by producing several V-band (50-75 GHz) SAR images of a burned pig skin sample with and without medical dressing.

Human skin burns are complex and dynamic as a function of time, moisture loss/gain, location in body, etc. The investigation outlined here and the subsequent results were first and foremost focused on illustrating the potential of millimeter wave diagnosis for burns in humane skin. Future investigations will have to include all other factors and experiments on actual skin (animal or human) where there is blood (and other fluids) circulation present as well.

REFERENCES

[1] World Health Organization, 2014. "Burns". [Online]. Available: http://www.who.int/mediacentre/factsheets/fs365/en/

[2] American Burn Association, 2015. "Burn Incidence Fact Sheet". [Online]. Available: http://www.ameriburn.org/resources_factsheet.php

[3] J. Latarjet. "A simple guide to burn treatment." Burns, vol. 21, no. 3, pp. 221-225, May. 1995.

[4] D. N. Herndon. "Evaluation of the burn wound: management decisions" in Total burn care. 4th ed. Elsevier. 2012.

[5] D. Heimbach, L. Engrav, B. Grube, J. Marvin. "Burn depth: a review." World J. Surg., vol. 16, no. 1, pp. 10-15, Jan. 1992.

[6] A. D. Jaskille, J. C. Ramella-Roman, J. W. Shupp, M. H. Jordan, J. C. Jeng. "Critical review of burn depth assessment techniques: part I. Historical review." J. Burn Care. Res., vol. 31, no. 1, pp. 151-157, Jan. 2010.

[7] S. Monstrey, H. Hoeksema, J. Verbelen, A. Pirayesh, P. Blondeel. "Assessment of burn depth and burn wound healing potential." Burns, vol. 34, no. 6, pp. 761-769, Sep. 2008.

[8] Y. Hayshi, N. Miura, N. Shinyashiki, S. Yagihare. "Free water content and monitoring of healing processes of skin burns studied by microwave dielectric spectroscopy in vivo." Phys. Med. Bilo., vol. 50, no. 4, pp. 599-612, Jan. 2005.

[9] A. Taeb, S. Gigoyan, S. Safavi-Naeini. "Millimetre-wave waveguide reflectometers for early detection of skin cancer." IET Microw. Antennas Propag., vol. 7, no. 14, pp. 1182-1186, Nov. 2013.

[10] P. Mehta, K. Chand, D. Narayanswamy, D. G. Beetneer, R. Zoughi, W. V. Stoecker. "Microwave reflectometry as a novel diagnostic tool for detection of skin cancers." IEEE Trans. Instrum. Meas., vol.55, no.4, pp. 1309-1316, Aug. 2006.

[11] Y. Gao, R. Zoughi. "Millimeter reflectometry as an effective diagnosis tool for skin burn injuries." Proc. of the IEEE Int. Instrumentation and Measurement Technol. Conf. (I2MTC), pp. 460-464, Taipei, Taiwan, May 23-26, 2016.

[12] Z. D. Taylor, et al. "Reflective terahertz imaging of porcine skin burns." Opt. Lett., vol. 33, no. 11, pp. 1258-1260, June. 2008.

[13] National Cancer Institute. "Epidermis, dermis and subcutaneous layers of skin". [Online]. Available: https://visualsonline.cancer.gov

[14] S. I. Alekseev and M. C. Ziskin. "Human skin permittivity determined by millimeter wave reflection measurements." Bioelectromagnetics. vol. 28, no. 5, pp. 331-339, July. 2007.

[15] F. Topfer, and J. Oberhammer. "Millimeter-wave tissue diagnosis: the most promising fields for medical applications." Microw. Mag. vol.16, no. 4, pp. 97-113, May. 2015.

[16] A. Sihvola. "Mixing rules with complex dielectric coefficients." Subsurf. Sens. Technol. Appl. vol. 1, no. 4, pp. 393-415, Oct. 2000.

[17] R. Aminzadeh, M. Saviz, and A. A. Shishegar. "Dielectric properties estimation of normal and malignant skin tissues at millimeter-wave frequencies using effective medium theory." in 2014 22nd Iranian Conf. Elect. Eng.,, pp. 1657-1661.

[18] D. B. Bennett, W. Li, Z. D. Taylor, W. S. Grundfest, E. R. Brown. "Stratified media model for terahertz reflectometry of the skin." IEEE Sensor Journal. vol. 11, no. 5, pp. 1253-1262, May, 2011.

[19] Z. D. Taylor, et al. "THz medical imaging: in vivo hydration sensing." IEEE Trans. THz Sci. Technol., vol. 1, no. 1, pp. 201-219, Sept. 2011.

[20] M. Saviz, et al. "Theoretical estimations of safety thresholds for terahertz exposure of surface tissues." IEEE Trans. THz Sci. Technol, vol. 3, no. 5, pp. 635-640, 2013.

[21] F. T. Ulaby, R. K. Moore, A. K. Fung. "Microwave dielectric properties of natural earth materials" in Microwave remote sensing active and passive volume III: from theory to application. MA, USA, Artech House. 1986.

[22] D. M. Jackson. "The diagnosis of the depth of burning." Br. J. Surg., vol. 40, no. 164, pp. 588-596, May. 1953.

[23] D. P. Orgill. "Excision and skin grafting of thermal burns." N. Engl. J. Med.., vol. 360, no. 9, pp. 893-901, Feb. 2009.

[24] S. Kharkovsky, M. T. Ghasr, M.A. Abou-Khousa and R. Zoughi, "Near-field microwave and mm-wave noninvasive diagnosis of human skin," Proceedings of the IEEE Int. Workshop on Medical Measurement and Appl. (MeMeA 2009), pp. 5-7, Cetraro, Italy, May 29-30, 2009.

[25] M. T. Ghasr, D. Simms and R. Zoughi, "Multimodal solution for a waveguide radiating into multilayered structures-dielectric property and thickness evaluation." IEEE Trans. Instrum. Meas., vol. 58, no. 5, pp. 1505-1513, May. 2009.

[26] S. Gabriel, R. W. Lau, and C. Gabriel. "The dielectric properties of biological tissues: III. Parametric models for the dielectric spectrum of tissues." Phys. Med. Biol., vol. 41, no. 11, pp. 2271-2293, 1996.

[27] L. Cuttle, et al. "A porcine deep dermal partial thickness burn model with hypertrophic scarring." Burns, vol. 32, no. 7, pp. 806-820, Nov. 2006.

[28] American burn association, 2016. "2016 national burn repository-report of data from 2006-2015". [Online]. Available: http://www.ameriburn.org/2016%20ABA%20Full.pdf

[29] M. Kempin, M. T. Ghasr, J. T. Case and R. Zoughi, "Modified waveguide flange for evaluation of stratified composites." IEEE Trans. Instrum. Meas., vol. 63, no. 6, pp. 1524-1534, June. 2014.

[30] S. W. Harmer, S. Shylo, M. Shah, N. J. Bowring, and A. Y. Owda. "On the feasibility of assessing burn wound healing without removal of dressings using radiometric millimeter-wave sensing." PIER M. vol. 45, pp. 173-183, 2016.

[31] D. M. Sheen, D. L. McMakin, T. E. Hall. "Three-dimensional millimeter-wave imaging for concealed weapon detection." IEEE Trans. Microw. Theory and Techn., vol. 49, no. 9, pp. 1581-1592, Sept. 2001.

[32] J. T. Case, M.T. Ghasr, and R. Zoughi, "Optimum two-dimensional uniform spatial sampling for microwave SAR-based NDE imaging systems." IEEE Trans. Instrum. Meas., vol. 60, no. 12, pp. 3806-3815, Dec. 2011.

[33] M. Fallahpour, J. T. Case, M. T. Ghasr, and R. Zoughi, "Piecewise and wiener filter-based SAR techniques for monostatic microwave imaging of layered structures." IEEE Trans. Antenna Propag., vol. 62, no. 1, pp. 282-294, Jan. 2014.

[34] M. T. Ghasr, J. T. Case, and R. Zoughi, "Novel Reflectometer for Millimeter Wave 3D Holographic Imaging." IEEE Trans on Instrum. Meas., vol. 63, no. 5, pp. 1310-1319, 1328-1336, May 2014.

II. TOWARDS ACCURATE AND WIDEBAND IN VIVO MEASUREMENT OF SKIN DIELECTRIC PROPERTIES

ABSTRACT

In this paper, we first review the most common measurement methods, previously used, for assessing the complex permittivity of human skin, namely open-ended coaxial and waveguide probe reflectometry methods. We then outline and emphasize their useful features and shortcomings that can adversely affect the measurements. Then, an approach utilizing an open-ended waveguide probe, with an engineered ground plane and a thin dielectric layer in front of the aperture to prevent skin protrusion is proposed. This approach utilizes a full-wave electromagnetic model that accurately describes the interaction of a layered skin with this probe. Furthermore, comprehensive analyses were performed to investigate important sources of modeling and measurement errors and their influences on the calculated skin complex permittivity. The results of these analyses showed that proposed method can achieve ~85% and ~95% calculation accuracy for skin relative (to free-space) dielectric constant and relative dielectric loss factor, respectively. Finally, a series of *in vivo* measurement were performed in Ka-band (26.5-40 GHz) on several different locations of three human subjects, using this proposed method. In addition, it is demonstrated that homogenous skin model cannot be used for areas of body where the *stratum corneum* (SC) layer is relatively thick (e.g., palm). Finally, the effect of thick SC layer on relative complex permittivity calculation was discussed and a modified method to determine the relative complex permittivity of layered skin was proposed and verified by simulations.

Index Terms—Skin, reflectometry, relative complex permittivity, *in vivo*, dielectric properties.

1. INTRODUCTION

Skin is the largest organ in human body, which in addition to protecting it from the environment, it also regulates body temperature and moisture balance [1]. Skin is also susceptible to injuries (e.g., burns) and diseases (e.g., cancers). Recent investigations into using non-invasive high-frequency (i.e., microwave and millimeter wave) methods have shown tremendous potential for diagnosing such injuries and diseases [2-5]. For such purposes, proper knowledge of the electromagnetic properties of skin, primarily its complex permittivity, is critically important, since changes in this parameter are closely related to changes in its biophysical properties, especially its water content. Consequently, changes in skin complex permittivity can yield information about skin cancer diagnosis and skin burn assessment [2-5]. Relative (to free-space) complex permittivity is denoted by $\varepsilon_r = \varepsilon_r' - j\varepsilon_r''$, where ε_r' is the relative dielectric constant and ε_r'' is the relative dielectric loss factor. For brevity, hereon the word "relative" is assumed and omitted in the text.

In addition, Federal Communications Commission (FCC) has approved the following new licensed frequency bands: 28 GHz (27.5-28.35 GHz), 37 GHz (37-38.6 GHz), 39 GHz (38.6-40GHz) and an unlicensed band at 64-71 GHz for the fifth generation (5G) communication needs [6]. Due to the high moisture content of skin, electromagnetic waves at these frequencies primarily interact with the skin layer and do not penetrate much

beyond. Therefore, accurate information about skin complex permittivity is crucially important for evaluating dosimetry and for setting exposure limit standards. Therefore, a robust and accurate measurement method (including the corresponding complex permittivity calculation algorithm) suitable for *in vivo* human skin complex permittivity assessment is highly desired.

For the purpose of modeling the interaction of the skin with electromagnetic wave, several skin models may be considered, as shown in Figs. 1(a)-(e) [7]-[9]. Human skin consists of three layers from the outermost to the innermost layer, namely: *epidermis*, *dermis* and *subcutaneous fat* tissue. However, the top layer of epidermis which is called *stratum corneum* (*SC*), as shown in Fig. 1 (a), represents the driest layer [7]. The rest of epidermis is referred to as the *viable epidermis* which has similar water content to dermis. The complex permittivity of skin is mainly affected by its water content. Thus, each skin layer with different water content has a different complex permittivity. Normally, epidermis is ~0.06-0.1 mm thick, dermis is ~1.2-2.8 mm thick and the SC layer is ~20 μm thick [7]-[8]. However, depending on the body location, SC may be somewhat thicker [10]-[11]. Fig. 1(a) represents the most general layered structure of the skin, representing the situation where every layer has a different complex permittivity. Fig. 1(b) is the homogenous skin model, which is the most simplified and widely used model. Fig. 1(c) shows the addition of the top dry SC layer to the homogeneous model. Fig. 1(d) is a two-layer model consisting of homogeneous skin and fat. Fig. 1(e) shows the addition of the top dry SC layer to the model in Fig. 1(d). In addition, *viable epidermis* and *dermis* are assumed to have the same complex permittivity in Fig. 1(b)-(e) and the bottom layers in all model are infinitely thick. Finally, any electromagnetic model used must *correctly* and

accurately represent the probe electromagnetic field characteristics and its subsequent interaction with a correct and representative model of the skin. To this end, in this paper we first provide a thorough review of the previous works related to skin complex permittivity measurement, along with a discussion of each method's limitations and considered approximation which are seldom quantitatively discussed.

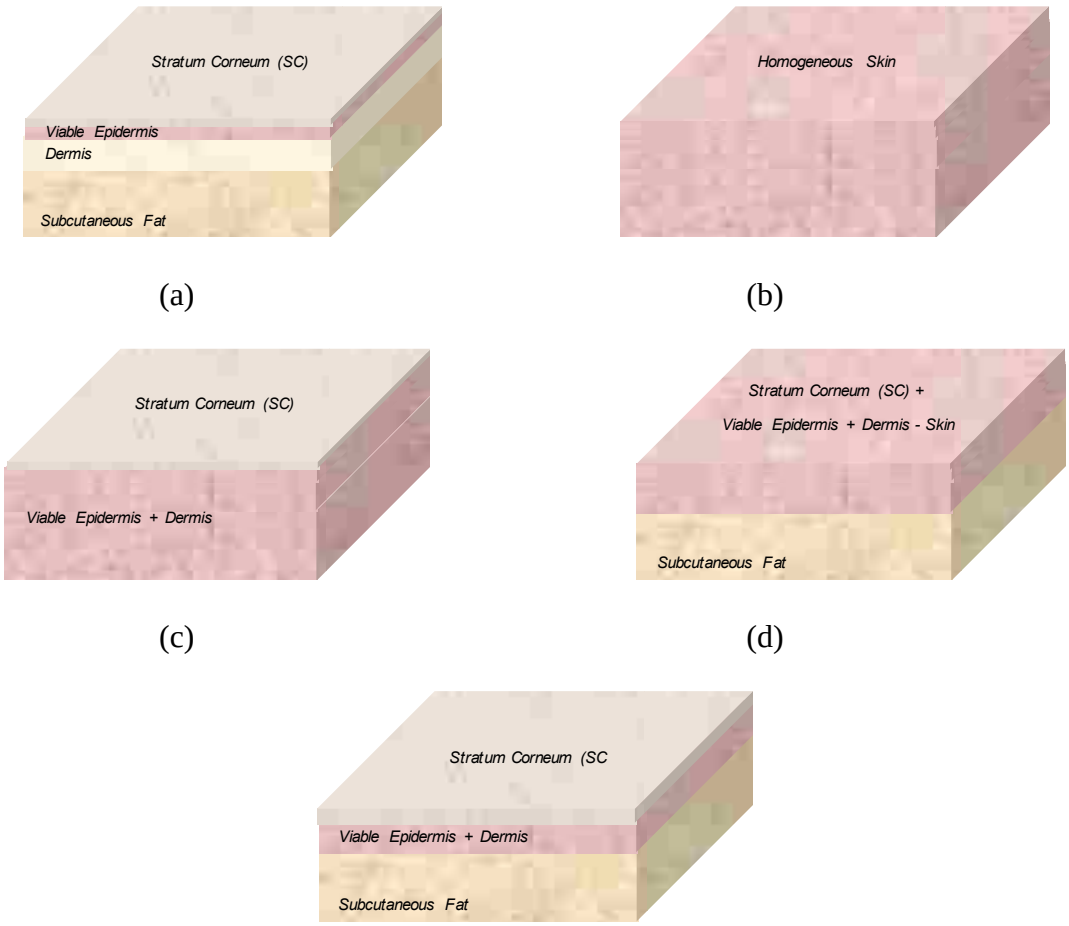

Figure 1. Human skin model (not-to-scale) for different assumption (a) four layers model, (b) homogenous model, (c) two layers model assuming SC layer is not negligible but fat layer can be ignored, (d) two layers model for situation that SC layer can be ignored but fat layer cannot, (e) three layers model for both SC and fat layer are taken into account (all not-to-scale). Viable epidermis is assumed has same relative complex permittivity compared to dermis in model (b-e).

Subsequently, we fully describe and analyze the implementation an open-ended rectangular waveguide probe to evaluate the complex permittivity of human skin, *in vivo*. However, contrary to previously-implemented methods using the same probe, the approach outlined here uses a *full-wave* electromagnetic model which fully describes the interaction of a wideband signal radiated by this probe into a layered model of human skin [12]. This method provides for correct calculation of the complex permittivity (and thickness if need be) of a given layer within the skin structure. In addition, and as will be seen later, this model properly (i.e., no approximation) facilitates the use of a known additional layer of a material, placed in front of the open-ended waveguide aperture to prevent skin from protruding into the waveguide, which is an extremely critical issue. As a result, we first thoroughly discuss the relevant practical issues associated with using an open-ended waveguide probe for measuring skin complex permittivity *in vivo*. This includes concerns and remedies over the effects of: *i*) approximating probe electromagnetic field modes and the influence of waveguide ground plane (flange) edge reflections resulting in errors in the measured reflection coefficient, which is then used to calculate the complex permittivity from these measurements, and *ii*) pressure (on the skin) that is used in the measurements. Then, the possible sources of complex permittivity calculation errors are discussed, including using *i*) homogenous assumption for skin, *ii*) errors in the thickness and complex permittivity of the additional layer placed between the waveguide probe and the skin to prevent skin protrusion into the waveguide, and *iii*) instrument noise and (operator) measurement inconsistency. Subsequently, *in vivo* human skin measurements are conducted on three human subjects and on several different locations within their bodies. Finally, the effect of thick SC layer in complex permittivity calculation is discussed, then

a modified method suitable for general layered structure is proposed and verified by simulation.

2. BACKGROUND OF HUMAN SKIN COMPLEX PERMITTIVITY MEASUREMENT

Currently, the most commonly used skin complex permittivity measurement method involves measuring the reflection coefficient of skin, in contact with an open-ended coaxial or a rectangular waveguide probe. Subsequently, the measured reflection coefficient is used in conjunction with an electromagnetic model that describes the measurement environment, to extract the complex permittivity. A comprehensive review of complex permittivity measurement of biological tissues, including human skin, was conducted in 1996 [13] and the review below mainly focuses on the subsequent progress in this field.

Application of open-ended coaxial probe is relatively easy and measuring dielectric properties of certain materials (i.e., infinite half-spaces and liquids) has been well documented [14]-[15]. A series of investigations were conducted in the 1990s, with respect to determining human skin complex permittivity, using open-ended coaxial probes [16]-[18]. *In vivo* measurements of reflection coefficient were first performed with this probe on human palm, forearm and sole of foot in the frequency range of 10 Hz to 20 GHz. Subsequently, skin complex permittivity at these locations was calculated based on the admittance model of the coaxial probe [19]. Finally, a parameterized Cole-Cole model was developed, by *curve-fitting* the complex permittivity results below 20 GHz. Then, the complex permittivity values at higher frequencies were obtained by *extrapolating* the

lower-frequency results [18]. A similar method was used to measure and calculate the complex permittivity of palm and wrist epidermis in 0.5-110 GHz by a small coaxial probe [20]. However, in this work it is assumed that only epidermis layer is sampled by the electric field of the probe. Additionally, the approach used to determine the sampled thickness is performed on pork fat and muscle, so the obtained quantitative results do not apply to human skin. It is also not clear whether the results are obtained *in vivo* or performed on excised skin. N. Chahat *et al.* used a commercial measurement system to conduct *in vivo* complex permittivity measurements on human palm, wrist and forearm in the 10-60 GHz frequency range [21]. The major disadvantage of the admittance model-based open-ended coaxial probe method is that it assumes human skin to be homogenous (only a single layer), which is not necessarily a correct assumption (particularly as a function of body location) and can lead to errors in calculating the complex permittivity. For example, reflection coefficient measured on forearm/wrist and palm with an open-ended coaxial probe could be substantially different since palm usually has a thicker and drier stratum corneum (SC) layer [17], [20]-[21]. In addition, penetration depth of coaxial probe is proportional to its diameter. Thus, to eliminate the influence of the existing fat layer below the skin, a small-diameter coaxial probe is usually used to assure the field sampling depth is in the skin layer only. However, using such coaxial probe and when the SC layer is relatively thick, viable epidermis and dermis layers may not be sufficiently exposed to the probe fields. All these reasons result in a lower-than-expected calculated complex permittivity of skin [17] [21].

The issue of skin inhomogeneity is mentioned by several researchers and attempts have been made to consider the layered nature of skin. However, using a static admittance

model limits the application to only several hundred megahertz [22]-[25]. Sasaki *et al.* employed several different methods, including open-ended coaxial probe reflectometry, to determine complex permittivity of different skin layers [26]-[27]. However, the measurements were performed on dissected porcine skin. This method is not suitable for establishing *in vivo* human skin complex permittivity due to the destructive nature of the measurements. To properly model the interaction between open-ended coaxial probe and layered skin structure, a wave propagation model is needed, such as the one developed in [28]. Furthermore, appropriate calculation algorithm is needed to properly extract the complex permittivity or/and thickness of each layer. Unfortunately, to-date no such effort has been reported. Finally, calibrating an open-ended coaxial probe, for measuring the reflection coefficient of non-liquid materials, is not a straightforward process and any errors due to calibration can significantly and adversely affect the measurement results [29]. This limits the potential of using a coaxial probe for complex permittivity determination in a general layered structure.

Open-ended waveguide probes have also been used as an effective tool to obtain thickness and complex permittivity of layered dielectric materials [12] [30]-[31]. Alekseev *et al*. utilized open-ended waveguide probes to measure the *power* reflection coefficient (not the complex reflection coefficient) of human skin and subsequently obtained skin complex permittivity and thickness by *curve fitting* the measured data [8]. In that work, different multilayer skin models were proposed, and the results showed that the multilayer model gives better fitting results compared to the homogenous model (i.e., assuming skin to be a single homogeneous layer). Although the results showed good agreement with other cited references in the literature, transverse electromagnetic (TEM) wave assumption was

used in the calculation, which is not the case in reality. That is to say that this assumption: *i*) does not properly account for the complex interaction of EM field in the near-field of a waveguide probe with a skin layer(s), and *ii*) it ignores the ever-important higher-order modes that are generated at the aperture, all of which lead to inaccuracies when calculating the complex permittivity of skin [12]. The consequences of these critical issues, on the calculated skin thickness and complex permittivity, are also not discussed in detail. Hey-Shipton *et al*. measured human palm *in vivo* at 8-18 GHz with a waveguide probe and polystyrene plug to prevent skin protrusion into the open-ended waveguide probe [32]. However, when calculating skin complex permittivity, they ignored the presence of the plug (i.e., assuming plug has a complex permittivity equal to that of free-space), which is not the case. In addition, they also used the infinitely thick skin layer (i.e., homogeneous) model for human palm. Ghodgaonkar *et al.* measured human palm *in vivo* with a waveguide probe and a Teflon impedance transformer [33]-[34]. However, again a homogenous model is used for the palm skin. In addition, a transmission line assumption was used to account for the presence of the Teflon impedance transformer, which is not accurate when dealing with radiation through an open-ended waveguide probe. This constitutes only an approximation, which can significantly impact the calculation of complex permittivity. Moreover, the measurements were conducted with a waveguide probe with a finite flange, but infinite flange formulation was used for calculation, this may also lead to additional errors in complex permittivity calculation, as described in [35].

Another important practical issue to consider, when using an open-ended waveguide probe, is that when measuring soft materials, such as skin, the applied pressure can result in significant errors as a consequence of tissue protrusion into the waveguide

aperture. Several solutions have been proposed to overcome this critical concern, such as using some variations of a plug [32]-[34], [36]. However, in all cases the issues discussed above remain unresolved. A filled waveguide solution was also proposed to solve the pressure problem, but only for measuring the reflection coefficient of healthy skin to be compared with an unhealthy skin (i.e., not for calculating skin complex permittivity) [37]-[38].

Several other methods have also been used for determining skin complex permittivity. Time-domain spectrometry has been used to measure excised healthy and wounded skin complex permittivity in the frequency range of 10 MHz-10 GHz [39]. Free-space transmission method is used in the frequency range of 60-100 GHz for excised human skin [40]. However, these two studies are invasive and not applicable to *in vivo* measurements. Secondary effect of electromagnetic wave interaction with skin, such as thermal effect, is also utilized to determine the power density and penetration depth in skin, then penetration depth is used for complex permittivity calculation [41]. But this method is only verified for a single frequency.

The measurement approaches mentioned above have their respective limitations and considered approximations that affect the outcome of calculating the complex permittivity of skin to varying degrees. Unfortunately, the influence of these limitations and approximations on complex permittivity calculation results is seldom discussed. Consequently, a more robust and accurate measurement methodology with a comprehensive discussion of calculation accuracy analysis is desired, particularly for *in vivo* skin measurement.

3. PRACTICAL PROBLEMS AND THEIR REMEDIES USING AN OPEN-ENDED WAVEGUIDE PROBE FOR SKIN MEASUREMENTS

3.1. INFLUENCE OF FIELD DISTRIBUTION ASSUMPTION AND FINITE GROUND PLANE EDGE REFLECTIONS ON SKIN COMPLEX PERMITTIVITY MEASUREMENTS

As mentioned in Section 1, when using open-ended rectangular waveguide probes for skin complex permittivity measurements, the previously implemented irradiating wave model has been either free-space TEM mode or transmission line model for impedance matching in a portion of the overall measurement probe. In addition, when waveguide admittance model used (non-TEM) the influence of higher-order modes, present at the waveguide aperture, has been ignored. Neglecting these important facts can result in significant errors in calculating complex permittivity.

As part of a broader and more general investigation of radiation of electromagnetic waves into layered composite structures, a comprehensive forward model and inverse (forward-iterative) algorithm for waveguide probe interaction with multilayer structures was developed in [12]. This model is capable of accurately producing the complex reflection coefficient, referenced at the waveguide aperture, for an open-ended rectangular waveguide probe radiating into a generally lossy layered structure. Specifically, the model accounts for the presence of higher-order modes in addition to the dominant TE_{10} mode for proper electromagnetic field matching at the waveguide aperture. Higher-order modes are generated at the waveguide aperture and contribute to the complex reflection coefficient from which the thickness and complex permittivity of each layer are subsequently calculated.

To show the differences in calculating the complex reflection coefficient, at the waveguide aperture, using only TEM waves, only waveguide TE_{10}, and addition of 14 higher-order modes to the dominant TE_{10} mode, Fig. 2a shows the simulated complex reflection coefficient of skin at Ka-band (26.5-40 GHz). These are also compared to the results obtained by a full-wave electromagnetic model using CST Microwave Studio®. For the purpose of this comparison, the skin was assumed to be thick and homogeneous with its complex permittivity given in [18] (for non-wet skin). The results clearly indicate that TEM wave assumption results in significant error in simulated reflection coefficient compared to when proper waveguide aperture irradiating wave model is used. The CST Microwave Studio® simulated reflection coefficient was used to calculate the complex permittivity of the skin by using the TEM model, open-ended waveguide model with 1 and 15 modes, respectively. The calculated results are show in Fig. 2 (b) and 2(c). As the results show, the error in calculating both the dielectric constant and dielectric loss factor can be very substantial. The results also indicate that this difference in complex permittivity calculation is a function of frequency and decreases as frequency increases. In addition, the results in Fig. 2 show that ignoring the presence of higher-order modes affect the results less significantly than the TEM wave assumption, because of the high loss nature of complex permittivity used for this comparison [12].

In this study, calculation error is defined by:

$$\text{Calculation Error} = \left|\frac{\varepsilon_{Theoretical} - \varepsilon_{Calculated}}{\varepsilon_{Theoretical}}\right| \times 100\% \quad (1)$$

where, $\varepsilon_{Theoretical}$ is the theoretical dielectric constant or dielectric loss factor used in simulation, and $\varepsilon_{Calculated}$ is the calculated dielectric constant or dielectric loss factor.

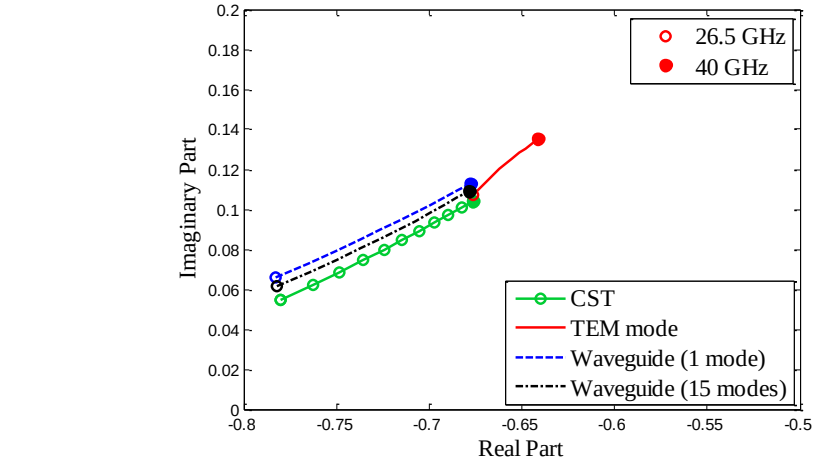

(a)

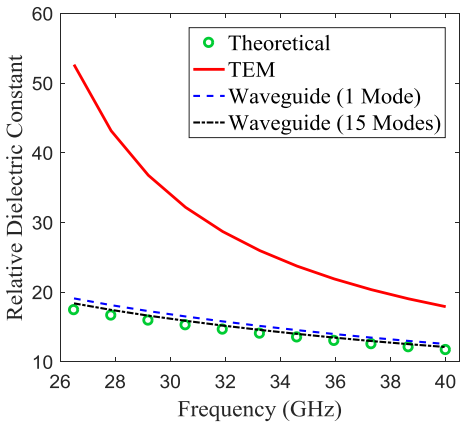

(b)

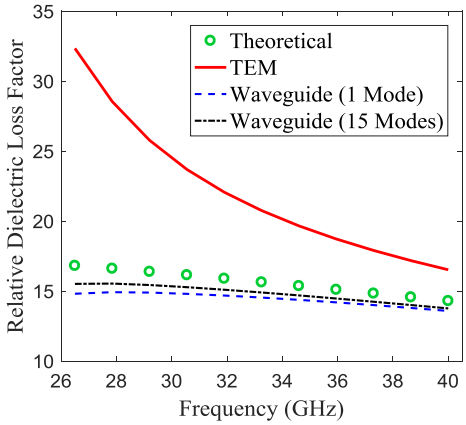

(c)

Figure 2. (a) Simulated reflection coefficient of homogenous skin for different irradiating wave modes including CST results, (b) calculated relative dielectric constant, and (c) calculated relative dielectric loss factor with different models.

Another consideration, when using open-ended rectangular waveguide probes, has to do with the fact that all (forward) models assume an infinite ground plane at the waveguide aperture, while the measurements are instead conducted with finite-sized ground planes (i.e., waveguide flanges). Reflections caused by the edges of a finite-sized

flange also contribute to errors in the measured reflection coefficient compared with those derived from the models. This in turn leads to additional sources of error when calculating complex permittivity. One effective solution to this problem is the use of a modified (engineered) flange that closely represents the electromagnetic characteristics of an infinite ground plane used in the modeling and simulations [35]. Figure 3 shows a picture of an open-ended waveguide probe with a standard (finite-sized) flange (left), and a modified (engineered) flange (right), respectively.

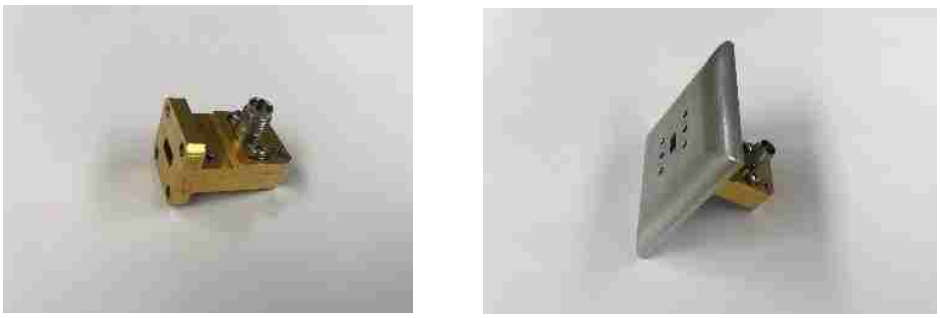

(a) (b)

Figure 3. Open-ended waveguide probe with a standard (finite) flange (left), and a modified (engineered) flange (right).

Therefore, throughout this paper and in all reported simulation results: a) higher-order modes (15 modes) are considered and b) all measurements are conducted with the engineered flange, to significantly reduce any errors associated with their respective issues, as discussed above. Furthermore, the algorithm for calculating the reflection coefficient (forward model) and calculating complex permittivity used in this paper is as same as the one given in [12], otherwise more description will be given.

3.2. INFLUENCE OF APPLIED PRESSURE ON SKIN COMPLEX PERMITTIVITY MEASUREMENTS

Skin is a soft tissue. Consequently, it is necessary to apply some pressure to assure that the open-ended waveguide aperture is completely covered by the skin tissue. However, this pressure cause skin to protrude into the waveguide to some degree, as depicted in Fig. 4(a). This will significantly affect the measured complex reflection coefficient, which in turn leads to significant errors in the calculated complex permittivity of the skin. To illustrate the importance of the need to account for and remedy this practical issue, a corresponding simulation model was constructed using CST Microwave Studio®, at Ka-band (26.5-40 GHz), as shown in Fig. 4(b). For this illustration, skin is assumed to be homogenous and its complex permittivity is again set equal to that given in [18]. In this model, variations in the complex reflection coefficient, caused by skin protrusion, were calculated as a function of the effective thickness of protruding skin tissue (i.e., *t*) inside the open-ended waveguide probe, as shown in Fig. 4(b).

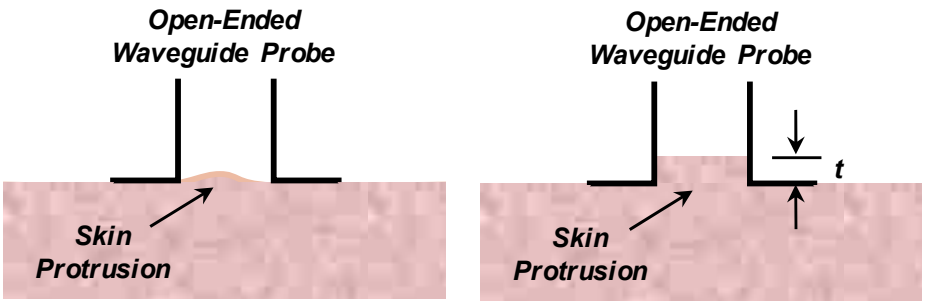

(a) (b)

Figure 4. (a) Illustration of skin protrusion problem, and (b) Simulation model in which pressure on skin is represented by its protrusion inside the waveguide probe and its effective thickness, *t*.

The simulated results in Fig. 5 show that even a very slight amount of pressure, represented by a skin protrusion of t = 0.2 mm, can cause significant change in the complex reflection coefficient of the skin, especially in its phase, as expected. However, what is more important is the effect of this pressure on the calculated complex permittivity of skin. To show this adverse influence, the results shown in Fig. 5 for t = 0 mm and 0.2 mm were used to calculate the complex permittivity of skin using the algorithm given in [12]. The calculated results are compared with the theoretical value (complex permittivity used in full-wave simulation) in Fig. 6. Results show that when no skin tissue protrudes into waveguide (t = 0 mm), the calculated complex permittivity is very close to the theoretical value, as expected. The slight differences are due to the numerical calculation error associated with the full-wave simulation. On the other hand, when even a slight amount of skin tissue protrudes into the waveguide (t = 0.2 mm), the calculated complex permittivity is very different than the theoretical values, even resulting in an erroneous negative dielectric loss factor values over the frequency range. The results clearly show that the reflection coefficient error caused by pressure can lead to significant complex permittivity calculation error.

A rigid additional dielectric material layer can be added, in front of the open-ended waveguide aperture, to prevent skin protrusion into the waveguide. Then, using the algorithm given in [12], which properly accounts for the presence of this layer, one can accurately calculate the skin complex permittivity if the thickness and the complex permittivity of this additional layer are known. This fact will be shown later along with a discussion of the sensitivity of skin complex permittivity calculation as a function of the thickness and complex permittivity of this layer.

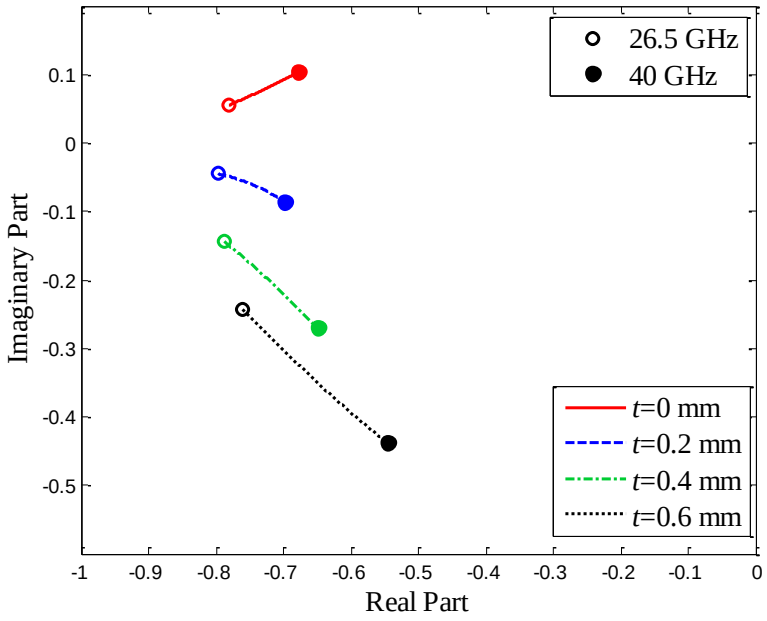

Figure 5. Simulated reflection coefficient results for different amounts of pressure represented by *t* in Fig. 4(b).

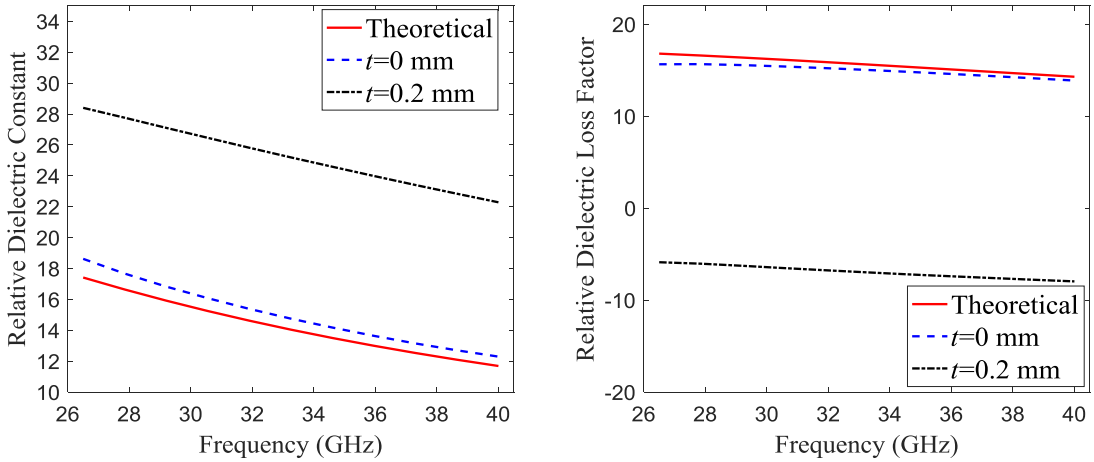

(a) (b)

Figure 6. Calculated relative complex permittivity based on full-wave simulated reflection coefficient: (a) relative dielectric constant, and (b) relative dielectric loss factor.

4. CONSIDERATION OF POTENTIAL SOURCES OF COMPLEX PERMITTIVITY CALCULATION ERROR IN THE PROPOSED METHOD

4.1. ERROR CAUSED BY USING HOMOGENEOUS SKIN ASSUMPTION

Skin is commonly assumed to be homogenous at microwave and millimeter wave frequency bands because of the limited penetration depth into the skin at these frequencies. However, the quantitative analysis of complex permittivity calculation error caused by this assumption is seldom reported and remains unknown.

Using the homogenous skin model means that the influences of dry SC layer and the subcutaneous fat layer are ignored. The conditions under which this assumption is valid are: (a) the SC layer is very thin, so its contribution to the total reflection coefficient is negligible, and (b) the (lossy) skin layer is relatively thick, so that the incident wave either does not reach the fat layer or any reflections from that layer is substantially attenuated.

Here, we analyze the effects of the presence of SC and fat layers. The reflection coefficient of the skin model given in Fig. 1(e) is calculated as a function of SC layer thickness, and different thickness of the viable epidermis and dermis layers together, hereon referred to as the second layer. The subcutaneous fat layer is assumed to be infinitely thick. The complex permittivity of SC layer is set to that of palm SC layer given in [8]. Complex permittivity of the second and the fat layers are set to those of skin and infiltrated fat given in [18], respectively. Subsequently, this reflection coefficient is used to calculate the complex permittivity by assuming that the skin is homogenous. The maximum complex permittivity calculation error in the Ka-band frequency range of 26.5-40 GHz caused by the homogenous skin assumption is then calculated. This is done by first calculating the error for each frequency point as determined by Equation (1). Then, the

maximum value in this range is denoted as the maximum complex permittivity calculation error. The results are presented in Fig. 7.

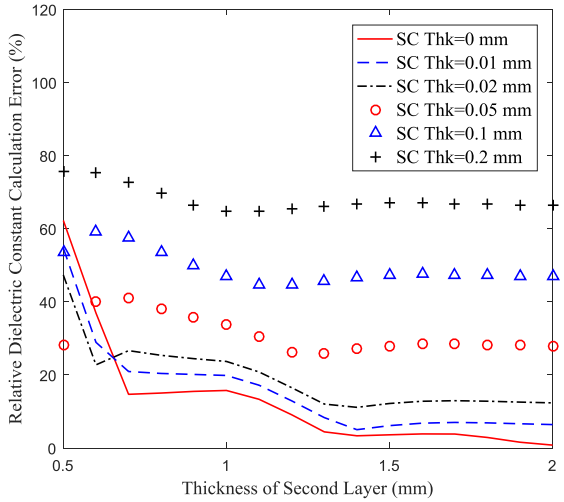

(a)

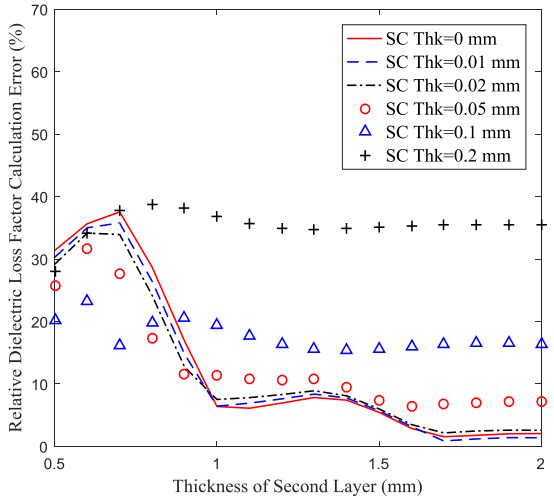

(b)

Figure 7. Maximum: (a) relative dielectric constant and (b) relative dielectric loss factor calculation error in the Ka-band frequency range, when a homogenous skin model (Fig. 1b) is used in calculating skin relative complex permittivity in place of the layered model (Fig. 1e).

Several conclusions can be drawn from these results, namely:

1- The calculation error generally decreases as a function of increasing second layer thickness. This is due to the losses in the second layer, reducing the effect of the third (fat) layer on the overall reflection coefficient. However, this relationship is not a linear one as a function of second skin layer thickness [12].
2- When the effect of fat layer is significantly reduced, complex permittivity calculation error increases as function of increasing SC layer thickness, as expected.

Since human skin has ~0.02 mm-thick SC layer and the second layer is usually larger than 1.2 mm, the maximum calculation error caused by the homogenous skin assumption is less than ~15% in the Ka-band (26.5-40 GHz) frequency range. This error decreases to less (~5%) when the second layer is thicker than ~1.6 mm. Thus, the results indicate that if these levels of error are acceptable, for a given application, then using the homogenous skin model in the Ka-band (26.5-40 GHz) frequency range when performing open-ended waveguide measurements should be fine. Furthermore, as will be shown later, if the thickness of each layer of skin is also available (through secondary measurement means), then more accurate results can be obtained.

4.2. SENSITIVITY TO THE THICKNESS OF ADDITIONAL LAYER

To closely calculate skin complex permittivity, the thickness and complex permittivity of the additional layer, used to prevent skin protrusion into the waveguide, must be accurately known. Optimum thickness and complex permittivity of this layer changes as a function of frequency and the properties of the layered structure to be examined [12]. Therefore, careful analysis must be performed to evaluate the sensitivity of

skin complex permittivity calculation to the additional layer thickness and complex permittivity. Thus, to evaluate the sensitivity of skin complex permittivity calculation to these parameters, a two-step approach was followed.

In the first step, reflection coefficient was calculated in Ka-band (26.5-40 GHz) frequency range for a two-layer model (i.e., the additional layer and homogenous skin) while changing the thickness of the former about a nominal value with a given percent thickness error (i.e., maximum uncertainty in knowing the actual thickness) about the nominal value. The additional dielectric layer was assumed to be lossless and its relative dielectric constant was set as 2, mimicking those of most polymers and paper products from which this layer may consist. As before, the skin complex permittivity was set to that given in [18].

In the second step, the calculated reflection coefficient in step 1 was used to calculate skin complex permittivity by assuming the top dielectric layer has a thickness equal to the exact nominal thickness and its relative dielectric constant. In this way, the sensitivity of skin complex permittivity calculation to any deviation from the assumed nominal thickness can be investigated (i.e., sensitivity to the thickness of this additional layer). The maximum complex permittivity error within the Ka-band (26.5-40 GHz) frequency range was again calculated by comparing the results with the skin complex permittivity used in reflection coefficient calculation. The results, presented in Fig. 8, show that the skin complex permittivity calculation error is quite sensitive to thickness error associated with the additional dielectric layer. Also, the complex permittivity error, for a given percent thickness error, generally increases as function of increasing additional layer thickness. In other words, and based on the results in Fig. 8, the additional layer needs to

be relatively thin and have small thickness error associated with it (i.e., well-produced). To this end, materials such as ordinary paper, which has a low relative dielectric constant (~2), is loss less, and has a precise thickness (with respect to its actual thickness) could be a good candidate for this purpose.

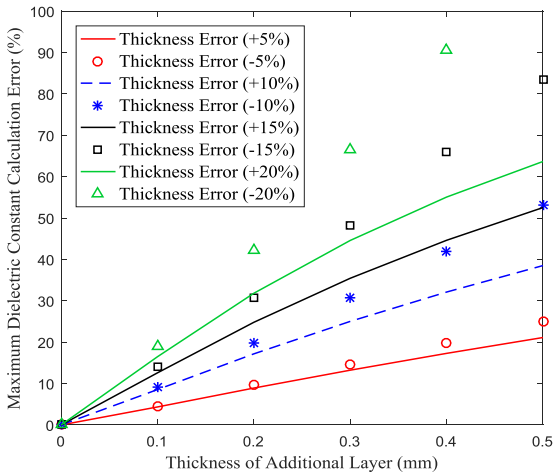

(a)

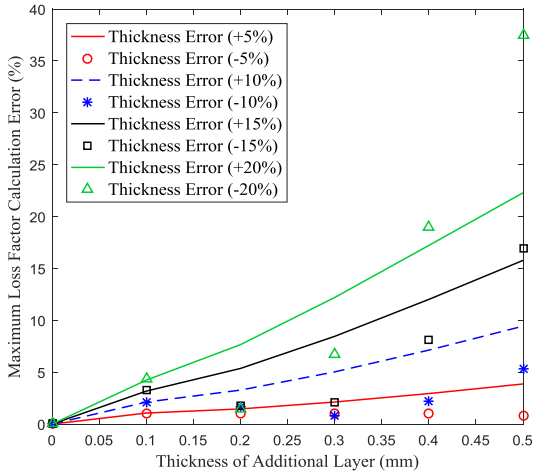

(b)

Figure 8. (a) Relative dielectric constant calculation error, and (b) relative dielectric loss factor calculation error caused by inaccuracy in knowing the additional layer thickness, with the relative dielectric constant of the additional layer set at 2.

4.3. SENSITIVITY TO THE COMPLEX PERMITTIVITY OF THE ADDITIONAL LAYER

A similar approach was followed to analyze the calculation error of skin complex permittivity caused by error (i.e., maximum uncertainty in knowing the actual complex permittivity) in the complex permittivity of the additional layer. First, reflection coefficient was calculated in Ka-band (26.5-40 GHz) for a two-layer model consisting of a 0.1-mm thick additional dielectric layer and an infinitely thick skin layer, while the dielectric constant of the additional layer (assumed lossless) was varied. Similar to thickness analysis, the dielectric constant of the additional layer varied by a certain percentage about a nominal value. Then, the calculated reflection coefficient was used to calculate the complex permittivity of the skin layer by assuming that the additional layer dielectric constant equals that of its nominal value. The maximum calculation error within the Ka-band frequency range (26.5-40 GHz) was then calculated by comparing the calculated complex permittivity with the skin complex permittivity used in reflection coefficient calculation. The results, presented in Fig. 9, show unlike the sensitivity shown by the calculated complex permittivity to the additional layer thickness, the calculation results are much less sensitive to variations about the nominal dielectric constant values of the additional layer.

In conclusion, in order to minimize the calculation error due to the introduction of the additional layer, it must be thin, and its thickness and dielectric constant errors must also be small. The complex permittivity of such materials may be readily and accurately measured using several well-known techniques [12], [42].

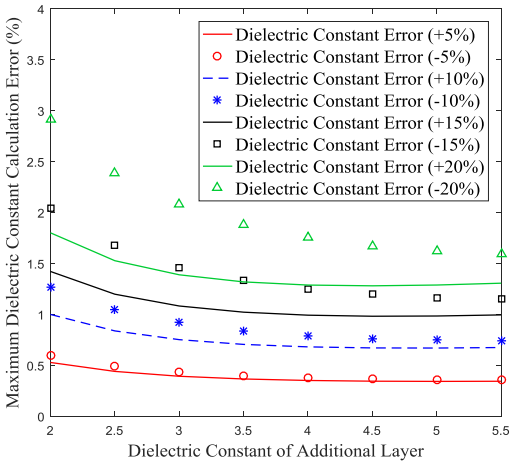

(a)

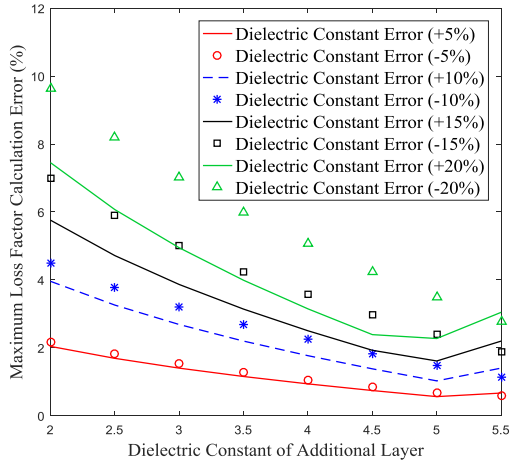

(b)

Figure 9. (a) Relative dielectric constant calculation error, and (b) relative dielectric loss factor calculation error caused by relative dielectric constant error of the additional layer, where the additional layer thickness is 0.1 mm, and its relative permittivity varies from 2 to 5.

4.4. SENSITIVITY TO INSTRUMENT NOISE AND MEASUREMENT INCONSISTENCY

Another source of complex permittivity calculation error is instrument noise and measurement inconsistency associated with the operator. The effect of instrument noise

can be significantly reduced by using a high-quality and “low noise” instrument, such as commercial vector network analyzer (VNA), coupled with a high-quality calibration standards and process. Measurement inconsistency can be determined and improved by performing multiple measurements (i.e., averaging of the measured data) and using multiple skilled operators.

When a custom-designed measurement system is used (i.e., not a high-quality commercial VNA), the noise level of the system needs to be measured, and the corresponding calculation error caused by this noise level must be investigated. In addition, several reflection coefficient measurements and subsequent complex permittivity calculation should be performed and the results averaged. This helps in reducing the influence of operator measurement inconsistencies and better ascertains the robustness of the measurement method and the calculation algorithm. Unfortunately, the influence of these factors have seldom been discussed previously (for example see [8]). Furthermore, although the average and standard deviation of the measured reflection coefficient may be given in previous studies, the corresponding complex permittivity calculation standard deviation is absent. Given the non-linear relationship between the two, this effect can be significant and must be investigated. In [16], the authors mention that the complex permittivity calculation results could be within ~±5% - ±10 % for their measurements at frequencies higher than 100 MHz. However, the reason given for this variation is the inhomogeneous nature of skin without any further or evidential analysis. However, the recent results of research using the similar approach for measuring skin tissue show that the standard deviation for dielectric constant and dielectric loss factor could be as high as 16.9% and 26.1%, respectively [5].

As will be shown later, in this study, we performed several reflection coefficient measurements, at every location on the human subjects used, in addition to using multiple operators confirming each other's measurement results, as will be shown later. It was concluded that measurement inconsistency due to multiple measurements and using different operators was insignificant. This was partially due to the fact that they were skilled operators in using VNAs, the calibration process.

As it relates to reflection coefficient measurements using a VNA, the minimum measurable signal (noise floor) can be considered as the residual calibration errors which are determined by the quality of the calibration standards used (in particular the matched load). Since these residual signals have small amplitudes, they can be lumped with other sources of instrument noise as an additive white Gaussian noise (WGN), *N*, to the ideal measured reflection coefficient, as:

$$\Gamma = \Gamma_{ideal} + N$$

where, Γ is the measured complex reflection coefficient, and Γ_{ideal} represents the complex reflection coefficient free of instrument noise. Thus, to quantitatively investigate the effect of instrument noise on complex permittivity calculation, noise power (*NP*), in the reflection coefficient, averaged over the frequency band given by was used:

$$NP = 10log_{10}\frac{\sum_{i=1}^{n}|N(i)|^2}{n}(dB)$$

where, *i* is the *i*th measurement frequency sampling point.

To determine the influence of instrument noise on maximum complex permittivity calculation error, simulations were performed for homogenous skin model at Ka-band (26.5-40 GHz). First, the reflection coefficient of homogenous skin model, Γ_{ideal}, was

calculated. The skin complex permittivity is set as that given in [18], and then WGN with different *NP* levels was added to the Γ_{ideal} to obtain Γ. Then, Γ was used to calculate the complex permittivity. Subsequently, the complex permittivity calculation error was obtained by comparing the calculation results with the theoretical complex permittivity, resulting in the relationship between maximum complex permittivity calculation error (within the frequency band) and *NP* level, as shown in Fig. 10.

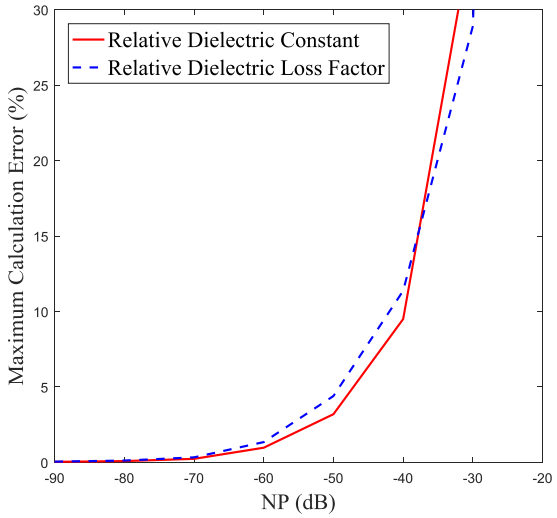

Figure 10. Maximum relative complex permittivity calculation error in homogenous skin model caused by different noise levels.

The results show that maximum complex permittivity calculation error rapidly increases for *NP* levels greater than -50 dB. This puts restrictions on the quality of the calibration standards used and the instrument itself. The system used in this study consisted of a calibrated Anritsu MS4644A vector network analyzer (VNA), modified Ka-band (26.5-40 GHz) open-ended rectangular waveguide probe and a semi-rigid coaxial cable.

The *NP* for this instrument was obtained by measuring the reflection coefficient of a matched load (where $\Gamma_{ideal} = 0$), as explained earlier. The measurements were conducted five times, and the *NP* varied between -50.1 dB and -46.4 dB with an average of -47.8 dB. According to results shown in Fig. 10, the calculation error caused by the instrument noise may be as high as ~7%.

4.5. ESTIMATION OF CALCULATION ACCURACY DUE TO MULTIPLE SOURCES OF ERROR

In practice, more than one source of error may exist in a given measurement. Therefore, it is important to assess or estimate the complex permittivity calculation accuracy with multiple sources of error present. We can estimate the calculation accuracy using the previous derivation. Here, the total error is assumed to be a vector summation of errors caused by different sources, so the scalar summation of all errors together represents a worst-case scenario. To estimate this calculation error, SC layer is assumed to be 0.02 mm, and the viable dermis and dermis together are 2-mm thick, then the dielectric constant and dielectric loss factor calculation error is ~7% and ~2%, respectively based on Fig. 7. The thickness measurement standard deviation (±0.003 mm) of printing paper is used for thickness error which is ±3.3 %, the corresponding dielectric constant and dielectric loss factor calculation error is ~4% and ~1%, respectively based on Fig. 8. Similarly, measured standard deviation of dielectric constant for printing paper, which is ±3.1%, was used to represent its associated dielectric constant error. This results in a calculation error for skin dielectric constant and dielectric loss factor equal to ~0.5% and ~2%, respectively based on the results shown in Fig. 9. Finally, when considering all of these errors, the *total*

estimated calculation error for skin dielectric constant and dielectric loss factor is ~11.5% and ~5%, respectively.

In addition, some simulations were also performed to determine the calculation error. In the forward calculations, the layered skin model in Fig. 11 was used along with the nominal thickness and complex permittivity of the additional layer and their variations about these nominal values (i.e., for thickness 0.09 ±0.003 mm). However, in the calculation of the complex permittivity of the skin, a homogeneous skin model and only the nominal thickness and complex permittivity of the additional layer were assumed. In this way, resulting errors in the calculated complex permittivity of skin, due to the skin structure and the addition layer thickness and complex permittivity accuracy could be determined. The average measured results of thickness and complex permittivity of paper were then used as the nominal parameter of additional layer, and the measured standard deviation was used as the error of thickness and complex permittivity. The complex permittivity of SC was set to that of the SC layer of palm given in [8], the complex permittivity of viable epidermis and dermis were set to those given in [18], and fat complex permittivity was set as that of infiltrated fat given in [18]. The thickness of SC and the second layer of skin was set using previously mentioned typical values of 0.02 mm and 2 mm, respectively. Finally, we assessed the calculation error by comparing the calculated complex permittivity results with the complex permittivity of dermis layer used in forward calculation. The maximum calculation error for different additional layer parameters are shown in Table I. The results show that the proposed method can achieve ~85% and ~95% calculation accuracy for dielectric constant and dielectric loss factor, respectively, given the multiple error sources considered in these calculations.

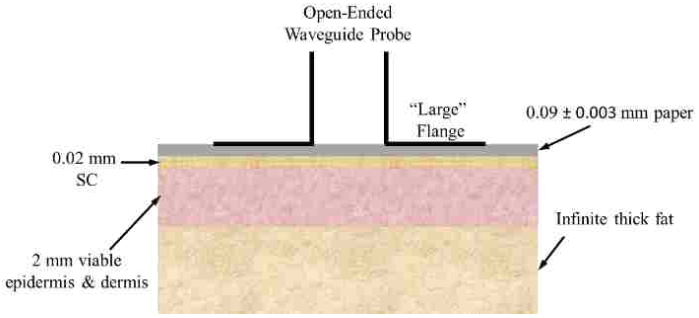

Figure 11. Simulation model used for estimating calculation errors due to multiple sources of error.

Table 1. Relative complex permittivity calculation error for additional layer with different parameters.

Thickness of Additional Layer (mm)	Relative Dielectric Constant of Additional Layer	Maximum Relative Dielectric Constant Calculation Error	Maximum Relative Dielectric Loss Factor Calculation Error
0.093	1.87-j0.05	15.5 %	2.8 %
0.093	1.87-j0.09	16.0 %	2.8 %
0.093	1.99-j0.05	15.7 %	3.4 %
0.093	1.99-j0.09	16.2 %	3.5 %
0.087	1.87-j0.05	10.6 %	2.7 %
0.087	1.87-j0.09	11.2 %	2.9 %
0.087	1.99-j0.05	10.8 %	5.1 %
0.087	1.99-j0.09	11.3 %	5.3 %

5. IN VIVO HUMAN SKIN COMPLEX PERMITTIVITY MEASUREMENT RESULTS

The measurement setup, for measuring human skin reflection coefficient, is shown in Fig. 12. A piece of ordinary (70 g/m^2 white printer) paper was used to prevent skin tissue protrusion into the waveguide. The paper thickness was measured to be 0.09±0.003 mm and its complex permittivity was also measured to be (1.93±0.06)-*j*(0.07±0.02) using the method given in [12]. Slight pressure was applied to keep a good contact with skin during

the measurement. As will be seen later, we checked to ensure that applying additional pressure did not change the complex reflection coefficient measurements (over the measured frequency band). Then, the following locations were measured a Ka-band (26.5-40 GHz) on three human subjects, namely: forearm, shoulder, abdomen, thigh, calf, palm (close to thumb), palm (close to pinky). All experiments in this study were performed in accordance to the guidelines of and approved by Missouri University of Science and Technology (S&T) Institutional Review Board (IRB).

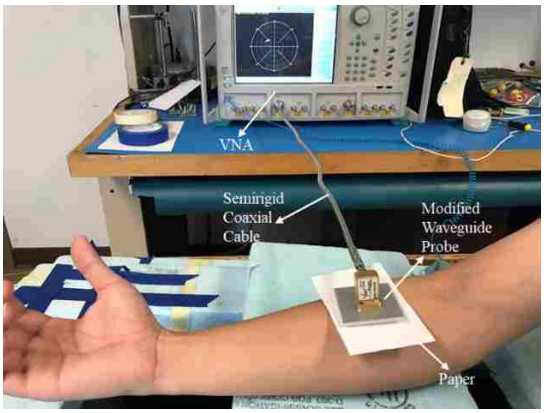

Figure 12. Skin reflection coefficient measurement setup.

The effectiveness of using a thin layer of paper, as the additional layer, for eliminating the issue of pressure was examined first. Reflection coefficient of human forearm was measured using the setup shown in Fig. 12. Two cases were examined where a small and a large amount of pressure was applied to the waveguide probe, with a thin layer of paper and with no paper. The results are shown in Fig. 13, where it can be seen that by adding just one thin layer of ordinary (printing) paper, the problem associated with pressure is completely resolved. Furthermore, the trend of the measured reflection

coefficient without paper is quite similar to the simulated results shown in Fig. 5. This also validates the model used for assessing the effect of pressure (see Fig. 4).

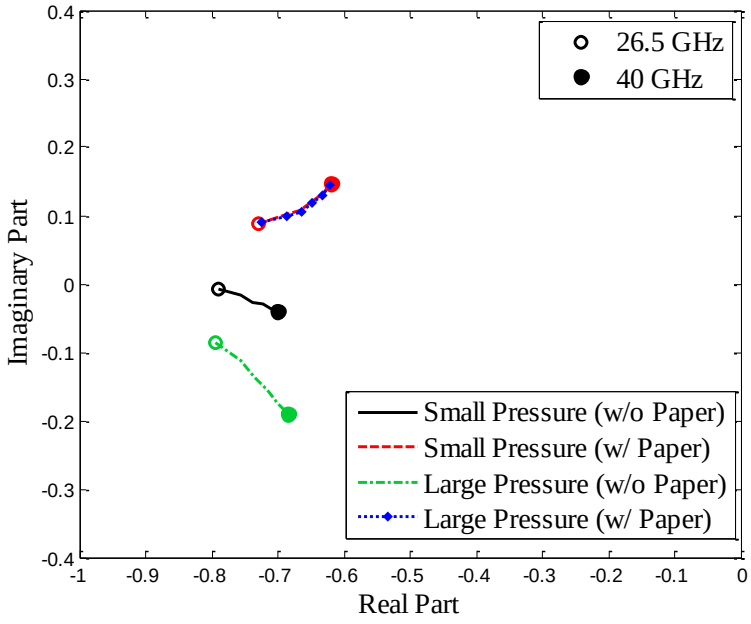

Figure 13. Measured reflection coefficient results for different levels of pressure.

When performing measurements on the human subjects, five measurements were taken at each location and then the complex permittivity was calculated for each measurement, resulting in the average and standard deviation of calculated complex permittivity for each location. Homogenous skin model was used for all calculations. The results for the complex permittivity of forearm of subject 1 are given in Fig. 14. Results show that very similar complex permittivity for the right and left forearms (at relatively the same locations). This is generally true for all results obtained in this study. Therefore, for the remaining measurements the results of right and left forearms are all averaged together.

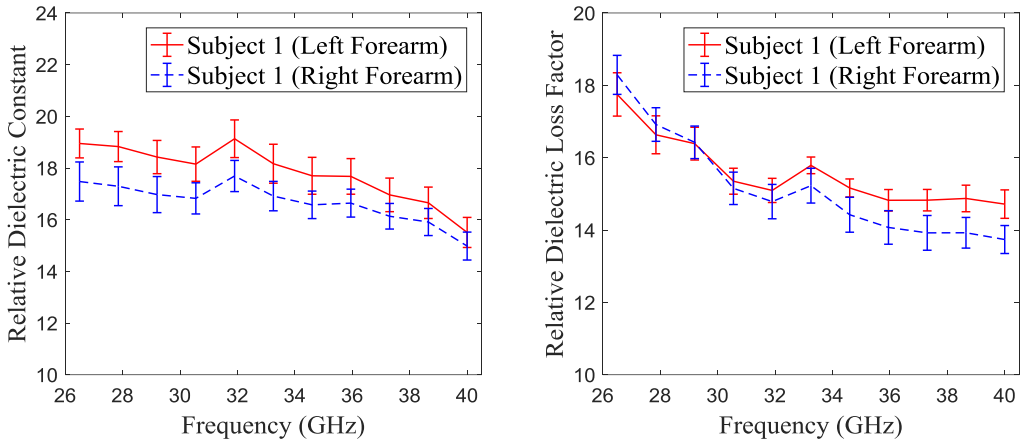

(a) (b)

Figure 14. Relative complex permittivity calculation results of subject 1: (a) relative dielectric constant of forearm, and (b) relative dielectric loss factor of forearm.

Fig. 15(a)-(g) show the results of all calculated dielectric constant and dielectric loss factor (for the three subjects and for different locations). Results show that the complex permittivity of skin varies not only as a function of different body locations in the same subject, but also from subject to subject. Furthermore, the complex permittivity of palm is in general lower than the other locations. This is directly related to the fact that palm has a relatively thick and dry SC layer. This also indicates that that using the homogenous skin model for calculating the complex permittivity of palm may not be exactly correct. This finding is also consistent with the previous discussions. The percentage of standard deviation relative to corresponding average results are given in Table II. The measured standard deviation for most cases is less than or close to the estimated maximum calculation error given in Table I. However, relative dielectric constant results of palm show large standard deviation.

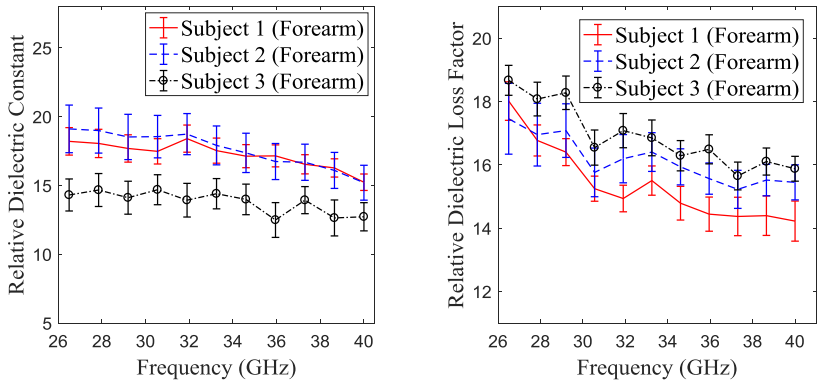

(a)

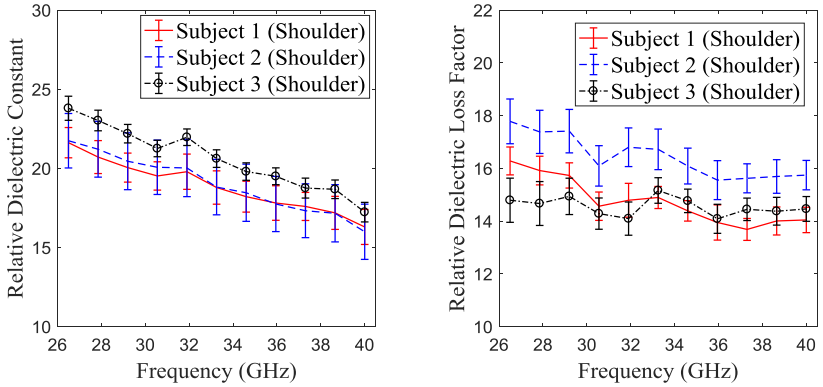

(b)

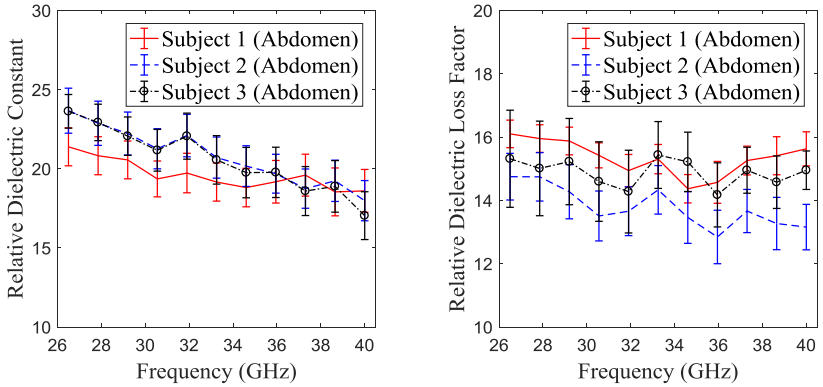

(c)

Figure 15. Relative dielectric constant and relative dielectric loss factor calculation results for: (a) forearm, (b) shoulder, (c) abdomen, (d) thigh, (e) calf, (f) palm (close to pinky), and (g) palm (close to thumb).

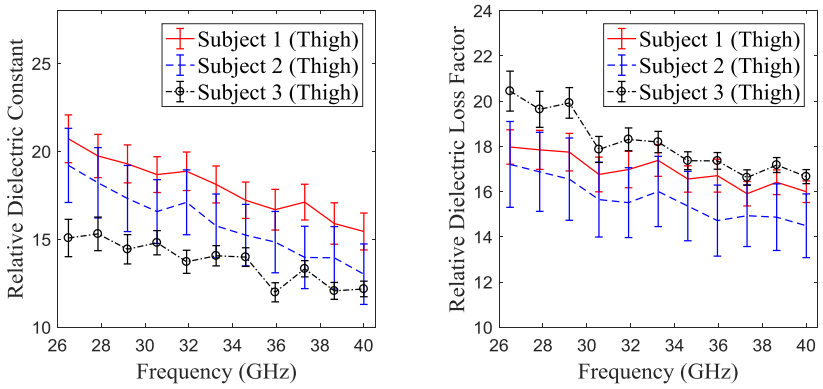

(d)

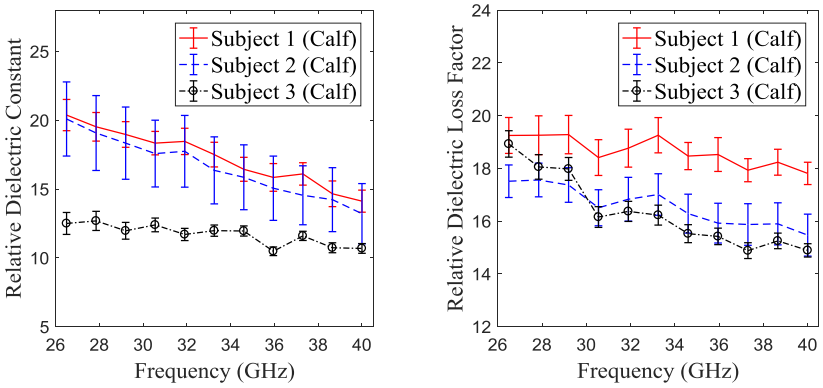

(e)

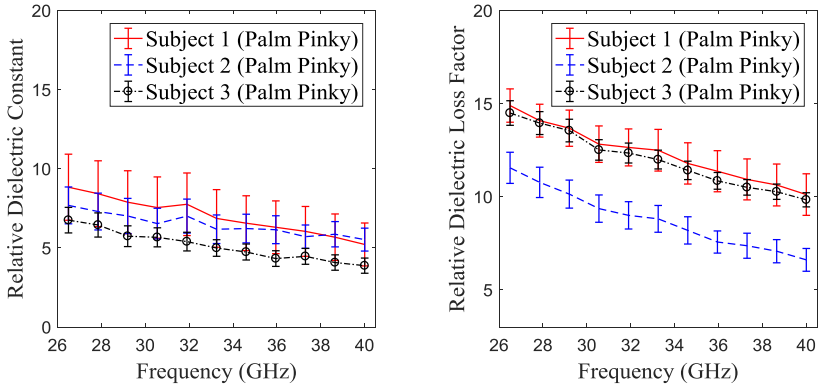

(f)

Figure 15. Relative dielectric constant and relative dielectric loss factor calculation results for: (a) forearm, (b) shoulder, (c) abdomen, (d) thigh, (e) calf, (f) palm (close to pinky), and (g) palm (close to thumb) (cont.).

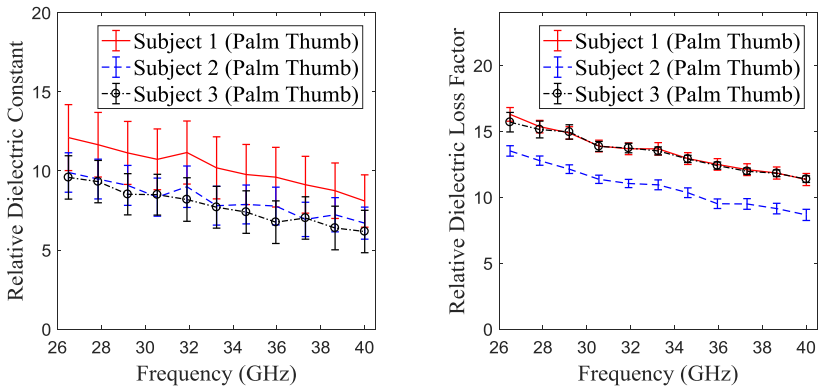

(g)

Figure 15. Relative dielectric constant and relative dielectric loss factor calculation results for: (a) forearm, (b) shoulder, (c) abdomen, (d) thigh, (e) calf, (f) palm (close to pinky), and (g) palm (close to thumb) (cont.).

Table 2. Maximum standard deviation for relative complex permittivity calculations.

Locations	Maximum Standard Deviation of Relative Dielectric Constant			Maximum Standard Deviation of Relative Dielectric Loss Factor		
	Subject 1	Subject 2	Subject 3	Subject 1	Subject 2	Subject 3
Forearm	5.7 %	9.1 %	10.3 %	2.6 %	3.2 %	2.5 %
Shoulder	6.8 %	10.9 %	3.6 %	2.7 %	3.5 %	2.9 %
Abdomen	8.2 %	7.1 %	8.9 %	2.6 %	5.0 %	4.1 %
Thigh	7.4 %	13.2 %	7.0 %	3.0 %	9.1 %	1.9 %
Calf	6.4 %	16.5 %	6.4 %	2.4 %	3.5 %	1.7 %
Palm (pinky)	26.5 %	15.9 %	12.4 %	6.0 %	7.2 %	3.9 %
Palm (Thumb)	20.4 %	15.7 %	21.7 %	3.1 %	2.7 %	2.0 %

6. MEASUREMENT METHOD FOR LAYERED SKIN MODEL

As clearly demonstrated in the discussions thus far, skin at most of locations may be modeled as a homogenous layer in the Ka-band (26.5-40 GHz) frequency range and

when using an open-ended waveguide measurements method. However, simulation results indicated higher calculation error for locations having a relatively thick SC layer. The measurement results presented in Section 4 also indicated that the calculated palm complex permittivity is lower than those at other locations. This is the result of palm having a relatively thicker SC layer in which case a homogeneous skin layer model does not properly represent the palm region. To show the effect of using homogenous model for locations with thick SC layer, a series of additional simulations were performed. Reflection coefficient of a two-layer model with different SC layer thickness and an infinite thick layer for the rest of the skin was first calculated. The SC layer complex permittivity was set the same as palm SC layer given in [8], the complex permittivity of second layer was set at the skin complex permittivity given in [18], and then the complex permittivity of skin was calculated by assuming it to be homogenous. Fig. 16 shows the results of this analysis, illustrating that the calculated complex permittivity of skin decreases with increasing thickness of SC layer, which is consist with measurement results.

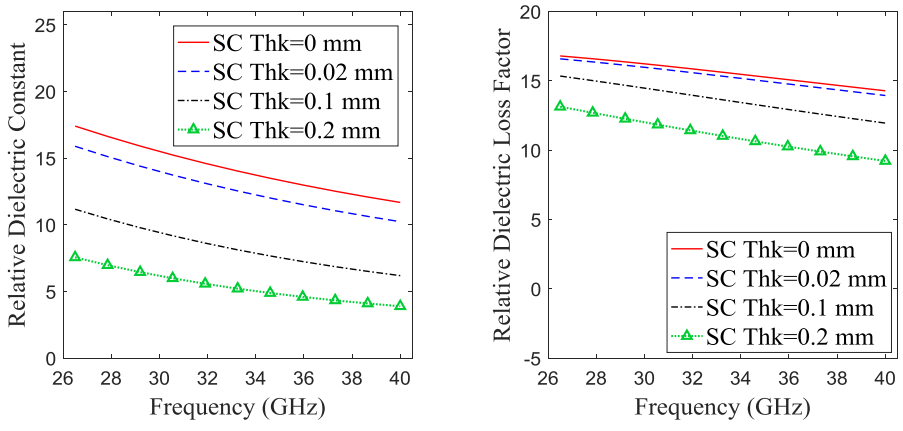

(a) (b)

Figure 16. Calculated relative complex permittivity by assuming homogenous model for layered model: (a) relative dielectric constant, and (b) relative dielectric loss factor.

In addition, measured results are also used to examine the effects of SC layer. A 0.05 mm-thick SC layer is assumed for palm (area close to thumb) of subject 1, then the viable epidermis and dermis complex permittivity is calculated by assuming the complex permittivity of SC layer equal to the palm SC layer complex permittivity given in [8]. The calculated results are compared with results from homogenous model as shown in Fig. 17. The results indicate that by assuming a SC layer, the calculated viable epidermis and dermis complex permittivity is much higher, and it is close to the forearm complex permittivity of subject 1, as expected. Furthermore, the dielectric loss factor results do not change significantly with adding this assumed SC layer, and this phenomenon is consistent with simulation result given in Fig. 16.

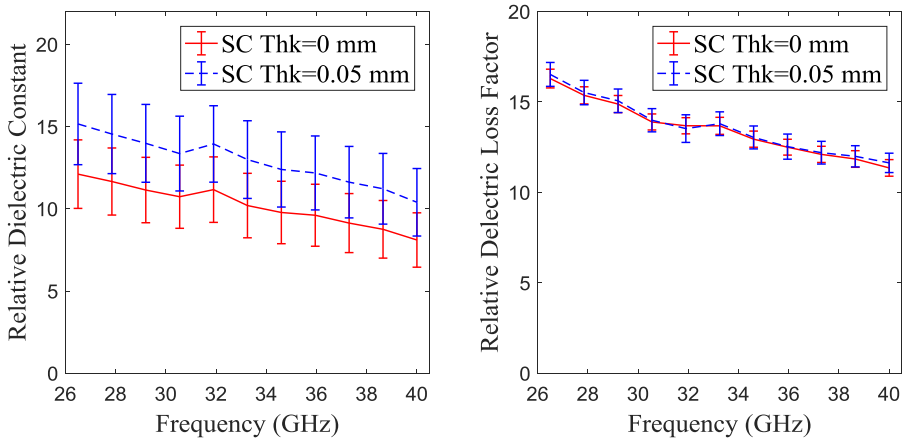

(a) (b)

Figure 17. Calculated relative complex permittivity by assuming homogenous model for layered model: (a) relative dielectric constant, and (b) relative dielectric loss factor.

In order to correctly calculate the skin complex permittivity for layered model, as the method in [12] is capable of doing so, one must also know the thickness of the SC layer

or simultaneously solve for it as well. However, more accurate prior information can achieve better calculation accuracy for solving parameters in a multilayer model. For instance, if the thickness of each layer and the complex permittivity of viable epidermis and dermis is known, then the complex permittivity of SC can be calculated more accurately.

Since the SC layer on forearm is very thin, the complex permittivity of forearm can be seen as being equivalent to viable epidermis and dermis. Subsequently, using a secondary method one can measure the thickness of each layer of skin (i.e., high frequency ultrasound and Raman spectroscopy [11] [43]). Then, the only remaining unknown parameter becomes the complex permittivity of SC layer which can be subsequently calculated.

To verify the proposed method, a four-layer model consisting of 0.1 mm-thick paper, 0.2 mm-thick SC layer, 2 mm-thick viable epidermis and dermis, and an infinite thick fat layer was created in CST Microwave Studio®. For each layer the complex permittivity used earlier (see Fig. 11) were considered while the paper was assumed to be loss less with a relative dielectric constant of 2. The simulated reflection coefficient was then used to calculate complex permittivity of SC layer knowing the thicknesses and complex permittivity of all other layers, and using 43 additional higher-order modes in the calculations for good convergence. The calculated results were compared with the theoretical values of SC complex permittivity used in the simulation, as shown in Fig. 18. The maximum calculation error for dielectric constant and dielectric loss factor is shown to be ~2.2% and ~5.3%, respectively. Considering less number of higher-order modes

results in significantly higher error values, which indicates the importance of using sufficient additional higher-order modes in these calculations.

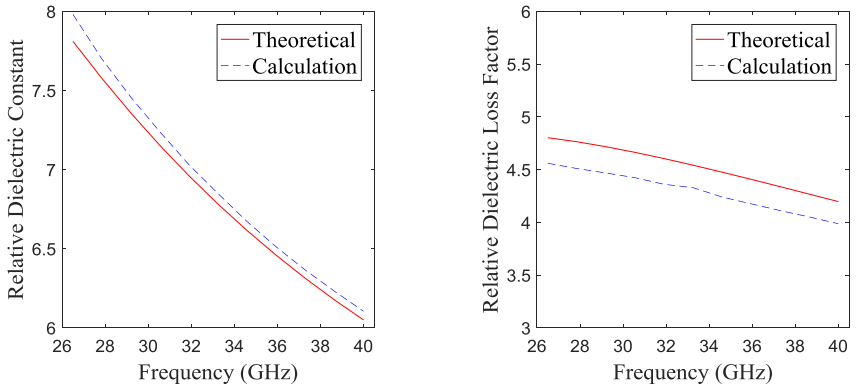

(a) (b)

Figure 18. Comparison of SC layer calculated and theoretical relative complex permittivity, (a) relative dielectric constant, and (b) relative dielectric loss factor.

7. CONCLUSIONS

In this paper, reflectometry-based skin complex permittivity measurement methods were reviewed, indicating their strengths and shortcomings. Subsequently, comprehensive analyses were performed considering important practical issues in open-ended waveguide measurement approach that can significantly and adversely affect complex permittivity calculations, such as aperture field distribution approximation, finite ground plane effects and probe pressure problem. Accordingly, a modified open-end waveguide probe method was proposed to effectively overcome these issues for skin complex permittivity measurement, in conjunction with a full-wave electromagnetic model that properly describes the interaction of the fields at the waveguide aperture with a generally layered

structure (i.e., human skin). Extensive analyses were conducted to investigate and account for critical sources of error in the proposed measurement method, including assuming skin to be a homogeneous layer, thickness and complex permittivity error in additional dielectric layer that keeps skin from protruding into the open-ended waveguide probe, and instrument noise and (operator) measurement inconsistency. Results showed that proposed method can achieve ~85% and ~95% theoretical calculation accuracy for dielectric constant and dielectric loss factor respectively in Ka-band (26.5-40 GHz) skin complex permittivity determination. Using this robust method skin complex permittivity on multiple body locations of three human subjects were measured. Finally, the effect of thick SC layer in complex permittivity calculation was discussed and a modified method to determine the complex permittivity of layered skin was proposed and verified by simulations.

REFERENCES

[1] American Academy of Dermatology. "Basic science of the skin". Dec. 2017. [Online]. Available: https://www.aad.org/File%20Library/Main%20navigation/Education/Basic%20Derm%20Curriculum/revised%20files%202-2016/Basic-Science-of-the-Skin.pptx

[2] F. Töpfer, S. Dudorov, J. Oberhammer, "Millimeter-Wave Near-Field Probe Designed for High-Resolution Skin Cancer Diagnosis," *IEEE Trans. Microwave Theory and Techniques,* vol. 63, no. 6, pp. 2050-2059, June 2015.

[3] A. Taeb, S. Gigoyan, S. Safavi-Naeini, "Millimeter-wave waveguide reflectometers for early detection of skin cancer," *IET Microwave Antenna Propagation,* vol. 7, iss. 14, pp. 1182-1186, Nov. 2013.

[4] Y. Gao, R. Zoughi, "Millimeter Wave Reflectometry and Imaging for Noninvasive Diagnosis of Skin Burn Injuries," *IEEE Trans. Instrumentation and Measurement,* vol. 66, no. 1, Jan. 2017.

[5] A. Mirbeik-Sabzevari, R. Ashinoff, N. Tavassolian, "Ultra-wideband millimeter-wave dielectric characteristics of freshly-excised normal and malignant human skin tissues." *IEEE Trans. Biomedical Engineering,* vol. pp, issue. 99, pp. 1-1, Sept. 2017.

[6] FCC, "Fact sheet: Spectrum Frontiers Rules Identify, open up vast amounts of new high-band spectrum for next generation (5G) wireless broadband," July. 15. 2017. [Online]. Available: https://apps.fcc.gov/edocs_public/attachmatch/DOC-340310A1.pdf

[7] F. Topfer and J. Oberhammer, "Millimeter-wave tissue diagnosis: The most promising fields for medical applications," IEEE Microw. Mag., vol. 16, no. 4, pp. 97–113, May 2015.

[8] S. I. Alekseev, M. C. Ziskin, "Human Skin Permittivity Determined by Millimeter Wave Reflection Measurements," *Bioelectromagnetics,* vol. 28, no. 5, pp. 331-339, July 2007.

[9] D. B. Bennett, *et al.,* "Stratified Media Model for Terahertz Reflectometry of the Skin," *IEEE Sensor Journal,* vol. 11, no. 5, pp. 1253-1262, May 2011.

[10] H. Fruhstorfer, U. Abel, C. D. Garthe, A. Knuttel, "Thickness of the Stratum Corneum of the Volar Fingertips," *Clinical Anatomy,* vol. 13, no. 6, pp. 429-433, Nov. 2000.

[11] M. Egawa, T. Hirao, M. Takahashi, "In vivo Estimation of Stratum Corneum Thickness from Water Concentration Profiles Obtained with Raman Spectroscopy," *Acta Dermato-Venereologica,* vol. 87, no. 1, pp. 4-8, Jan. 2007.

[12] M. T. Ghasr, D. Simms, R. Zoughi, "Multimodal Solution for a Waveguide Radiating Into Multilayered Structures—Dielectric Property and Thickness Evaluation," *IEEE Trans. Instrumentation and Measurement,* vol. 58, no. 5, pp. 1505-1513, May 2009.

[13] C. Gabriel, S. Gabriel, E. Corthout, "The dielectric properties of biological tissues: I. Literature survey," *Phys. Med. Biol.,* vol. 41, no. 11, pp. 2231-2249, Nov. 1996.

[14] Keysight Technologies, "N1500A Materials Measurement Suite Technical Overview," July. 15. 2017. [Online]. Available: http://literature.cdn.keysight.com/litweb/pdf/5992-0263EN.pdf?id=2547117

[15] Keysight Technologies, "N1501A Dielectric Probe Kit 10 MHz to 50 GHz Technical Overview," July. 15. 2017. [Online]. Available: http://literature.cdn.keysight.com/litweb/pdf/5992-0264EN.pdf?id=2605692

[16] S. Gabriel, R. W. Lau, C. Gabriel, "The dielectric properties of biological tissues: II. Measurements in the frequency range 10 Hz to 20 GHz," *Phys. Med. Biol.,* vol. 41, no. 11, pp. 2251-2269, Nov. 1996.

[17] C. Gabriel, "Compilation of the dielectric properties of body tissues at RF and microwave frequencies," July. 15. 2017. [Online]. Available: www.dtic.mil/get-tr-doc/pdf?AD=ADA303903

[18] S. Gabriel, R. W. Lau, C. Gabriel, "The dielectric properties of biological tissues: III. Parametric models for the dielectric spectrum of tissues," *Physics in Medicine & Biology,* vol. 41, no. 11, pp. 2271-2293, Nov. 1996.

[19] C. Gabriel, T. Y. A. Chan, E. H. Grant, "Admittance models for open ended coaxial probes and their place in dielectric spectroscopy," *Physics in Medicine & Biology,* vol. 39, no. 12, pp. 2183-2200, Dec. 1994.

[20] H. Hwang, *et al.,* "110 GHz Broadband Measurement of Permittivity on Human Epidermis Using 1 mm Coaxial Probe," *Microwave symposium digest, 2003 IEEE MTT-S International,* Philadelphia, PA, USA, 2003, pp. 399-402.

[21] N. Chahat, M. Zhadobov, R. Augustine. R. Sauleau, "Human skin permittivity models for millimeter wave range," *IET Electronics Letters,* vol. 47, no. 7, pp. 427, March 2011.

[22] T. Lahtinen, J. Nuutinen, E. Alanen, "Dielectric properties of the skin," Physics in Medicine & Biology, vol. 42, no. 7, pp. 1471-1472, July 1997.

[23] C. Gabriel, "Comments on 'Dielectric properties of the skin'," *Physics in Medicine & Biology,* vol. 42, no. 8, pp.1671, Aug. 1997.

[24] E. Alanen, T. Lahtinen, J. Nuutinen, "Variational Formulation of Open-Ended Coaxial Line in Contact with Layered Biological Medium," *IEEE Trans. Biomedical Engineering,* vol. 45, no. 10, pp. 1241-1248. Oct. 1998.

[25] E. Alanen, T. Lahtinen, J. Nuutinen, "Measurement of dielectric properties of subcutaneous fat with open-ended coaxial sensors," *Physics in Medicine & Biology,* vol. 43, no. 3, pp. 475-485, March 1998.

[26] K. Sasaki, K. Wake, S. Watanabe, "Measurement of the dielectric properties of the epidermis and dermis at frequencies from 0.5 GHz to 110 GHz," *Physics in Medicine and Biology,* vol. 59, no. 16, pp. 2014.

[27] K. Sasaki, M. Mizuno, K. Wake, S. Watanabe, "Measurement of the dielectric properties of the skin at frequencies from 0.5 GHz to 1 THz using several measurement systems," *Infrared, millimeter, and Terahertz waves (IRMMW-THz),* Hong Kong, China, 2015, pp. 1-2.

[28] Bakhtiari, S., S. Ganchev and R. Zoughi, "Analysis of the Radiation of an Open-Ended Coaxial Line into Stratified Dielectrics," *IEEE Transactions on Microwave Theory and Techniques,* vol. 42, no. 7, pp. 1261-1267, July, 1994.

[29] Ganchev, S., N. Qaddoumi, S. Bakhtiari and R. Zoughi, "Calibration and Measurement of Dielectric Properties of Finite Thickness Composite Sheets with Open-Ended Coaxial Sensors," *IEEE Transactions on Instrumentation and Measurement,* vol. IM-44, no. 6, p. 1023-1029, December, 1995.

[30] R. Zoughi, J. R. Gallion, M. T. Ghasr, "Accurate Microwave Measurement of Coating Thickness on Carbon Composite Substrates," *IEEE Trans. Instrumentation and Measurement,* vol. 5, no. 4, pp. 951-953, April 2016.

[31] M. T. Ghasr, *et al., "*Accurate One-Sided Microwave Thickness Evaluation of Lined-Fiberglass Composites," *IEEE Trans Instrumentation and Measurement,* vol. 64, no. 10, pp. 2802-2812, Oct. 2015.

[32] G. L. Hey-Shipton, P. A. Matthews, J. McStay, "The complex permittivity of human tissue at microwave frequencies," *Physics in Medicine and Biology,* vol. 27, no. 8, pp. 1067-1071, Aug. 1982.

[33] D. K. Ghodgaonkar, O. P. Gandhi, M. F. Iskander. "Complex Permittivity of Human Skin in Vivo in the Frequency Band 26.5-60 GHz," *Anntenna and propagation society international symposium, 2000. IEEE,* Salt Lake City, UT, USA, 2002, pp. 1100-1103.

[34] N. Tamyis, D. K. Ghodgaonkar, W. T. Wui, "Dielectric Properties of Human Skin In Vivo in the Frequency Range 20–38 GHz for 42 Healthy Volunteers," *Proc. of the 28th URSI general assembly, 2005,*

[35] M. Kempin, M. T. Ghasr, J. T. Case, R. Zoughi, "Modified Waveguide Flange for Evaluation of Stratified Composites," *IEEE Trans. Instrumentation and Measurement,* vol. 63, no. 6, pp. 1524-1533, June 2014.

[36] S. J-P. Egot-Lemaire, M. C. Ziskin, "Dielectric properties of human skin at an acupuncture point in the 50 - 75 GHz frequency range. A pilot study," *Bioelectromagnetics,* vol. 32, no. 5, pp. 360-366, July 2011.

[37] P. F. M. Smulders, "Analysis of human skin tissue by millimeter wave reflectometry," *Skin Research and Technology,* vol. 19, no. 1, pp. 209-216, Feb. 2013.

[38] N. Janssen, P. F. M. Smulders, "Design of Millimeter-wave Probe for Diagnosis of Human Skin," *Microwave conference (EuMC), 2012 42nd European,* Amsterdam, Netherlands, 2012, pp. 440-443.

[39] C. Gabriel, R. H. Bentall, E. H. Grant, "Comparison of the Dielectric Properties of Normal and Wounded Human Skin Material," *Bioelectromagnetics,* vol. 8, no. 1, pp. 23-27, Jan. 1987.

[40] C. M. Alabaster, "Permittivity of human skin in millimeter wave band," *Electronics Letters,* vol. 39, no. 21, pp. 1521-1522, Oct. 2003.

[41] N. Chahat, M. Zhadobov, R. Sauleau, S. I. Alekseev, "New Method for Determining Dielectric Properties of Skin and Phantoms at Millimeter Waves Based on Heating Kinetics," *IEEE Trans. Microwave Theory and Techniques,* vol. 60, no. 3, pp. 827-832, March 2012.

[42] K.J. Bois, L. Handjojo, A. Benally, K. Mubarak and R. Zoughi, "Dielectric Plug-Loaded Two-Port Transmission Line Measurement Technique for Dielectric Property Characterization of Granular and Liquid Materials," *IEEE Trans on Instrumentation and Measurement,* vol. 48, no. 6, pp. 1141-1148, December 1999.

[43] A. Laurent, *et al.,* "Echographic measurement of skin thickness in adults by high frequency ultrasound to assess the appropriate microneedle length for intradermal delivery of vaccines," *Vaccine,* vol. 25, no. 34, pp. 6423-6430, Aug. 2007.

III. EFFECTS OF AND COMPENSATION FOR TRANSLATIONAL POSITION ERROR IN MICROWAVE SYNTHETIC APERTURE RADAR IMAGING SYSTEMS

ABSTRACT

Translational position error in microwave and millimeter wave synthetic aperture radar (SAR) imaging systems can cause significant image quality degradation, particularly in nondestructive testing and evaluation (NDT&E) applications where the distance to the imaging object is relatively short. In this study, this translational position error problem is fully studied through electromagnetic simulation. The results show that among possible geometrical causes of error, translational position error in the height direction, is the dominant factor in image quality degradation. Subsequently, a corresponding height position error compensation method is proposed and analyzed. Extensive simulations and measurement are performed, in the X-Band (8.2 – 12.4 GHz) frequency range. Then, by defining several evaluation metrics, the relationship between image quality and height position error is discussed quantitatively. The measured results show good agreement with the simulated results, which validates the effectiveness of the proposed analysis approach and the compensation method. The methodology proposed in this study can be used to evaluate the feasibility or help define the required specifications of a microwave SAR imaging system for a specific application.

Index Terms—Position error; microwave imaging; synthetic aperture radar; nondestructive testing

1. INTRODUCTION

Various types of microwave and millimeter wave imaging systems, particularly those founded on synthetic aperture radar (SAR) principles, have been developed in recent years, for many applications including nondestructive testing and evaluation (NDT&E), security, and medical imaging [1]-[5]. In these imaging systems, particularly those used in NDT&E applications, measurement uncertainties related to critical system parameters, such as instrument frequency drift [6], inaccuracies associated with the motion or the assumed exact (3D) location within the synthetic aperture can cause image quality degradation [7]. In SAR imaging systems, incorrect antenna position causes incorrect phase compensation in the SAR imaging algorithm, thereby leading to image quality degradation primarily in the form of an unfocused image [7]. For NDT&E applications, in particular, a probe (i.e., an open-ended rectangular waveguide) is commonly raster scanned in one (1D) or two (2D) directions over the sample under test (SUT). Mechanical raster scanning is performed using a 1D or 2D automated scanner [8]-[9], while alternatively a linear (1D) or two dimensional (2D) imaging array can be used to perform electronic scanning [1]-[2]. Usually, such imaging systems, particularly in the former case, have very good positional accuracies since high-precision positioning mechanisms are employed for mechanical raster scanning systems. However, when operating in the millimeter wave frequency range (30 GHz-300 GHz) or when manual scanning is performed [10], the effect of this error can be significant and must be analyzed to determine the minimum requirements for location accuracy and the resulting level of image degradation [9]-[12]. Furthermore, this issue becomes critically important in light of the prevalence of using small unmanned aerial

vehicle (UAV) for various imaging purposes including SAR imaging [13]-[14]. In these systems position error could become a significant bottleneck. For instance, the position error need to be at centimeter or millimeter scale to enable using UAV imaging systems in conjunction with a ground penetrating radar (GPR) operating at 3.1-5.1 GHz (center frequency wavelength of ~73 mm) for NDT&E applications [15]. The position error discussed here is similar to the error associated with imaging platform trajectories in remote sensing application [16]-[17]. However, unlike in remote sensing applications, the probe aperture in NDT&E applications has limited size and is usually very close (i.e., a few wavelength away) to the sample under test (SUT), and consequently the position error can lead to a more severe image distortion for the same level of position error. In this investigation, we develop a general methodology for quantitatively evaluating the effects of translational position error on a microwave imaging system, and an effective translational position error compensation method is proposed to improve the resulting SAR image quality.

2. ANALYSIS OF TRANSLATIONAL POSITION ERROR PROBLEM

2.1. TRANSLATIONAL POSITION ERROR PROBLEM

The common SAR imaging system geometrical configuration, particularly for NDT applications, is shown in Fig. 1. A transceiver scans along both *x*- and *y*- direction, over the synthetic aperture imaging domain (shown as the rectangular grid in Fig. 1), with a uniform step size to gather the reflection coefficient data $s(x', y', z', f)$ from the target or SUT. The collected data is then processed by the SAR imaging algorithm to produce a

focused SAR image of the target. The SAR algorithm used in this study is very similar to the algorithm used in [3] and [8] and will not be repeated here for brevity.

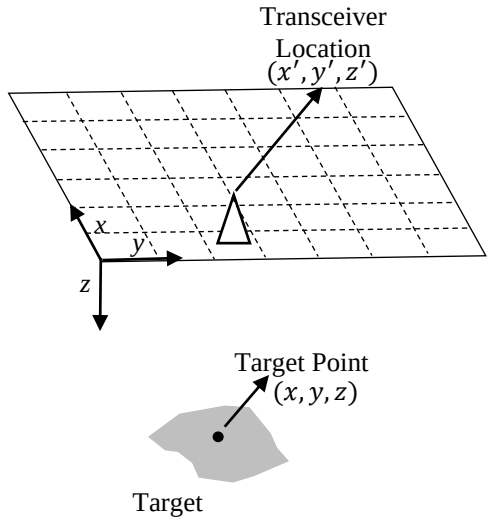

Figure 1. SAR imaging system geometrical configuration.

The reflection coefficient, measured by the transceiver, from a single point on the target, can then be written as:

$$s(x', y', z', f) = \sigma(x, y, z, f) \frac{e^{-j\frac{4\pi f}{c}R}}{R^2} \tag{1}$$

where $\sigma(x, y, z, f)$ is the reflectivity of the target and $R = \sqrt{(x - x')^2 + (y - y')^2 + (z - z')^2}$ is the distance between the target and transceiver.

To simplify the translational position error analysis, in this study only the 1D case, representing a linear scan, is considered and discussed as shown in Fig. 2. However, the analysis can be easily extended to a 2D (planar) configuration. In this 1D scan, the probe is located at *z'* and scans along the *x*-direction with a uniform step size of x_{step}. This uniform sampling position (i.e., vector *x'*) is then used in the SAR imaging algorithm [8]. When

considering transitional position error, the actual position is different by an amount $\Delta x'$ along the movement direction (i.e., lateral position error), and $\Delta z'$ vertical to the synthetic aperture plane (i.e., height position error). These translational position errors cause errors in the phase correction portion of the SAR algorithm, thereby leading to eventual image quality degradation. In this study, lateral and height position error are discussed separately, since their effects on the SAR images are different, as will be shown later.

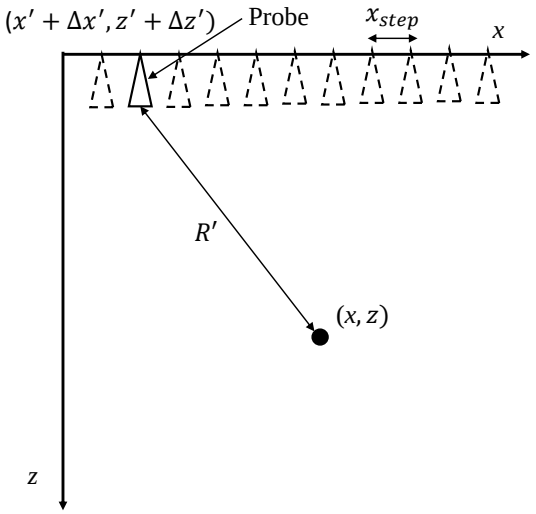

Figure 2. Position error model for raster scanning SAR imaging systems.

The reflection coefficient measured at a transceiver for a point target with position error can subsequently be written as:

$$s(x' + \Delta x', z' + \Delta z', f) = \sigma(x, z, f) \frac{e^{-j\frac{4\pi f}{c}R'}}{(R')^2} \tag{2}$$

where $R' = \sqrt{(x - x' - \Delta x')^2 + (z - z' - \Delta z')^2}$ is the actual distance between the point target and the transceiver, which means there is a distance difference equal to $\Delta R'$ between the assumed distance R used in SAR imaging algorithm and the actual distance R'. Also,

$\Delta x'$and $\Delta z'$ are assumed to be random and vary at different transceiver locations with a uniform probability distribution function (PDF) given by (3). In addition, $\Delta z'$ is assumed to be zero when $\Delta x'$ is discussed and vice versa.

$$Position\ error = Uniform(-a, a) \tag{3}$$

In (3) a is the maximum possible value for translational position error (either in lateral or height direction). Different PDFs can be used based on how a particular scanner position is statistically modeled. However, no matter what particular PDF is used the analysis of the proposed methodology will not be affected.

2.2. EFFECTS OF TRANSLATIONAL POSITION ERROR

Based on (2) there are three parameters that can cause errors in the measured reflection coefficient and the subsequent phase compensation error and eventually image quality degradation, namely: frequency *f*, lateral position error $\Delta x'$ and height position error $\Delta z'$. The effects of frequency error has already been fully discussed in [6] and was shown to be negligible for most practical microwave signal sources used in SAR imaging system. The effects of lateral position error (i.e., error due to $\Delta x'$) was analyzed in [7] on a preliminary basis. Here, an example is given to compare the image degradation effects of lateral position error, $\Delta x'$, and height position error, $\Delta z'$, individually. In doing so, three SAR images are generated at X-band (8.2-12.4 GHz), using a 1D scan of a perfect electric conductor (PEC) point target (σ =1), as shown in Fig. 2. The scanned aperture is located at $z' = 0$ and the point target is 3.6 λ away from the scanning synthetic aperture [7]. The antenna pattern is assumed to be same as that of an open-ended rectangular waveguide probe with TE_{10} mode aperture field distribution, and this assumption is used in all

simulation in this study. For the middle frequency wavelength of λ, the size of the scanned aperture is chosen to be 10 λ and the step size x_{step} is 0.05 λ. The translational position error varies at different transceiver locations according to the PDF in equation (3) with a maximum magnitude, a, of 0.25 λ. The simulation results for no translational position error, with lateral position error only and with height position error only are shown in Figs. 3(a)-(c).

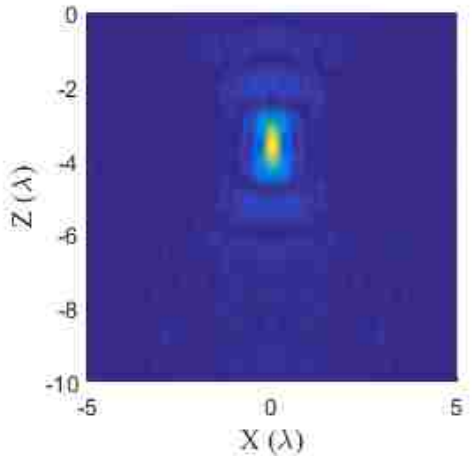

(a)

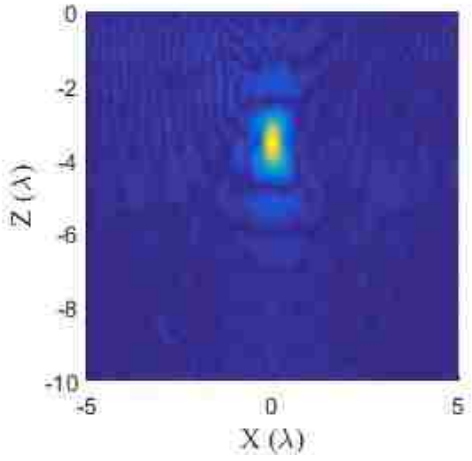

(b)

Figure 3. SAR imaging results: (a) without translational position error, (b) with lateral positon error only, and (c) with height position error only.

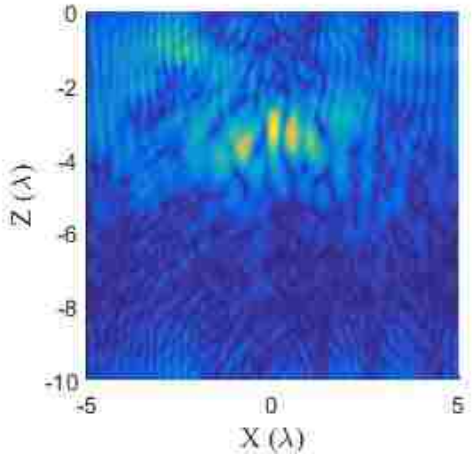

(c)

Figure 3. SAR imaging results: (a) without translational position error, (b) with lateral positon error only, and (c) with height position error only (cont.).

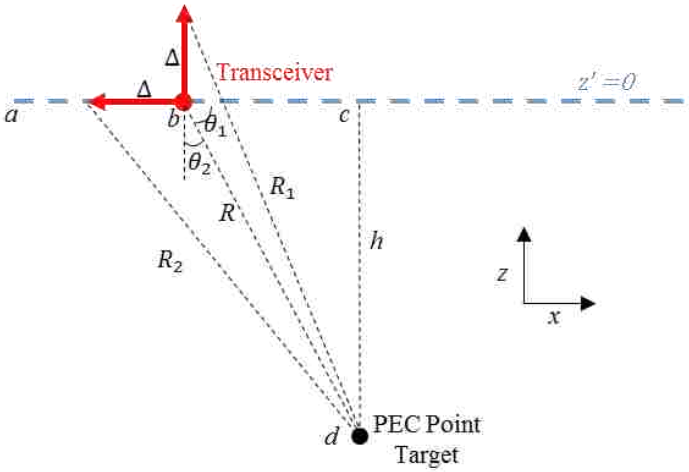

Figure 4. Schematic of lateral and height position errors.

Translational position error can cause the image of the point target to spread and shift slightly in its location [7]. The imaging results in Fig. 3 show that image distortion caused by the height position error (i.e., $\Delta z'$) is more severe than that by the lateral

position error (*i.e.* $\Delta x'$). Fig. 4 illustrates the geometry associated with each position error. For a position error, Δ, along *z* or *x* direction, the distance between the transceiver and the PEC point target is R_1 or R_2, respectively. According to (2), the same errors in *R (*distance between transceiver and point target) should have the same effect on the image reconstruction process, no matter whether it is caused by the lateral or the height position error. If θ_1 is larger than θ_2, then the height position error causes a larger error in *R*, which leads to a larger phase error. Otherwise, the lateral position error results in a larger phase error. Therefore, when the target is close to the aperture and the transceiver locations are far away from the target (i.e., at the edges of the scanning aperture), then the measured reflection coefficient phase error caused by the lateral position error will be larger than that caused by the height position error. However, due to the rapid signal attenuation along the propagation direction, the signal contribution from locations near the scanning aperture edges become negligible. Thus, height position error represents the primary factor affecting the image quality. Consequently, since the effects of lateral position error have already been discussed in [7], analysis of the rest of this study will focus on the influence of height position error (i.e., $\Delta z'$).

2.3. COMPENSATION PROCEDURE FOR HEIGHT POSITION ERROR

Here, we outline a procedure for effectively compensating for the height position error, resulting in significantly improved image quality. Height position error leads to a distance difference of $\Delta R'$ between R (assumed target and transceiver distance) and R'(actual target and transceiver distance). To fully compensate for the reflected signal magnitude and phase changes caused by $\Delta R'$ is not a straightforward process. However,

since the reflected signal magnitude change caused by signal spreading along the propagation direction (i.e., caused by the $\frac{1}{R^2}$ factor) has little impact on SAR image focusing [3], [8], then the compensation for this factor may be ignored. Furthermore, for some SAR imaging configurations (e.g., in NDT&E applications where the SUT distance to the transceiver is relatively short), $\Delta R'$is approximately equal to $\Delta z'$. In practical SAR imaging systems, $\Delta z'$ is measurable and can be used to compensate for the introduced phase error, as shown in equation (4).

$$s'(x', z', f) = \sigma(x, z, f) e^{-j\frac{4\pi f}{c}\Delta z'} \frac{e^{-j\frac{4\pi f}{c}\sqrt{(x-x')^2+(z-z'-\Delta z')^2}}}{(x-x')^2+(z-z'-\Delta z')^2} \quad (4)$$

The validity of this assumption is first analyzed through simulations. First, the reflection coefficient, *s*, for a PEC point target ($\sigma = 1$) is calculated at each location of the transceiver for a 1D scan at the center frequency of X-band (8.2-12.4 GHz). The scanned settings are the same as those in the previous section, except that the target distance varies from 0.5 to 25λ. Then, another reflection coefficient, s', is calculated using the same setup except with an added height position error. The height position error varies at every location of transceiver and its value follows the PDF given in (2) with a maximum possible height position error *a* equals to 0.1λ. Finally, the phase error at each transceiver location is calculated by subtracting the phase of s' from the phase of s. The calculation result is shown in Fig. 5(a), which shows that the phase error caused by height position error is random and generally large unless the target is very close to the synthetic aperture.

Subsequently, the compensation term $e^{-j\frac{4\pi f}{c}\Delta z'}$ (i.e., approximate phase compensation) is calculated by using the same $\Delta z'$ used in calculation of s'. After subtracting this approximate compensated phase from the phase error given in Fig. 5(a),

then the residual phase error after compensation, as shown in Fig. 5(b), is finally obtained. The ‘blue’ area represents relatively small residual phase error, (i.e., most of the phase error is compensated). The results show that the proposed method can effectively compensate for the phase error unless the target is very close to the synthetic aperture.

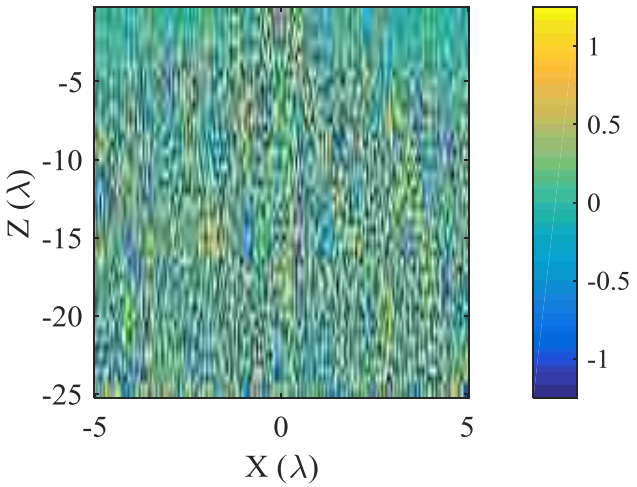

(a)

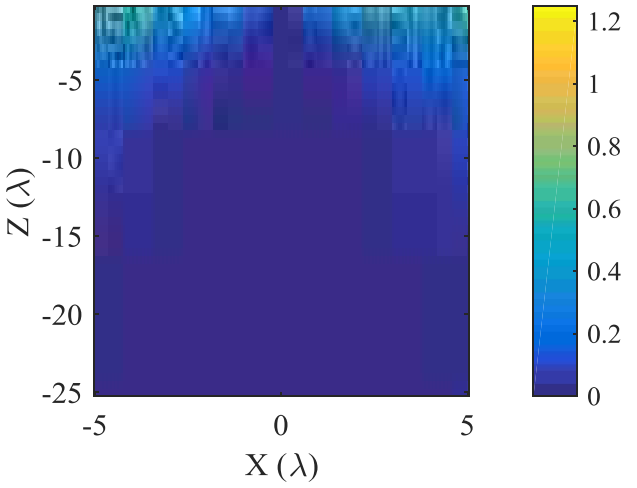

(b)

Figure 5. Phase error (unit is radian) at each transceiver when the center point target locates at different standoff distance: (a) uncompensated, and (b) compensated.

2.4. EVALUATION METRICS

To quantitatively evaluate the effects of translational position error, three evaluation metrics are defined according to the mentioned adverse image quality degradation, such as: spreading, splitting and target location offset and image distortion.

The first important metric for evaluating an image is *spatial resolution*, defined in [7], and shown in Fig. 6, as δ, for the normalized image magnitude of a PEC point target.

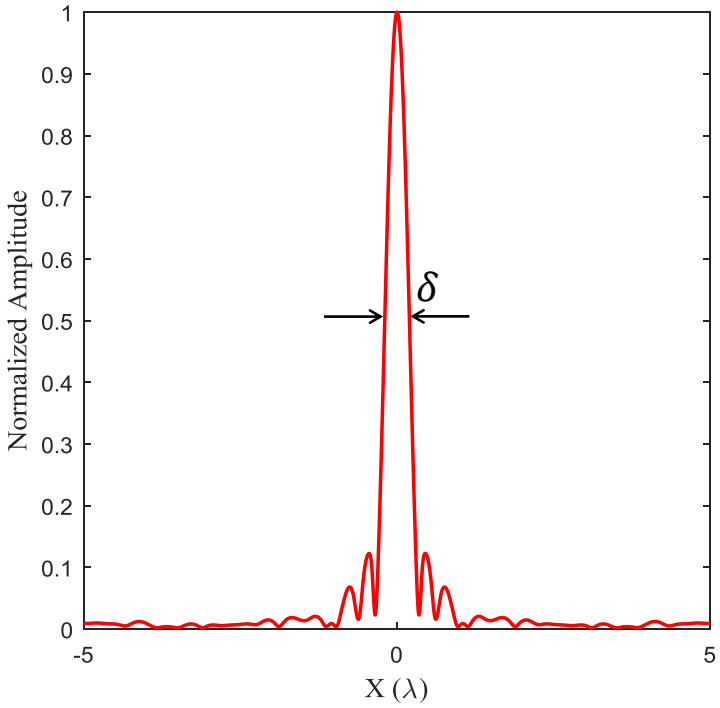

Figure 6. Definition of spatial resolution for a point target.

Furthermore, with the presence of translational position error, the predicted position of a target may be offset, to varying degrees, from its correct location, as well. This offset from the actual position is defined as *location bias*. The location bias for a point target is

simply defined as the Euclidean distance between location of the maximum magnitude $L_{calculated}$ in the SAR image of a point target and the actual location of that point target L_{actual}, as:

$$L = |L_{actual} - L_{calculated}| \tag{5}$$

The last metric describing the distortion in the image is *image error*. As shown in (6), a densely-sampled and position-error-free image, *Ref(x, z)*, generated by the SAR algorithm is used as the reference. Subsequently, the normalized root-mean-square error, *E*, between a reference image and a produced image, *I(x, z)*, with distortion is obtained, and referred to as the image error.

$$E = 20log_{10}\left(\sqrt{\frac{\sum_{x\in X}\sum_{z\in Z}(|Ref(x,z)|-|I(x,z)|)^2}{\sum_{x\in X}\sum_{z\in Z}(|Ref(x,z)|)^2}}\right) \tag{6}$$

3. SIMULATIONS

3.1. SIMULATION SETUP

A series of 1D scan simulations were performed using MATLAB to analyze the effect of height position error. These simulations were conducted at the X-band (8.2-12.4 GHz) and for a single PEC point target (σ =1). The SAR image quality is a function of scanning (synthetic) aperture size, sampling step size and standoff distance [8]. In this study, scanning aperture size is set to 10λ, and an over-sampled scan step size of 0.05λ (λ is the wavelength of middle frequency in the band) was used in these simulations. The point target was located in the center of the scanned axis (*x*) and its standoff distance varied between 2λ and 10λ. The height position error varied at different transceiver locations and had the PDF given by (3). The maximum possible value for height position error (i.e., *a*)

was chosen to be in the height of 0 to 0.2λ with 0.05λ step size, since for any value of *a* equals to or larger than 0.25λ, the point target in the image loses its definition, as shown in Fig. 3(c). Subsequently, the *spatial resolution, location bias,* and *image error* were calculated. For each metric, the simulations were performed several times (50 times for resolution and location bias calculations and 10 for image error calculation, these numbers of calculation times are a trade-off between results curve smoothness and simulation time) and the average values are reported here. Furthermore, the effectiveness of the proposed compensation method is examined through simulations with the same settings.

3.2. SIMULATION RESULTS

3.2.1. Calculation of Evaluation Metrics. Fig. 7(a) shows the contours for the obtained spatial resolution as a function of different standoff distances and maximum height position error values (i.e., *a* in (3)). The resolution values on the contours are normalized to λ. Ideally, if there is no height position error, the resolution for a certain standoff distance should remain constant. Results in Fig. 7(a) show that for a certain standoff distance, resolution decreases slightly as the height position error increases. This may be caused by the splitting effect of height position error as was shown in Fig. 3(c). In addition, the change in resolution is smaller for longer standoff distances, which is consistent with the results of lateral position error analysis [7]. This means that the image of a farther target is less sensitive to translational position error, as standoff distance affects spatial resolution significantly [8], compared to translational position error.

Fig. 7(b) shows location bias as a function of changing standoff distance and different levels of maximum possible height position error. The value on the contour is also

normalized to λ. The location bias increases as the maximum height position error increases. In addition, the location bias is actually very small. This means that even with height position error present, as long as the level of height position error is small enough to result in a well-defined point target, then the effect of point target location shift is almost negligible.

Results of image error for different standoff distances and maximum possible height position error are presented in Fig. 7(c). The unit of the value on the contour is dB. The results show that image error increases with increasing maximum possible height position error. In addition, for same maximum possible height position error level, image error remains nearly constant.

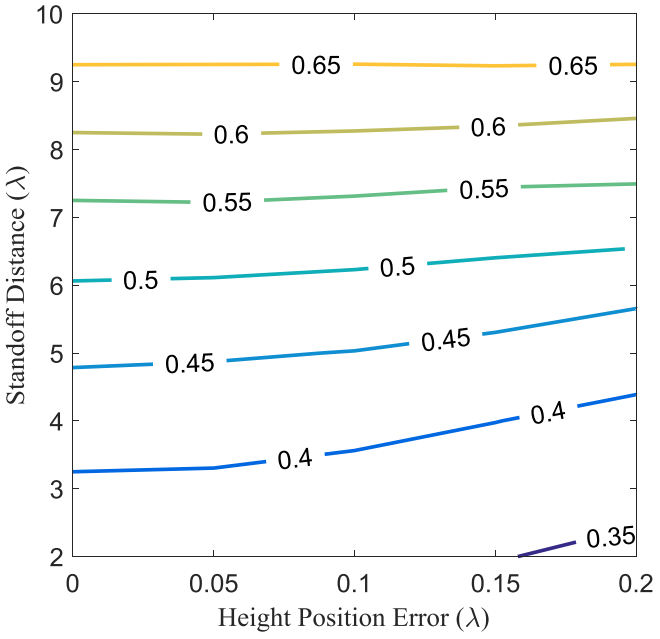

(a)

Figure 7. Calculated evaluation metrics for a centered PEC point target at different standoff distances and with different levels of maximum possible height position errors: (a) spatial resolution, (b) location bias, and (c) image error.

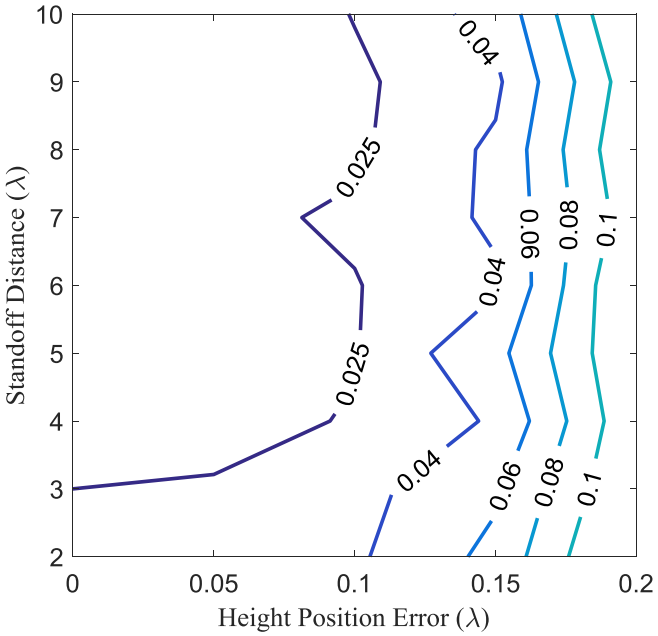

(b)

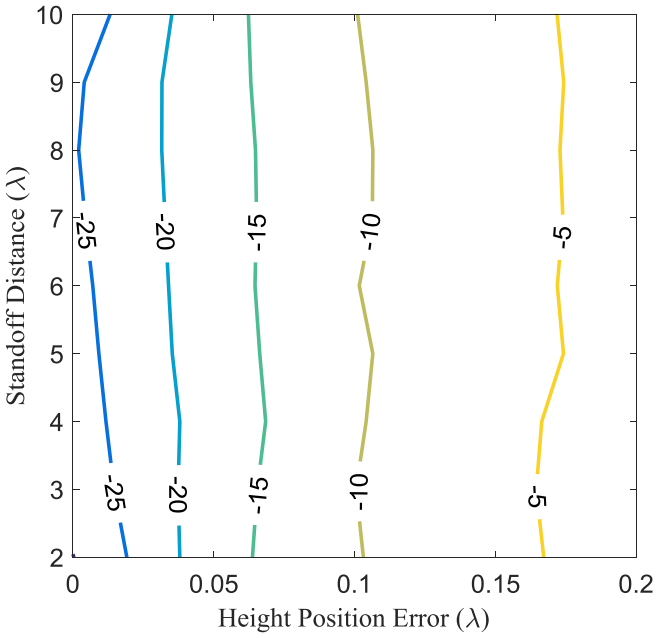

(c)

Figure 7. Calculated evaluation metrics for a centered PEC point target at different standoff distances and with different levels of maximum possible height position errors: (a) spatial resolution, (b) location bias, and (c) image error (cont.).

3.2.2. Simulation Results of Compensation. Several simulations were also performed to verify the proposed compensation method described earlier. The same settings described in part A of this section were used, except that standoff distance and maximum possible height error (i.e., *a*) were fixed. For the first two simulations, *a* is set as 0.25λ and standoff distance is set to 3.6λ and 8λ, respectively. The imaging results with and without compensation are shown in Fig. 8. The results clearly show the excellent image correction capability of the proposed error compensation method.

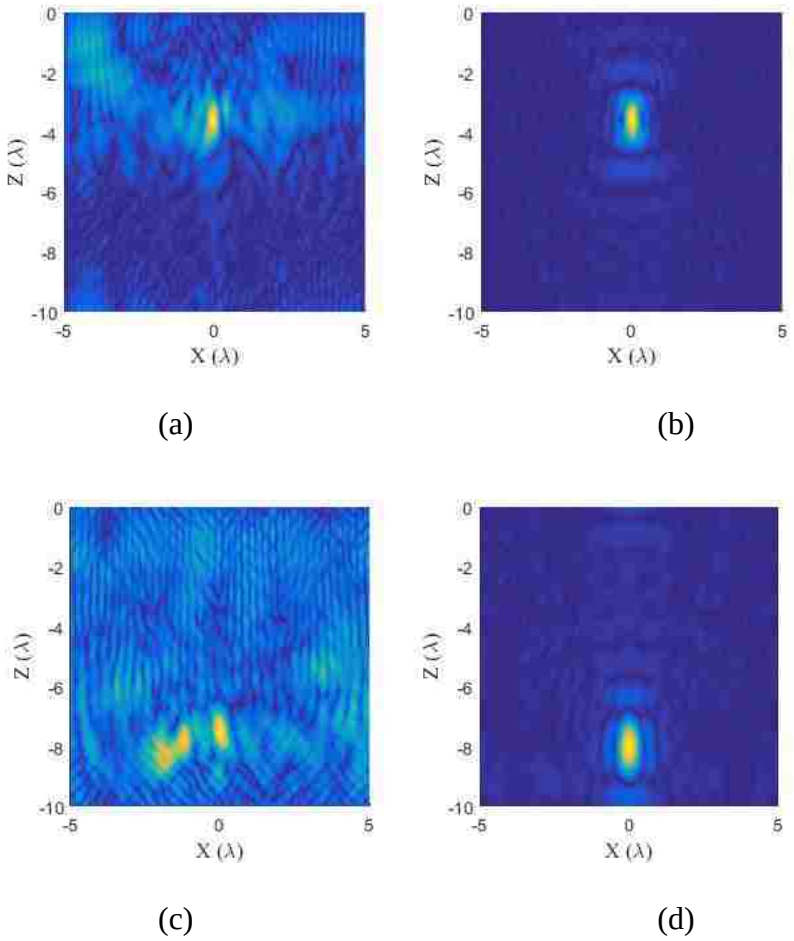

Figure 8. Simulated imaging results when *a* equals to 0.25λ and point target locates at center (a) uncompensated, standoff distance equals to 3.6λ, (b) compensated, standoff distance equals to 3.6λ, (c) uncompensated, standoff distance equals to 8λ, (d) compensated, standoff distance equals to 8λ.

Another set of simulations were performed for an off-center target with much larger maximum possible height position error. In these simulations, the point target was 3λ away from the center of scanned aperture and a was set equal to λ. Two standoff distances of 3.6λ and 8λ were considered, respectively. The results in Fig. 9 show that when a equals to λ, there is no well-defined point target any longer and the uncompensated image cannot provide any correct indication of the point target. However, when the proposed error compensation method is applied, well-defined images appear in their correct locations.

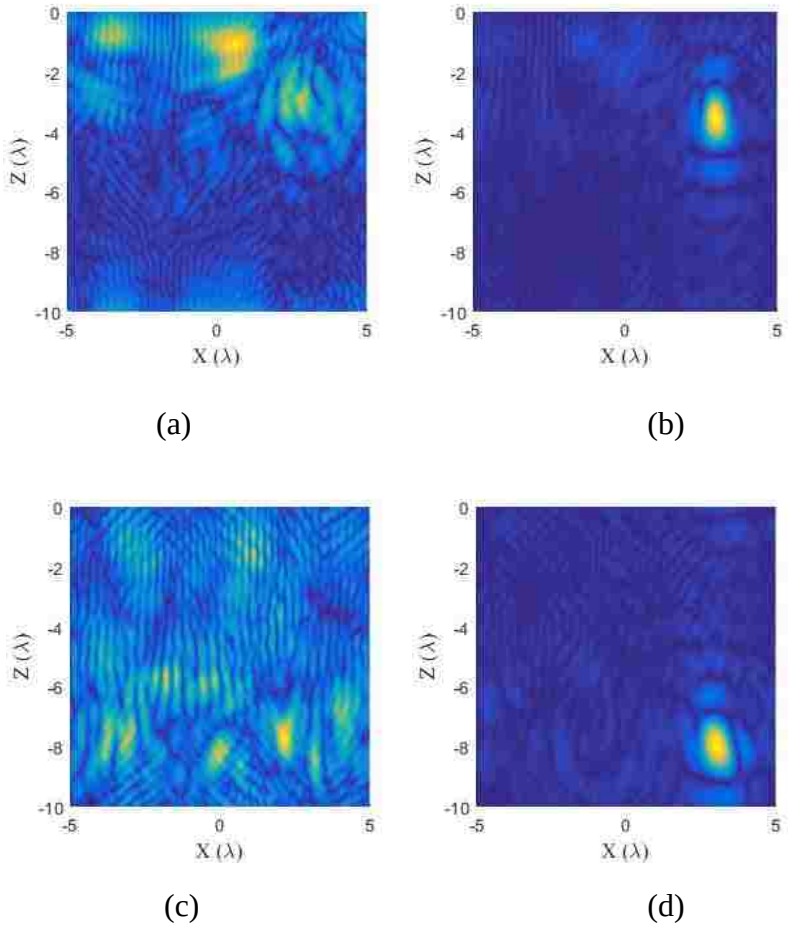

Figure 9. Simulated imaging results when a equals to λ and point target is 3λ away from center: (a) uncompensated, standoff distance equals to 3.6λ, (b) compensated, standoff distance equals to 3.6λ, (c) uncompensated, standoff distance equals to 8λ, and (d) compensated, standoff distance equals to 8λ.

4. MEASUREMENTS

4.1. MEASUREMENT SETUP

To further confirm the simulation results, a series of 1D scans were performed in the X-Band (8.2-12.4 GHz) frequency range, using an open-ended waveguide probe, as shown in Fig. 10.

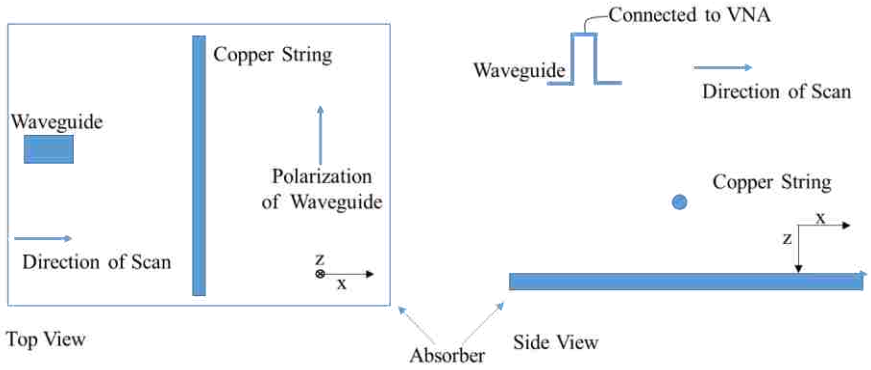

(a)

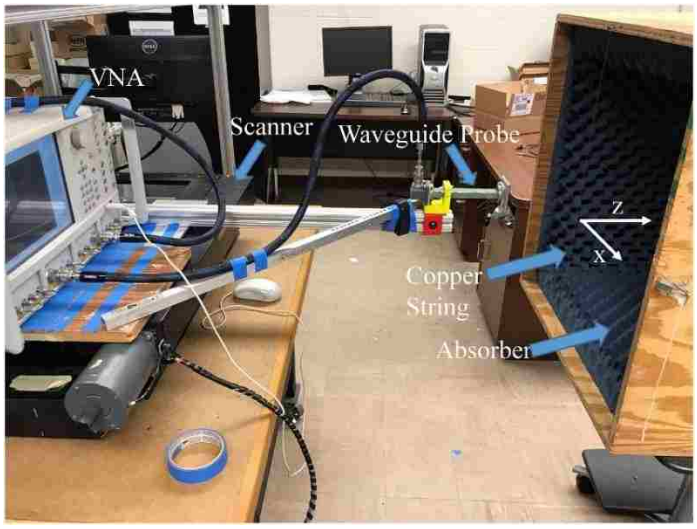

(b)

Figure 10. Experimental setup: (a) schematic, and (b) actual.

The probe was connected to an Anritsu MS4644A vector network analyzer (VNA) to measure reflection coefficient or S_{11}. The probe was mounted on and moved by a stepper-motor controlled scanner. To provide a small target with a relatively high reflection, a very thin copper string was used. Polarization of waveguide probe was aligned with the orientation of the copper string, and the scan was performed along the cross-polarized direction (i.e., *x*), so that cross-section of the copper string would be more equivalent to a point target for a 1D scan [7]. Furthermore, microwave absorbers were used to reduce unwanted background reflections. A separate scan was also performed without the copper string, to obtain the background reflection characteristics, as the reference. This information was then (coherently) subtracted from the measurements conducted with the copper string to eliminate any background reflections (including that from the probe aperture) from the measured imaging data. The length of the scan was 10λ, with a scanning step size of 1 mm (~0.03 λ) and the copper string located in the center of the scanned aperture.

To investigate the height positon error problem at a certain assumed standoff distance, a series of scans were conducted. As shown in Fig. 11, scans were performed along the *x*-direction for different standoff distances (i.e., *z*). The scanned height for *z* was the assumed standoff distance plus/minus a certain margin. The acquired data was a multidimensional matrix defined by *x*, *z* and *f*. To obtain the reflection coefficient data, s' , at the locations with height position error, a vector $(z' + \Delta z')$ was used to interpolate the original measured data along the *z*-dimension. $\Delta z'$ had a uniform PDF and was bounded by the maximum height error *a*. Furthermore, since the image evaluation metrics are a function of scan step size along *x* as well, to compare the measured results with previous

simulated results, the interpolation was also performed along the *x* direction with the same step size of 0.05λ. The height position error was random, so when calculating the evaluation metrics, the calculations were performed several times and averaged. In this study, two standoff distances were investigated, namely; 3.6λ and 8λ, the margin along *z* was 8 mm (~0.27 λ) and the step size along *z* was 0.5 mm (~0.02 λ). Since the reflection coefficient (complex) processed by the SAR imaging algorithm was interpolated from these measured reflection coefficients, to ensure the accuracy of interpolation, the distribution of magnitude and phase of the measured reflection coefficient should be almost continuous on *xz*-plane. This means the scanning step along *x*- and *z*-direction should be sufficiently small. In these measurements, the small electrical length of scanned step size along *x* (~0.03λ) and *z* (~0.02λ) are used to minimize the artificial effects caused by interpolation. In addition, spline interpolation was used to further reduce artificial effects caused by interpolation.

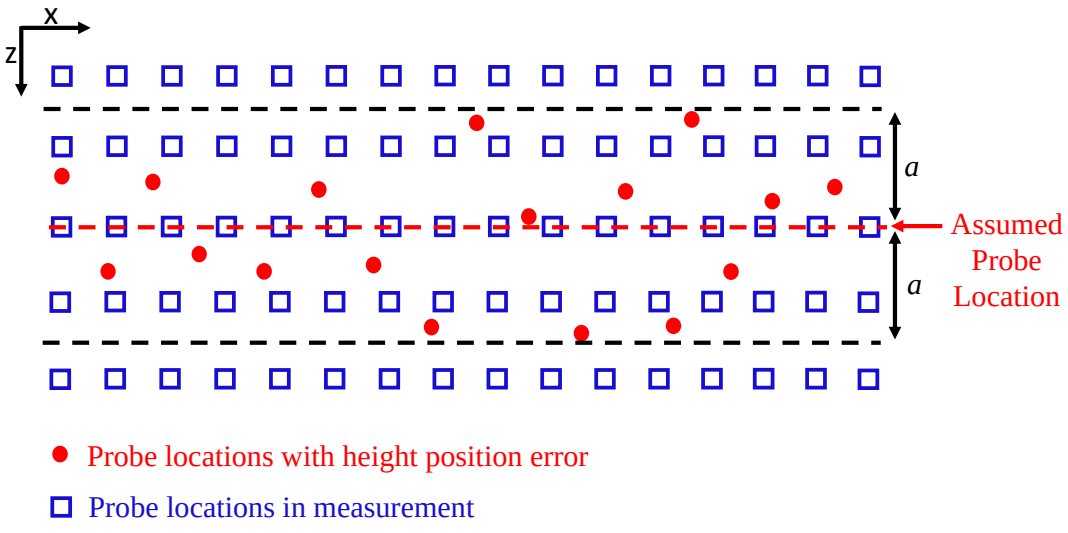

Figure 11. Method of generation of reflection coefficient data at locations with height position error (not-to-scale).

4.2. MEASUREMENT RESULTS

Simulated and measured results for spatial resolution, location bias and image error for a standoff of 3.6λ and 8λ are shown in Fig. 12. The trend of the results are consistent with previous discussions, namely; the spatial resolution decreases slightly due to the splitting effect, while the location bias and image error both increase with height position error. Furthermore, the simulation and measurement results also in good agreement. For spatial resolution and location bias, the small difference between simulation and measurement results may be caused by a small measurement error or the influence of the diameter of the copper string used, which is ~0.03λ. However, the PEC point target used in the simulations has a theoretical diameter of zero.

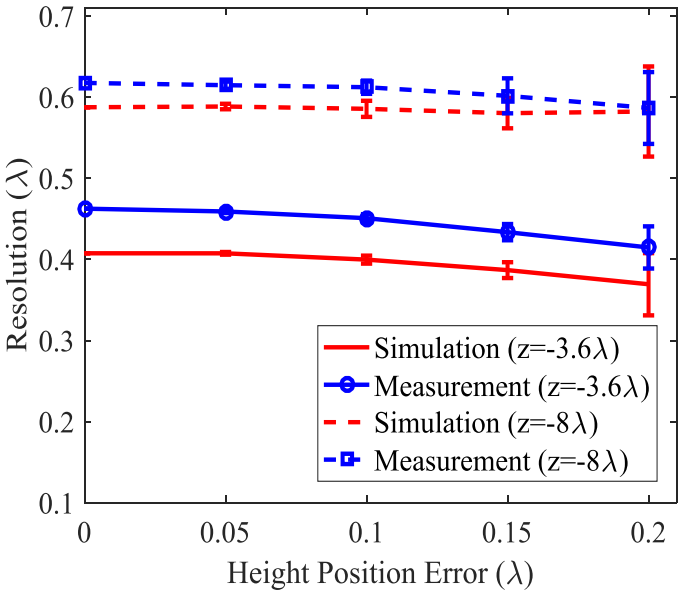

(a)

Figure 12. Evaluation metrics for standoff distance of 3.6λ and 8λ: (a) spatial resolution, (b) location bias, and (c) image error.

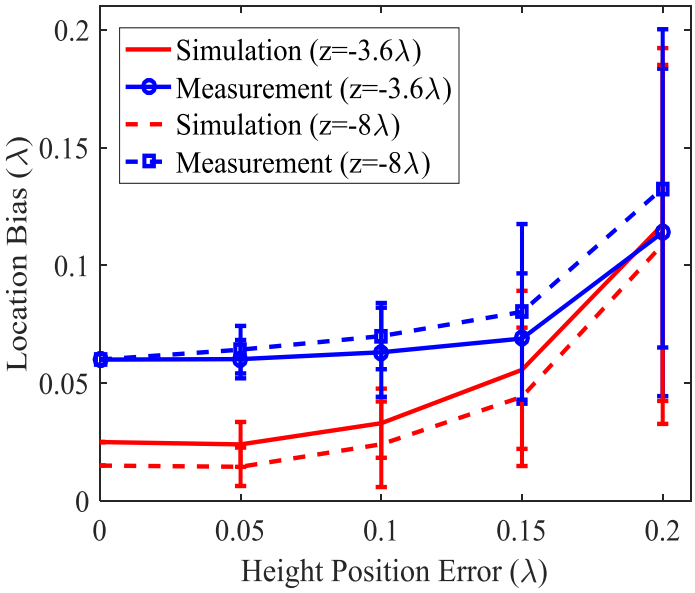

(b)

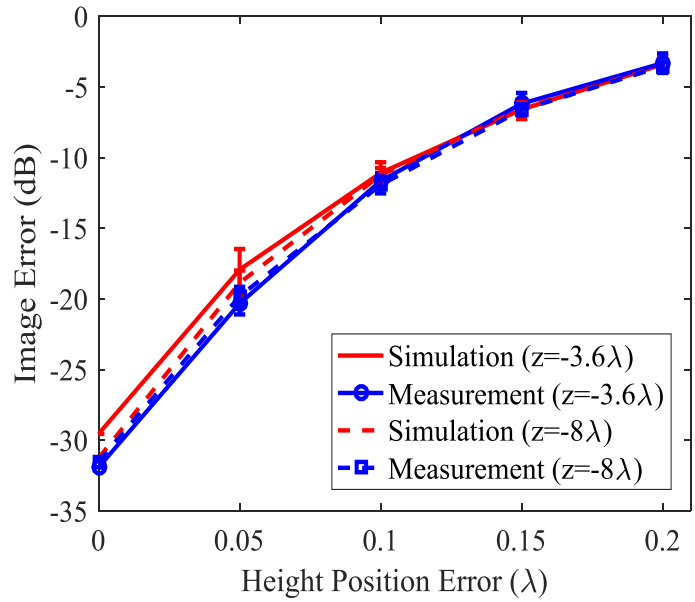

(c)

Figure 12. Evaluation metrics for standoff distance of 3.6λ and 8λ: (a) spatial resolution, (b) location bias, and (c) image error (cont.).

The compensation effectiveness of the proposed method was also examined with measurement data. The uncompensated and compensated measured imaging results are shown in Fig. 13. The results are very similar to the simulated results given in Fig. 8. This again verify the validity of proposed height position error compensation method.

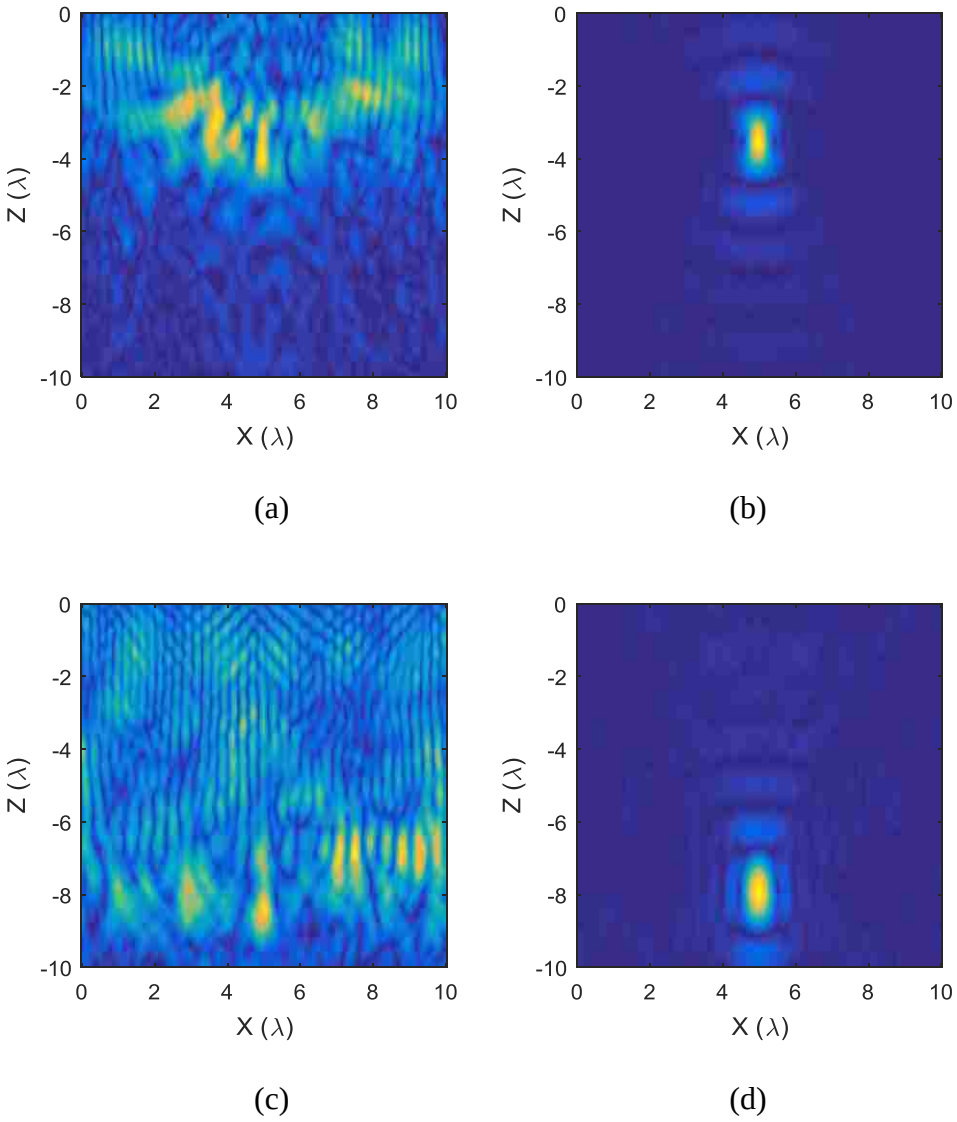

Figure 13. Measured imaging results when *a* equals to 0.25λ and point target located at center (a) uncompensated, standoff distance equals to 3.6λ, (b) compensated, standoff distance equals to 3.6λ, (c) uncompensated, standoff distance equals to 8λ, and (d) compensated, standoff distance equals to 8λ.

5. CONCLUSION

In this study, the effects of translational position error, in particular in the height direction, in microwave SAR imaging system was studied, as the height position error was determined to be the dominant factor of SAR image quality degradation. Three image quality metrics were used to quantify the effects of position error. Subsequently, an extensive set of simulations and measurements were performed. The results showed to be in good agreement verifying the effectiveness of the proposed analysis approach. Subsequently, an error compensation method was proposed and verified by both simulation and measurement. The methodology proposed in this study can be used to evaluate the feasibility or help define the required specifications of a microwave SAR imaging system for a specific application.

REFERENCES

[1] M. T. Ghasr, M. A. Abou-Khousa, S. Kharkovsky, R. Zoughi and D. Pommerenke, "Portable Real-Time Microwave Camera at 24 GHz", IEEE Trans. on Anten. and Prop., vol. 60, no. 2, pp. 1114-1125, February 2012.

[2] M. T. Ghasr, M. J. Horst, M. R. Dvorsky and R. Zoughi, "Wideband Microwave Camera for Real-Time 3-D Imaging," IEEE Trans. Antenna. Propag., vol. 65, no. 1, pp. 258–268, Jan. 2017.

[3] D. M. Sheen, D. L. McMakin, and T. E. Hall, "Three-Dimensional Millimeter-Wave Imaging for Concealed Weapon Detection," IEEE Trans. Microw. Theory Techn., vol. 49, no. 9, pp. 1581-1592, Sept. 2001.

[4] S. Kharkovsky, J. T. Case, M. A. Abou-Khousa, R. Zoughi, "Millimeter Wave Detection of Localized Anomalies in the Space Shuttle External Fuel Tank Insulating Foam," IEEE Trans. Instrum. Meas., vol. 55, no. 4, pp. 1250-1257, Aug. 2006.

[5] Y. Gao, R. Zoughi, "Millimeter Wave Reflectometry and Imaging for Noninvasive Diagnosis of Skin Burn Injuries," IEEE Trans. Instrum. Meas., vol. 66, no. 1, pp. 77-84, Jan. 2017.

[6] M. Horst, M. T. Ghasr, R. Zoughi, "Effect of Instrument Frequency Uncertainty on Wideband Microwave Synthetic Aperture Radar Images," IEEE Trans. Instrum. Meas., vol. 68, no. 1, pp. 151-159, Jan. 2019.

[7] Y. Gao, M. T. Ghasr, R. Zoughi, "Effects of Translational Position Error on Microwave Symthetic Aperture Radar (SAR) Imaging Systems", in Proc. IEEE Instrum. Meas. Technol. Conf. (I2MTC), Houston, USA. May 2018.

[8] J. T. Case, M. T. Ghasr, and R. Zoughi, "Optimum 2D Uniform Spatial Sampling for Microwave SAR-Based NDE Imaging Systems," IEEE Trans. Instrum. Meas., vol. 60, no. 12, pp. 3806-3815, December 2011.

[9] J. T. Case, M. T. Ghasr, R. Zoughi, "Optimum 2-D Nonuniform Spatial Sampling for Microwave SAR-Based NDE Imaging Systems," IEEE Trans. Instrum. Meas., vol. 61, no. 11, pp. 3072-3083, July 2012.

[10] J. T. Case, M. T. Ghasr, R. Zoughi, "Nonuniform Manual Scanning for Rapid Microwave Nondestructive Evaluation Imaging," IEEE Trans Instrum. Meas., vol. 62, no. 5, pp. 1250-1258, May 2013.

[11] L. Chusseau, P. Payet, J. Raoult, "Optimization of Near-Field Image Capture With Millimeter-Wave Bow-Tie Probes," IEEE Trans. Instrum. Meas., vol. 66, no. 1, pp. 61-68, Jan. 2017.

[12] S. Gu, K. Haddadi, A. E. Fellahi, T. Lasri, "Setting Parameters Influence on Accuracy and Stability of Near-Field Scanning Microwave Microscopy Platform," IEEE Trans. Instrum. Meas., vol. 65, no. 4, pp. 890-897, April 2016.

[13] C. J. Li, H. Ling, "High-Resolution, Downward-Looking Radar Imaging Using a Small Consumer Drone," 2016 IEEE International Symposium on Antenna and Propagation, Fajardo, Puerto Rico, June. 2016.

[14] M. Lort, A. Aguasca, C. Lopez-Martinez, T. M. Marin, "Initial Evaluation of SAR Capabilities in UAV Multicopter Platforms," IEEE Journal of Selected Topic in Applied Earth Observations and Remote Sensing, vol. pp, no. 99, pp. 1-14, Oct. 2017.

[15] M. G. Fernandez, Y. A. Lopez, B. G. Valdes, Y. R. Vagueiro, F. L. Andres and A. P. Garcia, "Synthetic Aperture Radar Imaging System for Landmine Detection Using a Ground Penetrating Radar on Board a Unmanned Aerial Vehicle", IEEE Access, vol. 6. pp. 45100-45112, Aug. 2018.

[16] G. Fornaro, "Trajectory Deviations in Airborne SAR: Analysis and Compensation," IEEE Trans. Aerospace Electronic Systems, vol. 35, no. 3, pp. 997-1009, July 1999.

[17] G. Fornaro, G. Franceschetti, Sperna, “Motion compensation errors: effects on the accuracy of airborne SAR images,” IEEE Trans. Aerospace Electronic Systems, vol. 41, no. 4, pp. 1338-1352, Dec. 2005.

IV. COMPLEX PERMITTIVITY EXTRACTION FROM SYNTHETIC APERTURE RADAR (SAR) IMAGES

ABSTRACT

Microwave and millimeter wave synthetic radar imaging (SAR) techniques are commonly used to generate high-resolution *qualitative* images showing the reflectivity (or complex permittivity) contrast in a sample-under-test (SUT). These techniques have been successfully applied for many diverse applications. However, these images lack *quantitative* information about the SUT, namely; its complex permittivity distribution. In this paper, a novel method to extract the spatial distribution of complex permittivity from SAR images is proposed. The principle of the proposed method is outlined, then verified by a series of electromagnetic simulations, demonstrating that the proposed method can accurately extract the complex permittivity. Additionally, it is shown that the results are robust with respect to most critical parameters of the SAR imaging technique. Subsequently, measurements were performed to verify the efficacy of the proposed method on two SUTs with different complex permittivities, corroborating the utility of the proposed method. Moreover, the measurement results of one of the SUTs showed that proposed method is capable of detecting local inhomogeneities with a relatively high spatial resolution. Then, a SUT with artificial defect was prepared to investigate this capability. Compared to quantitative methods based on inverse scattering techniques, this proposed method requires much less computational resources and has the potential for becoming an effective material characterization technique in the nondestructive evaluation (NDE) field.

Index Terms—Synthetic aperture radar, dielectric properties, nondestructive evaluation, materials characterization.

1. INTRODUCTION

Microwave and millimeter wave imaging techniques have been successfully applied for many applications, such as security inspection, medical imaging and nondestructive evaluation (NDE) [1]-[6]. These imaging approaches can be classified into two major categories, namely; quantitative and qualitative imaging. Quantitative imaging methods aim to solve for the complex permittivity distribution of the target. However, these methods require solving a complex inverse problem and necessitate extensive computational resources [6]. On the other hand, qualitative methods usually utilize high-resolution imaging techniques, such as synthetic aperture radar (SAR) technique, which provide contrast in the effective reflectivity of objects being imaged in a scene, a target or generally a material under test (MUT). These methods require much less computational resources and can be implemented on real-time basis rendering high-resolution 3D images [3]. However, unlike inverse imaging methods, these methods are unable to provide for the complex permittivity distribution in an MUT. Therefore, it is highly desirable to have a technique that can effectively combines the benefits of these two imaging methods.

In [7], an equivalent Gaussian beam was synthesized from a 2-dimentional (2D) raster scanned reflection coefficient to calculate local complex permittivity. However, additional processing is required to obtain the distribution of the complex permittivity, which means a weight value matrix needs to be recalculated for every different focused

spot or alternatively the MUT needs to be moved. In contrast, SAR algorithm can simultaneously (i.e., mathematically) focus anywhere on an image plane. In [8], a SAR-based method for material characterization was proposed. However, instead of providing the distribution of complex permittivity of MUT, it only estimates one complex permittivity value for the MUT.

In this paper, we expand on the development of a novel method that was initially proposed in [9], which is capable of spatially mapping the complex permittivity of MUT from SAR images. The basic foundation and preliminary results of this method were briefly outlined in [9]. The proposed method can derive plane-wave reflection coefficient at the air/MUT interface from SAR images. Then, the high-resolution 2D distribution of complex permittivity can be extracted from this plane-wave reflection coefficient. The principle and step-by-step implementation of the proposed method is described first, followed by a set of comprehensive electromagnetic simulations to verify the feasibility and robustness of the proposed method. Subsequently, relevant measurements are performed on both low and high loss MUTs to further illustrate the validity of the proposed method. Furthermore, the results also demonstrate the capability of proposed technique to detect local inhomogeneities with high spatial resolution.

2. PRINCIPLE OF THE PROPOSED METHOD

A typical setup for SAR imaging measurement is shown in Fig. 1 to help explain the principle of the proposed method. First, an antenna, commonly an open-ended waveguide (OEWG) probe, is raster scanned over an MUT to collect effective complex

reflection coefficient data. Subsequently, the ω-k SAR imaging algorithm is used to generate a series of high-resolution images of the MUT [1], [10]. The MUT in Fig. 1 is assumed to be infinitely thick (in the z-direction) so that there are no reflections form its back face and no multiple reflections within it. For the purpose of this discussion, the top surface of MUT is located at $z = 0$, and the synthetic array (measurement plane) is located at $z = h$ (xy-plane).

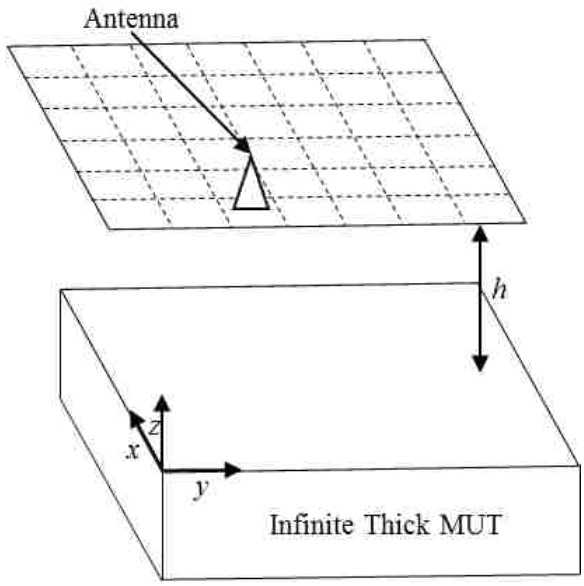

Figure 1. Measurement set up for a typical SAR imaging system.

Images generated by the SAR algorithm, when focused on MUT surface, represent spatial map of the effective (complex) reflection coefficient from the MUT. However, the obtained complex image values do not equal to the complex permittivity at the MUT surface. Thus, they can only be used for qualitative evaluation (i.e., presence of absence of an interior or surface discontinuity).

Principally, SAR algorithm back-propagates the reflection coefficient (phase) from the measurement plane to the imaging plane and focuses the wave to a pixel with a size equals to the spatial resolution, in the same manner as a physical lens. Furthermore, SAR imaging algorithm enables simultaneous focusing of the wave anywhere on the imaging plane (i.e., top surface or inside the MUT). Using this process, the wave on the focused imaging plane can ideally be considered as a plane-wave, and the complex image values should be equivalent to the plane-wave reflection coefficient at those focused planes. However, due to the approximations in the SAR algorithm (i.e., ignoring wave attenuation with distance) and influences of other factors such as antenna beamwidth, there will be some differences between the SAR complex image values and the ideal plane-wave reflection coefficient.

However, these complex image values can actually be properly corrected for to represent plane-wave reflection coefficient at the air/MUT interface. Here, an error correction coefficient, *e*, is used to relate the complex SAR image values, *i.e.*, the reflection coefficient after SAR processing, Γ_{SAR} , to the plane-wave effective reflection coefficient, Γ_{PW}, at the same plane, as shown in (1):

$$\Gamma_{PW}(x,y,z,f) = e(x,y,z,f)\Gamma_{SAR}(x,y,z,f) \tag{1}$$

Coefficient *e* is a function of measurement parameters such as frequency and standoff distance. Thus, *e* can be calculated using (2) after performing SAR imaging on a reference material with a known plane-wave reflection coefficient. Here, the scanned plane is assumed to be at $z=h$ and the imaging plane is the top surface of MUT ($z=0$).

$$e(x,y,z=0,f) = \frac{\Gamma_{PW}^{Ref}(x,y,z=0,f)}{\Gamma_{SAR}^{Ref}(x,y,z=0,f)} \tag{2}$$

where, $\Gamma_{PW}^{Ref}(x, y, z = 0, f)$ is the plane-wave reflection coefficient at the top surface of a reference material, and $\Gamma_{SAR}^{Ref}(x, y, z = 0, f)$ is the SAR processed reflection coefficient at the corresponding top surface of the same material, *i.e.* the complex image value at z=0.

If the scan configuration remains unchanged and the reference material is replaced by an MUT with an unknown complex permittivity, then the plane-wave reflection coefficient of MUT can be calculated based using (3).

$$\Gamma_{SAR(Cal)}^{MUT}(x, y, z = 0, f) = e(x, y, z = 0, f)\Gamma_{SAR}^{MUT}(x, y, z = 0, f) \quad (3)$$

where, $\Gamma_{SAR}^{MUT}(x, y, z = 0, f)$ is the complex image value of the MUT at z=0 and $\Gamma_{SAR(Cal)}^{MUT}(x, y, z = 0, f)$is the calibrated (corrected) image value of MUT at z=0. This process can then be referred to *calibration*. Ideally, $\Gamma_{SAR(Cal)}^{MUT}(x, y, z = 0, f)$ equals to the plane-wave reflection coefficient of MUT, $\Gamma_{PW}^{MUT}(x, y, z = 0, f)$, and then it can be used to extract complex permittivity of the MUT. The workflow of the proposed method is shown in Fig. 2, with the outcome of each step shown on the right.

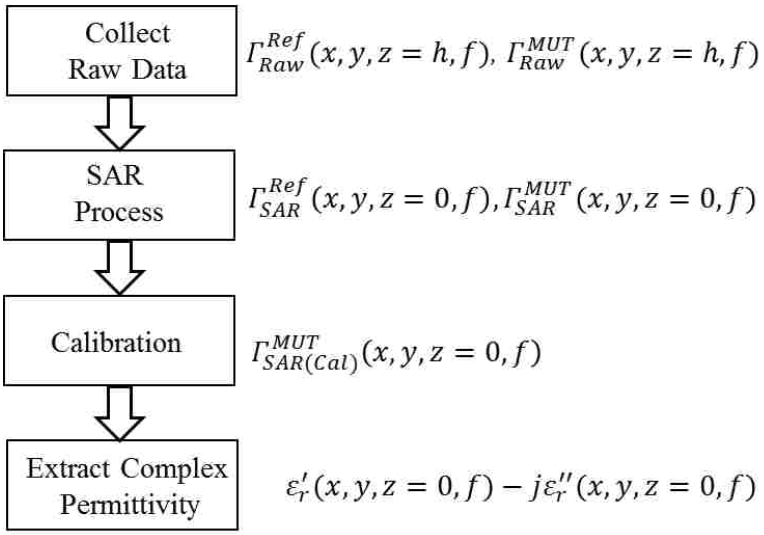

Figure 2. Workflow of the proposed method.

3. SIMULATIONS

To verify the feasibility and robustness of proposed method, a series of simulations were performed. The simulation setup was the same as that shown in Fig. 1. The antenna used in the simulations was an X-band (8.2-12.4 GHz) open-ended rectangular waveguide probe with an infinitely large flange. The reflection coefficient at the aperture of the open-ended waveguide was calculated using the algorithm given in [11]. Scanned area was 250 mm x 250 mm with a step size of 5 mm along both directions, and the standoff distance, *h*, was 100 mm. The MUT was assumed to be infinitely-extended along the lateral and depth directions. For these simulations, room temperature (23ºC) distilled water was used as the reference material, since due to its high dielectric loss factor, it can effectively represent an infinitely-thick dielectric material, in addition to the fact that its complex permittivity can be readily calculated as a function of temperature and salinity [12].

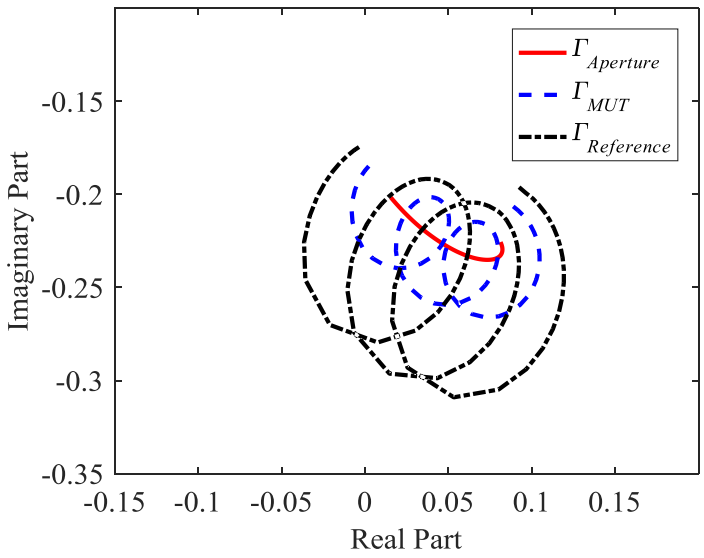

Figure 3. Calculated reflection coefficient at the waveguide probe aperture located at the center of the scanned plane when radiating into air, MUT and the reference material.

To show the details and results of the intermediate operations, an MUT with a complex permittivity of 7.5-*j*1.50 was considered. This value of complex permittivity is close to the complex permittivity of the cement paste sample that is used in the experiment, as will be shown later. Calculated reflection coefficient of the MUT, reference material and the waveguide aperture reflection (i.e. radiating into air), at the center of the scanned plane (z=100 mm), are shown in Fig. 3. To create a SAR image, the aperture reflection coefficient (which is relatively strong) must be calibrated out by coherently subtracting it from the reflection coefficient of the MUT and the reference material before SAR processing is performed. Then, the proposed procedure in Fig. 2 was implemented. Furthermore, the reflection coefficients for the MUT and the reference material also showed phase rotation as a function of increasing frequency (i.e. the *loops* feature in Fig. 3). These are the results of multiple reflections between the antenna aperture and the MUT or the reference material.

The theoretical plane-wave reflection coefficient results calculated at the surface of the MUT and the reference material (z=0 mm) are presented in Fig. 4(a). For MUT, this reflection coefficient is constant as a function of frequency (since it complex permittivity is assumed constant as a function of frequency). The small variation in the complex reflection coefficient of the reference material (i.e., distilled water) is due to the dispersion (frequency dependence) in the distilled water complex permittivity. The SAR processed reflection coefficient (i.e., complex image value) at the same location is shown in Fig. 4(b). The plane-wave and SAR-processed reflection coefficients in Figs. 4(a)-(b) are significantly different, as expected. Results in Fig. 4(b) also show phase rotation of the reflection coefficient (i.e., loop features), as a function of increasing frequency, due to the aforementioned multiple reflections that were presented in Fig. 3. Subsequently, (2) was

used to calculate the error-correction coefficient from the Γ_{PW}^{Ref} and Γ_{SAR}^{Ref} in Figs. 4 (a)-(b). Then, this error term was applied to Γ_{SAR}^{MUT} using (3) to obtain $\Gamma_{SAR(Cal)}^{MUT}$, as shown in Fig. 4c. The results show that the phase rotation effect (i.e., results of multiple reflections, as explained above) remains in the final calibrated results for $\Gamma_{SAR(Cal)}^{MUT}$. Assuming the MUT is non-dispersive (i.e., constant complex permittivity as a function of frequency) one (first-order) approach to remove this effect is to average the calibrated results over frequency, as shown by the black dot in Fig. 4(c), which makes it closely comparable to the plane-wave reflection coefficient of the MUT, Γ_{PW}^{MUT}. Alternatively, a proper SAR imaging algorithm that accounts for multiple reflections may be used (future work) to reduce this effect [13]. Finally, the complex permittivity of MUT was extracted by using the averaged reflection coefficient, $\Gamma_{SAR(CalAvg)}^{MUT}$, and the plane-wave reflection coefficient equation resulting in the calculated MUT complex permittivity of 7.39-*j*1.50, which is very close to the theoretical value of 7.50-*j*1.50. These corroborating results illustrate the feasibility of the method for the proposed use. However, since the average result of reflection coefficient was only a single point, the proposed method is only suitable for (electrically) infinitely-thick and non-dispersive materials. For dispersive (i.e., when complex permittivity is a function of frequency) and layered materials the SAR formulation must be modified to properly account for this, such as that in [13].

Furthermore, to confirm the robustness of proposed method with respect to the properties of the reference material, and the measurement parameters, a series of simulations were performed for MUTs with different complex permittivities. The dielectric constant of MUT was varied from 2 to 11 with a step size of 1 and loss tangent was assumed

to be 0.05, 0.25 and 1, respectively. Subsequently, (4) defined as below, was used to calculate the absolute percentage error (APE).

$$APE = \left|\frac{\varepsilon_{theoretical} - \varepsilon_{calculated}}{\varepsilon_{theoretical}}\right| \times 100\% \quad (4)$$

where ε can be either dielectric constant or loss factor. The simulation results are presented in Fig. 5, showing that the proposed method can accurately calculate both dielectric constant and loss factor of substantially different MUTs. This error is mainly as a result of numerical integration approximation in the open-ended waveguide model [11] and also caused by the averaging operation that used to remove multiple reflection effects, as was shown in Fig. 4c. Furthermore, the relatively large error for loss factor of low loss material ($tan\delta = 0.05$) is primarily due to this value being too small, in which case even a small error translates to a relatively large percentage error.

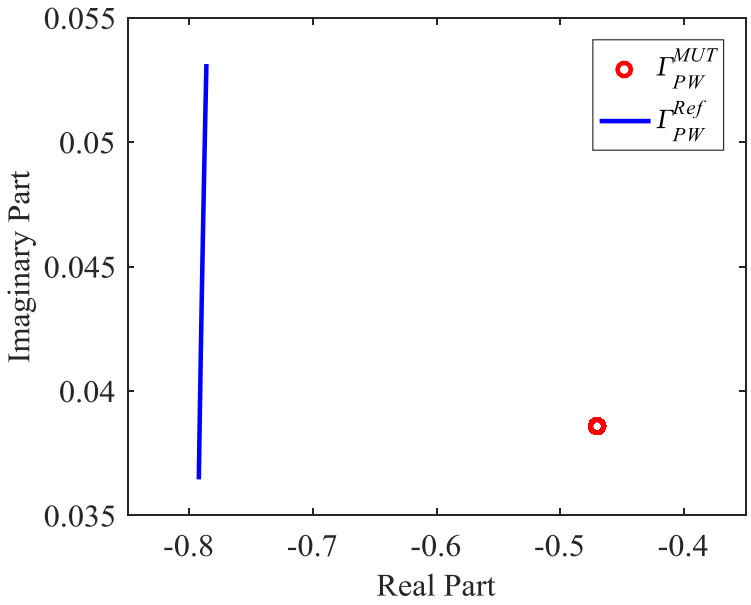

(a)

Figure 4. Calculated reflection coefficient at the center of imaged plane: (a) plane-wave, (b) SAR processed, and (c) final calibrated.

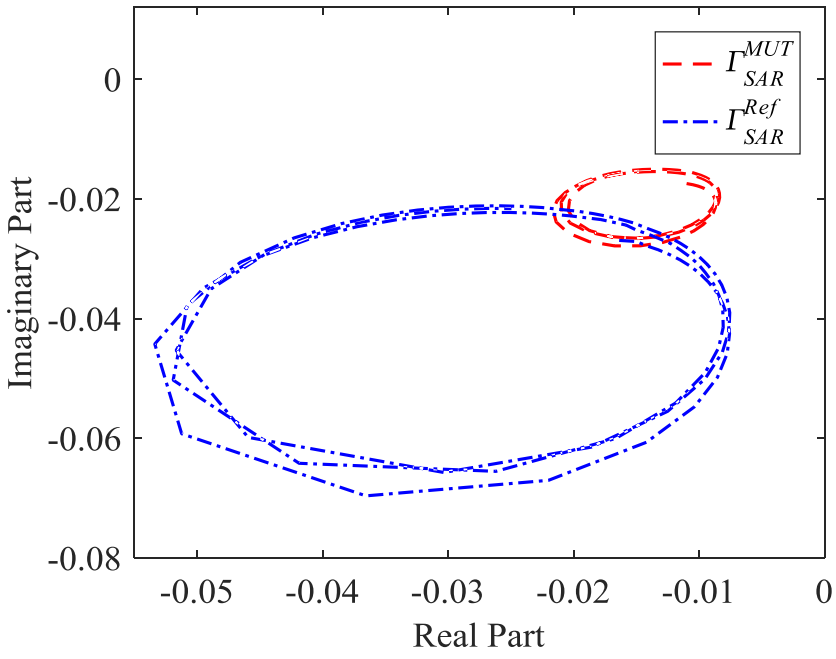

(b)

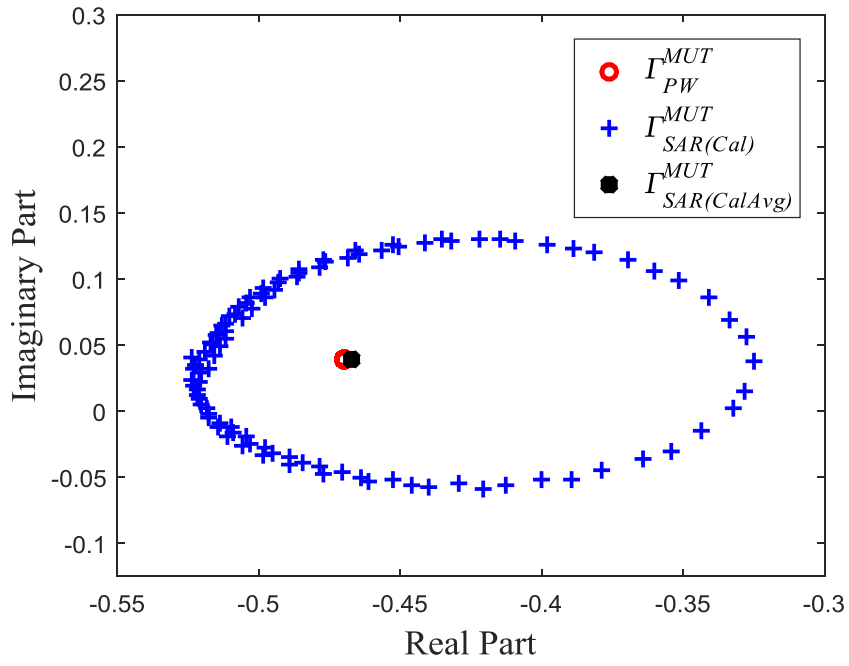

Figure 4. Calculated reflection coefficient at the center of imaged plane: (a) plane-wave, (b) SAR processed, and (c) final calibrated (cont.).

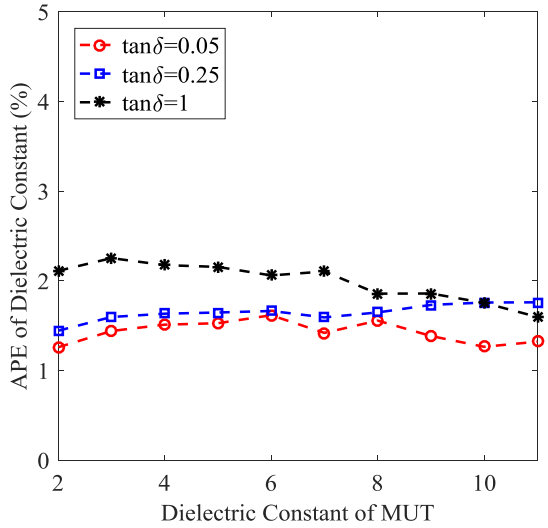

(a)

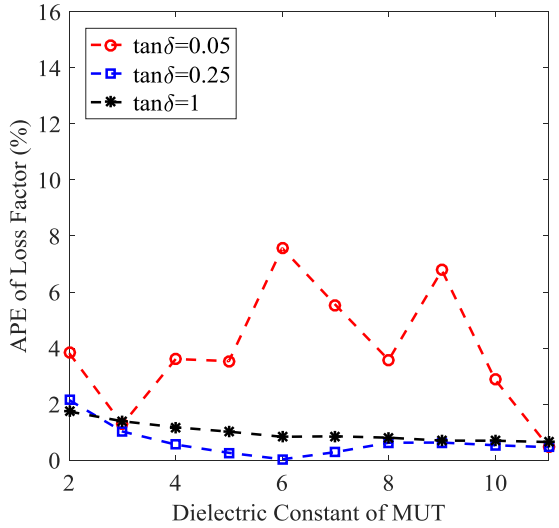

(b)

Figure 5. Errors for MUT with different complex permittivity, water is used as reference material: (a) dielectric constant, and (b) loss factor.

Subsequently, a similar set of simulations were performed by changing the complex permittivity of the reference material to a factor *k* times the complex permittivity of the distill water at room temperature, *k* values equal to 0.8 and 1.2 were simulated and the

results are shown in Fig. 6. The results indicate close similarity to those shown in Fig. 5. These simulation results show that the proposed method is not sensitive to the type of reference material used. The expected error for some of the standard complex permittivity measurements are ~5% for dielectric constant and ~10% for loss factor. The results here are in line with those values [15]-[16]. Similar simulations were also performed for different scan parameters, such as step size, scan area size, etc. The error associated with these parameters were also negligible and for brevity not shown here. These results collectively illustrate the insensitivity of the proposed method to variations in the measurement parameters, and hence its robustness.

Another factor that can lead to complex permittivity error is the standoff distance measurement error, since the standoff distance for MUT and the reference material must be the same and measured or set accurately. Two sets of simulations were performed to investigate the calculation error when there is an error in these respective standoff distances. For these simulations, the parameters were the same as those for the previous analysis in Fig. 4. Fig. 7a shows the schematic for the first set of simulations. This diagram describes the situation where the actual measured standoff distance was initially set to be the same for MUT and reference material, except where a small standoff distance measurement error exists. In these simulations, the error in standoff distance value varied from -1 mm to 1 mm with 0.1 mm step size. The results indicated that calculated complex permittivity remained fairly constant (i.e., changed in the third digit after the decimal point) to be 7.39-j1.5 for any standoff distance error values considered above. In addition, the result of complex permittivity calculation was the same as the result of the analysis in Fig. 4, which is free of standoff distance error. The results indicate that the calculation error,

caused by small standoff distance error, is negligible, when the actual standoff distance for MUT *and* reference material are the set to be the same.

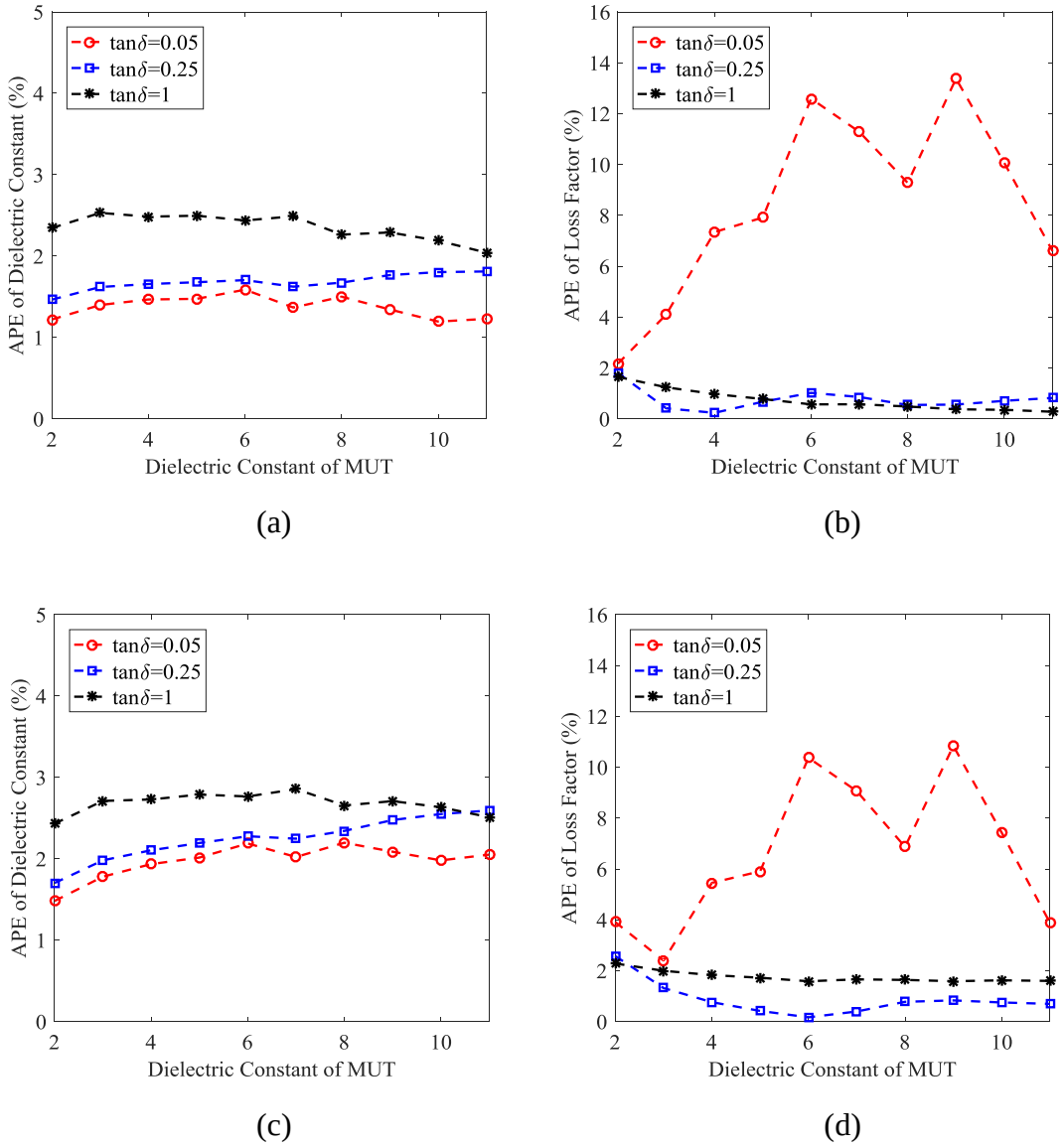

Figure 6. Errors for MUT with different complex permittivity, complex permittivity of reference material equals to *k* times the complex permittivity of room temperature distill water: (a) results of dielectric constant error when *k*=0.8, and (b) results of loss factor error when *k*=0.8, (c) results of dielectric constant error when *k*=1.2, and (d) results of loss factor error when *k*=1.2.

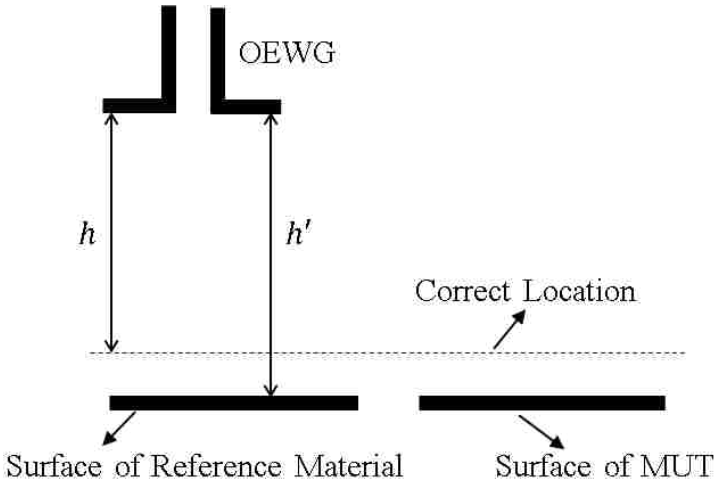

(a)

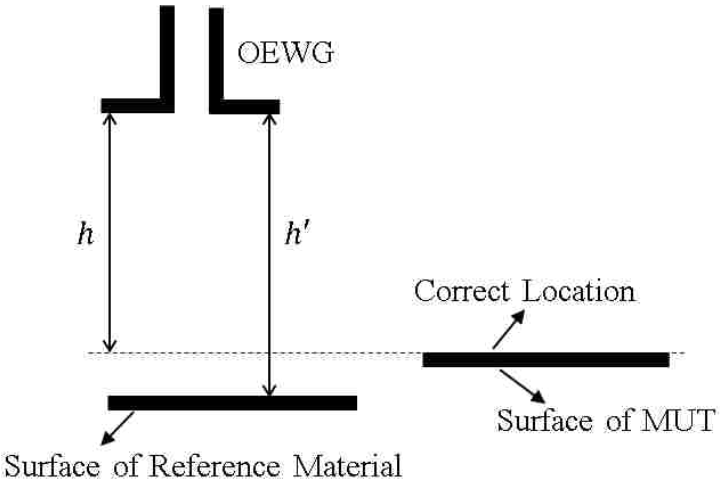

(b)

Figure 7. Schematics of situations with standoff distance error: (a) the standoff distance was the same for MUT and reference material measurement, and (b) the standoff distance was different for MUT and reference material measurement.

A second situation was investigated where the standoff distance was set at a certain distance for the MUT measurements (MUT top surface placed at the correct location), but the standoff distance of the reference material was set at a slightly different value, as shown in Fig. 7b. Then, the simulations were performed again with standoff distance error

changing from -1 mm to 1 mm (step size to 0.1 mm), and the absolute percentage error of the complex permittivity was calculated. The results are shown in Fig. 8, which indicate that the calculated complex permittivity results are indeed sensitive to the standoff distance error associated with the reference material. However, since the proposed method is insensitive to the standoff distance error in situation of Fig. 7a, therefore the standoff distance measurement does not need to be highly accurate but the MUT and reference material surface need to be at the same height and as close as possible in an experimental setup. As will be shown later, special care can be taken in the reference measurement to achieve this. The absolute percent calculation error generally increases with standoff distance error (absolute). However, since reflection coefficient is determined by both dielectric constant and loss factor, the calculation error for a single parameter may show localized non-monotonic trend, such as the loss factor calculation at ~1 mm standoff distance error where the dielectric constant calculation error is increasing but not the loss factor.

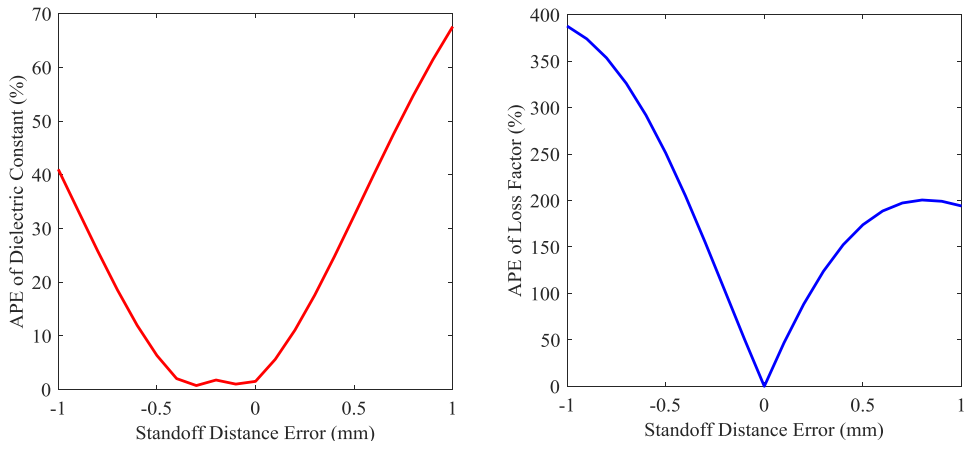

(a) (b)

Figure 8. Complex permittivity errors for MUT when standoff distance error exists: (a) dielectric constant, and (b) loss factor.

4. MEASUREMENTS AND DISCUSSIONS

4.1. LOW LOSS REFRACTORY SAMPLE

To demonstrate the efficacy of the proposed method, the first set of measurements were performed on a thick high dielectric constant but low loss refractory sample. A homogeneous 305 mm × 305 mm × 152 mm refractory sample was used as the MUT. The complex permittivity of the sample was first measured (at X-band) using the well-established open-ended rectangular waveguide method outlined in [11]. Since the loss factor of this sample was low, special care was taken as follows. The polarization of the waveguide was set to be parallel to the sample top and bottom surfaces, as shown in Fig. 9. Multiple measurements were taken along the red dash line shown in Fig. 9, with ~ $\lambda/10$ spacing at mid-band frequency. 66 measurements were performed in total and then the average complex permittivity was calculated. In addition to reduce the unwanted reflections from the probing waveguide flange, the engineered waveguide flange described in [14] was used. Finally, to further ensure accurate results, 28 modes were considered when calculating the complex permittivity [11]. Since the sample is extremely low loss, the loss factor cannot be calculated accurately, unless highly resonant cavity methods are used [15]. Thus, the loss factor was fixed at 0.005, which resulted in the measured complex permittivity to be 8.49±0.01-*j*0.005, representing ground-truth complex permittivity data.

Subsequently, a 2D scan was performed using the measurement setup shown in Fig. 10. As mentioned earlier, the proposed method is only valid for (electrically) infinitely-thick MUT. Here, since the MUT has a high dielectric constant (high reflection at the air/MUT interface), and the scanned sample side is thick, then the reflection from the

bottom is negligible and the MUT can be seen as infinite thick. An X-band waveguide was connected to an Agilent FieldFox N9926A VNA and raster scanned over the MUT to collect the complex reflection coefficient. The collected reflection coefficient data was then processed using the method outlined in Fig. 2. The scanned area was 200 mm x 200 mm with a 5-mm scan step size along both directions, and at a standoff distance of ~120 mm. These parameter settings ensure that the SAR imaging resolution is close to optimum, since the SAR spatial resolution is a function of scanning aperture size, step size and standoff distance [10]. The center of the refractory sample surface was aligned with the center of the scanned plane. The reference material consisted of the same refractory sample covered with a very thin aluminum tape. Given that the complex plane-wave reflection coefficient at the aluminum tape is -1, the desired error correction coefficient, *e*, can now be easily calculated. Given the very thin nature of the aluminum tape, the standoff distance for both the MUT and the reference samples was taken to be the same.

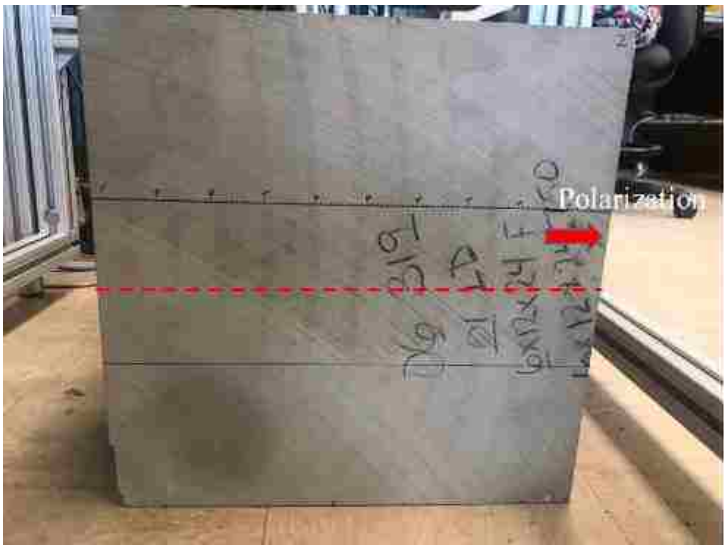

Figure 9. Refractory sample and open-ended waveguide measurement setup.

As per the earlier discussion regarding the loss factor of MUT, it was also assumed to be 0.005, hence leaving the dielectric constant to be the only parameter to be determined. In addition, to reduce the effect of edge reflections, only reflection coefficient data from a 50 mm x 50 mm area in the center of the refractory sample surface (i.e., the range of 75 mm to 125 mm along both scanned direction) was used to calculate its dielectric constant. The calculated spatial distribution of the dielectric constant is shown in Fig. 11. The average dielectric constant calculated over this area is 9.26±0.44, which is very close to 8.49±0.01 which was measured by the open-ended waveguide method.

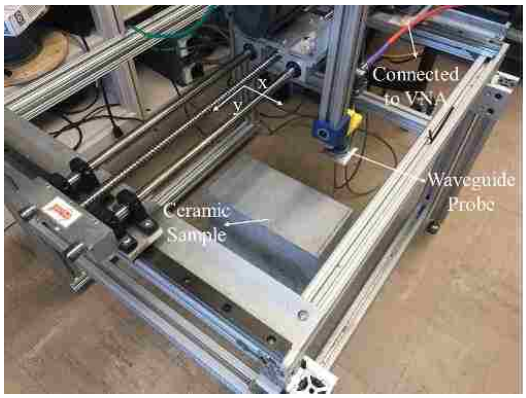

Figure 10. 2D scan setup for the refractory sample.

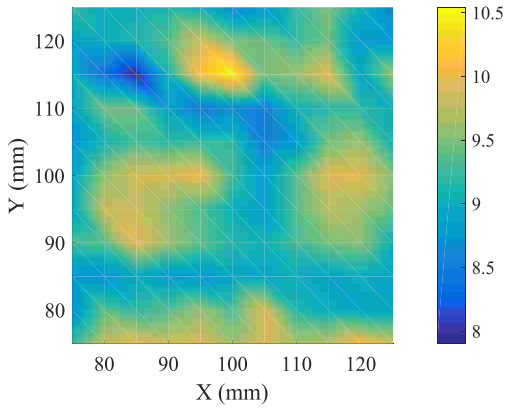

Figure 11. 2D distribution of the refractory sample dielectric constant.

4.2. LOSSY CEMENT PASTE SAMPLE

Measurements were also performed on a 200 mm × 200 mm × 190 mm cement paste sample at X-band. Cement paste is generally a lossy material, and if mixed properly it should also be a homogeneous material (i.e., without sand and rock aggregates). This is a high loss sample and we verified that wave generated by the X-band OEWG does not penetrate the full thickness of the paste sample, thus it can be considered as an infinite half-space. Near-field (contact) OEWG measurements were also performed on one side of the sample to estimate its complex permittivity using the method of [11] and [14]. This paste sample was made of cement powder and water only, and was prepared to be as homogeneous as possible. However, some inhomogeneities may remain in the form of small air voids [17]. Thus, complex permittivity needs to be measured at multiple locations to achieve good averaging. The measured side was divided into 9 sub-areas and 5 measurements were taken in each sub-area. In total, 45 measurements were taken, and the complex permittivity was calculated using the algorithm given in [11], 28 modes were used to obtain more accurate results compared to [9]. The calculated complex permittivity was then $8.01(\pm 0.67)\text{-}j1.48(\pm 0.34)$.

The 2D measurement setup for the proposed SAR technique- is shown in Fig. 12. The 2D scan was performed using an X-band waveguide on the same side, which was previously measured with the near-field OEWG method. The scanned area was 250 × 250 mm with a scan step size of 5 mm, and a standoff is ~100 mm. As mentioned earlier, aluminum tape was used for calibration. To avoid sample edge interference, only the area of x and y ranging from 50 mm to 200 mm was used in the calculations.

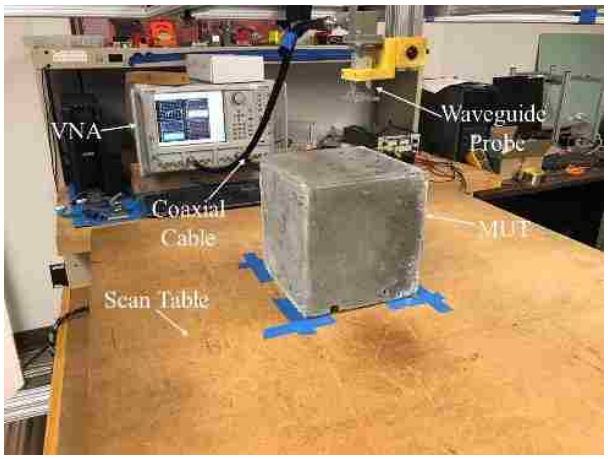

Figure 12. 2D distribution of the refractory sample dielectric constant.

Using the proposed method, the high-resolution color map image of the complex permittivity of the sample was produced, as shown in Fig. 13. The average complex permittivity over the area was 7.82(±0.60)-*j*2.17(±0.47), which is close to the results obtained from OEWG method (i.e., 8.01(±0.67)-*j*1.48(±0.34)). In addition, the SAR method results showed some areas with distinguishable complex permittivity variations, which are believed to correspond to locations where small inhomogeneities existed.

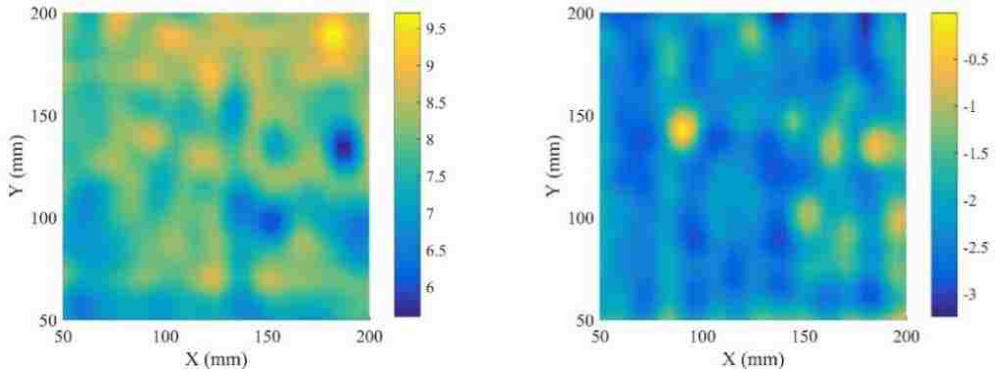

(a) (b)

Figure 13. Calculated distribution of cement paste sample complex permittivity: (a) dielectric constant, and (b) loss factor.

4.3. DISCUSSION

Because the proposed method assumes the MUT is homogenous, the calculation results will be different where local inhomogeneity exists, just as shown in Fig. 13. However, results in Fig. 13 also indicate that the proposed method is capable of distinguishing local inhomogeneities. The calculated results of complex permittivity were overlaid and aligned with the cement paste sample surface. Five locations, as the circled locations in Fig. 14, (denoted as defect locations hereafter) that showed significantly distinguishable complex permittivity were chosen for further analysis. Near-field (contact) OEWG method was used again to measure the complex permittivity at these specific locations [11]. Five measurements were taken at each location, the average results are shown in Table I together with the corresponding results calculated from the proposed SAR method at the same locations.

(a)

Figure 14. Image of calculated complex permittivity overlaid with paste sample: (a) dielectric constant, and (b) loss factor.

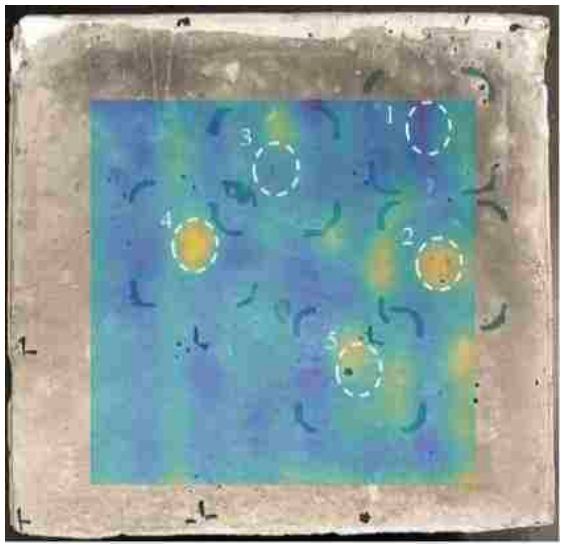

(b)

Figure 14. Image of calculated complex permittivity overlaid with paste sample: (a) dielectric constant, and (b) loss factor (cont.).

Table 1. Comparison of calculated complex permittivity.

	OEWG Method	SAR Method
Location 1	9.28(±0.10)-*j*1.37(±0.05)	9.52-*j*2.98
Location 2	4.90(±0.23)-*j*0.51(±0.11)	5.63-*j*0.40
Location 3	8.93(±0.11)-*j*1.67(±0.07)	9.12-*j*2.45
Location 4	8.30(±0.19)+*j*0.91(±0.15)	8.80-*j*0.73
Location 5	5.76(±0.32)-*j*1.15(±0.09)	6.04-*j*1.26

As shown in the previous section, the average complex permittivity calculated from open-ended waveguide method and SAR method were 8.01(±0.67)-*j*1.48(±0.34) and 7.82(±0.60)-*j*2.17(±0.47), respectively. The results show that the trend of complex permittivity changes at defect locations compare to the average complex permittivity is similar for OEWG and SAR methods. This means that for the potential defects (i.e., small voids) within the cement paste sample, the trend of change of *effective* complex permittivity is similar for these two methods. However, it must be noted that, this calculated

complex permittivity does not correspond to a physical complex permittivity of the defect or MUT (e.g., Location 4 for OEWG). This is due to the size of the defect being large considering the wavelength and thus the material at these locations do not follow the necessary homogenous assumption for both methods. Instead, it represents the local *effective* complex permittivity that can mathematically result in the same *effective* reflection coefficient. Doing so, this comparison of the obtained results from both techniques further illustrate the efficacy of the proposed techniques compare to the more established OEWG method [11], [14].

Figure 15. Paste sample with artificial defect (dowel).

Therefore, to appropriately verify the capabilities of the proposed method for evaluating localized complex permittivity, another similar paste sample with artificial defects was prepared, as shown in Fig. 15. A hole with a dimeter of ~25 mm was drilled into the cement paste sample to a depth of ~127 mm, in the middle of one of its sides. Since

the paste sample is lossy and the drilled hole is relatively deep, the defect (i.e., drilled air void) area can be seen as an infinitely thick defect in this case (unlike the small air voids in the previous sample). Subsequently, two scans were performed at X-band in a similar fashion to that outlined in Section 4.2. In the first scan the hole was left as is, representing a deep air void. In the second scan the hole was tightly fitted with a piece of cylindrical hardwood (i.e., a dowel). The scanned area was 200 mm x 200 mm with its center approximately aligned with the center of the hole, with a scanning step size of 5 mm and a standoff distance of 120 mm. To avoid sample edge interference, only the area of x and y ranging from 50 mm to 150 mm was used in the calculations. The results of complex permittivity distribution calculated by the proposed method are shown in Figs. 16 and 17.

As mentioned earlier, reflection-based material characterization method cannot calculate the loss factor accurately for very low loss MUT, such as an air void (loss factor equals zero). Thus, when calculating the complex permittivity distribution of sample with air void, the largest value of loss factor allowed was set at zero. Results in Fig. 16 show that the complex permittivity of the cement paste is similar to that used earlier. Furthermore, the complex permittivity of a 15 mm x 15 mm area within the air void region was averaged to be $1.06(\pm 0.07)\text{-}j0.02(\pm 0.05)$, which is close to the complex permittivity of air. The color map setting was set as the same for Fig. 16 and 17. The results clearly show that the complex permittivity of cement paste sample is similar for these two measurements, and the proposed method accurately captures the complex permittivity changes in the drilled area. Next, the same 15 mm x 15 mm area was selected and the averaged complex permittivity for wood in the area was calculated to be $1.74(\pm 0.11)\text{-}j0.45(\pm 0.09)$. For comparison purposes, the complex permittivity of a piece of that wood

was also measured using the plug-loaded method described in [18], to be 1.95(±0.02)-*j*0.15(±0.01). The calculation error in loss factor is caused by the calculation accuracy limitation for low loss MUTs, as mentioned earlier. These two measurements show that the proposed method can accurately calculate the dielectric constant of low loss local defect and correctly reflect the loss factor within and out of the low loss defect area.

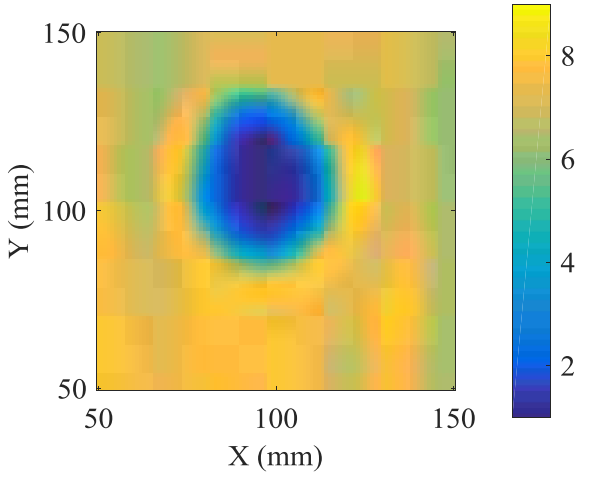

(a)

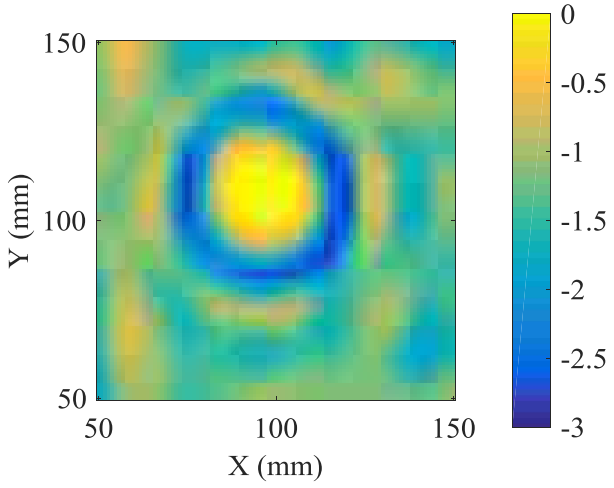

(b)

Figure 16. Calculated distribution of complex permittivity of the cement paste sample with air void: (a) dielectric constant (b) loss factor.

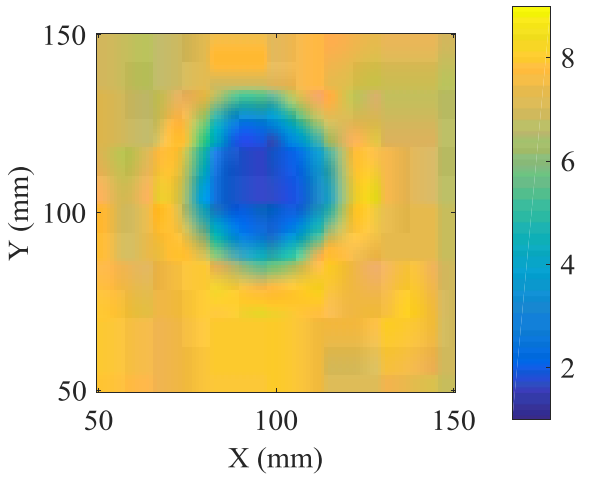

(a)

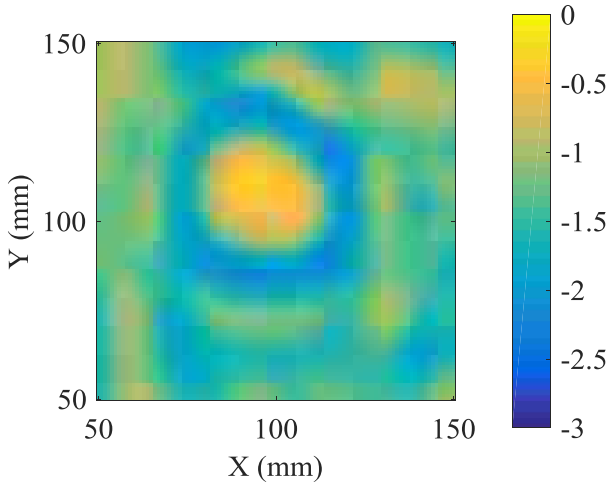

(b)

Figure 17. Calculated distribution of complex permittivity of the cement paste sample with wood: (a) dielectric constant (b) loss factor.

To also examine the capability of proposed method for evaluating lossy defects, a series of scan were performed with the top portion of the wood soaked in 15 grams of tap water. As time elapsed and the water started to naturally evaporate, a total of nine scans were performed with each being ~30 minutes apart. The calculated complex permittivity

at 30, 150 and 270 minutes after the wood had been soaked are shown in Fig. 18. The color map bounds is the same for all three cases and the calculated results clearly show that the complex permittivity changes with time.

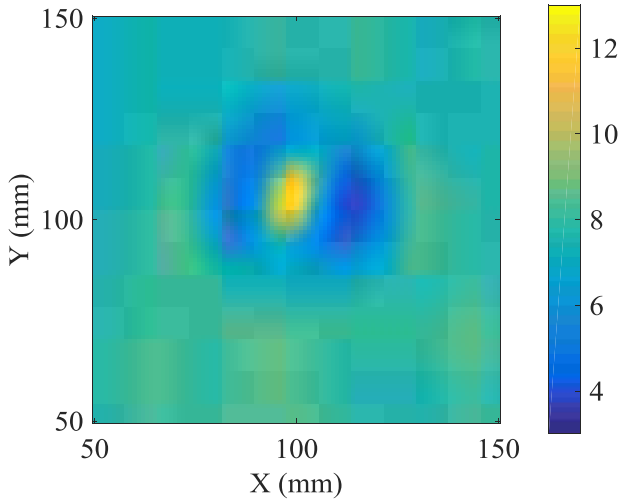

(a)

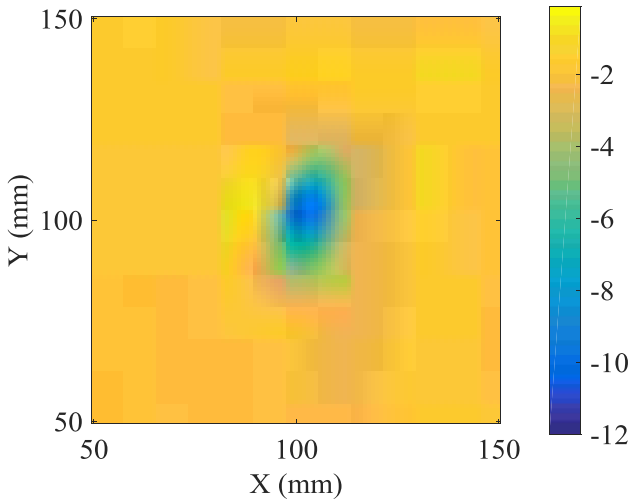

(b)

Figure 18. Calculated distribution of complex permittivity of moisten wood at different times after soaking: (a) dielectric constant, at 30 minutes, and (b) loss factor, at 30 minutes, (c) dielectric constant, at 150 minutes, (d) loss factor, at 150 minutes, (e) dielectric constant, at 270 minutes, (f) loss factor, at 270 minutes.

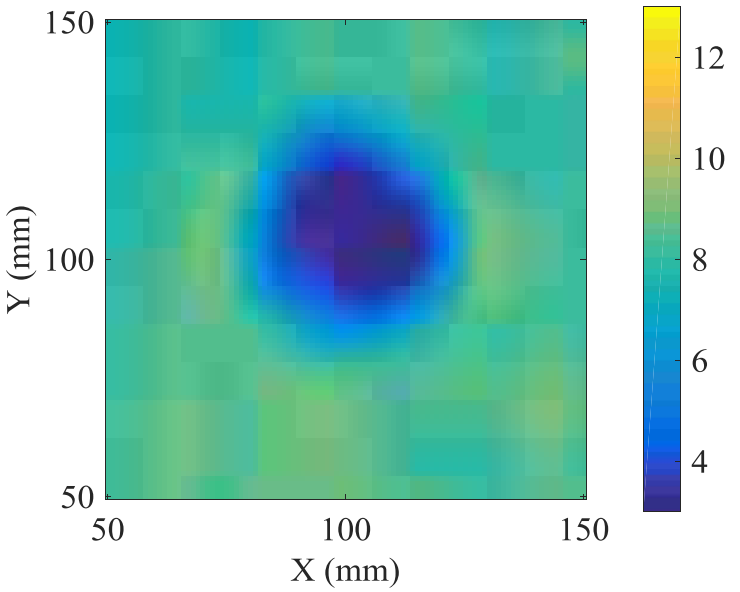

(c)

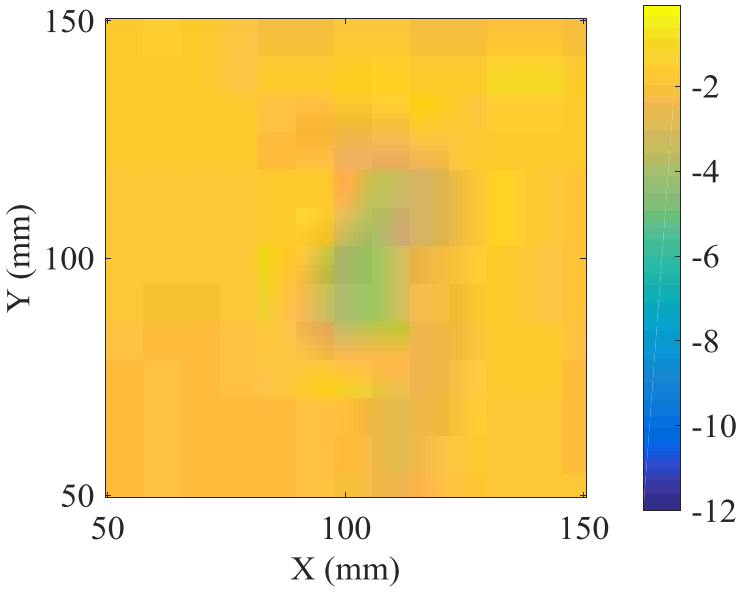

(d)

Figure 18. Calculated distribution of complex permittivity of moisten wood at different times after soaking: (a) dielectric constant, at 30 minutes, and (b) loss factor, at 30 minutes, (c) dielectric constant, at 150 minutes, (d) loss factor, at 150 minutes, (e) dielectric constant, at 270 minutes, (f) loss factor, at 270 minutes (cont.).

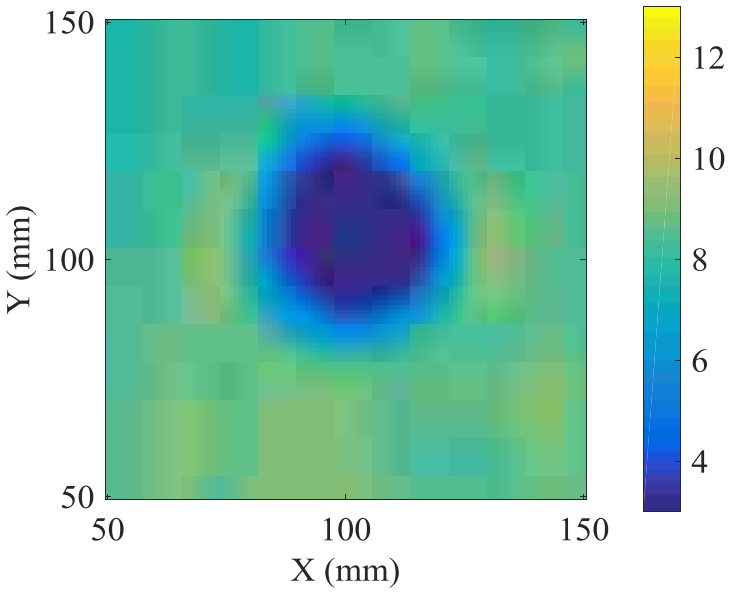

(e)

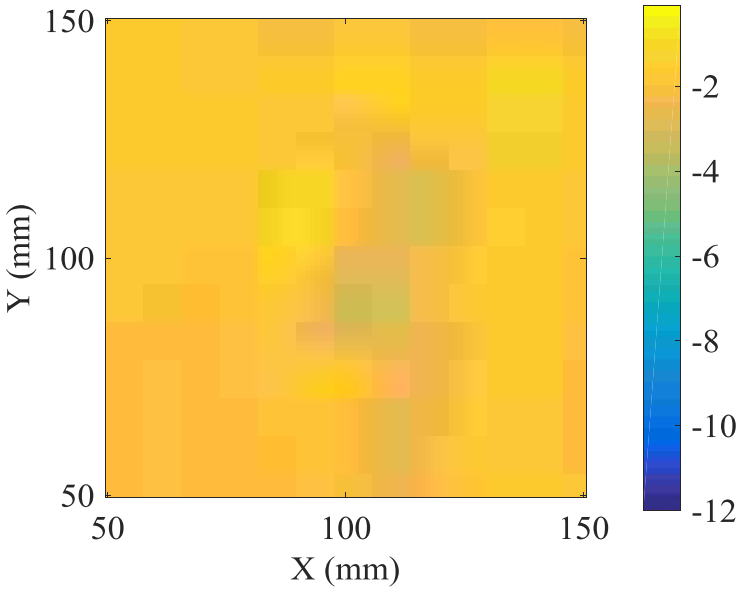

(f)

Figure 18. Calculated distribution of complex permittivity of moisten wood at different times after soaking: (a) dielectric constant, at 30 minutes, and (b) loss factor, at 30 minutes, (c) dielectric constant, at 150 minutes, (d) loss factor, at 150 minutes, (e) dielectric constant, at 270 minutes, (f) loss factor, at 270 minutes (cont.).

Again, a 15 x 15 mm area within the wood sample was selected and the average complex permittivity of this area is presented for different times in Fig. 19. The results show the permittivity and loss factor (relative) decrease with time caused by moisture evaporation, as expected. In addition, the standard deviation decreases with time as well, because the wood sample becomes more uniform in dielectric properties as its water content decreases over time.

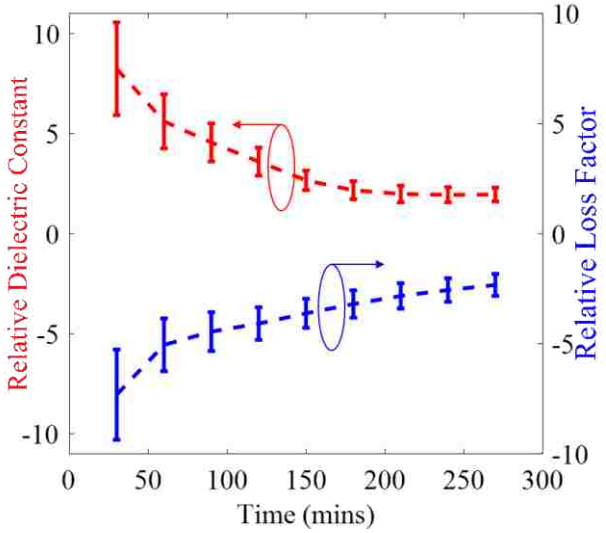

Figure 19. Calculated complex permittivity of wood sample over time.

5. CONCLUSION

Synthetic aperture radar (SAR) images only provide qualitative information, in the form of dielectric (reflection) property contrast. In this paper, a novel method was proposed to extract the complex permittivity of infinitely thick and non-dispersive MUT from SAR images. The detailed implementation approach was introduced and verified by both simulations and measurements. The simulation results showed that the proposed method

was insensitive to the type of an MUT and a reference material, and was also robust of most measurement parameters. However, its capability of calculating loss factor for low loss material in the actual measurement is limited, which is true for other reflection-based microwave materials characterization methods as well. Furthermore, the standoff distance for MUT and reference material measurement should be the same to achieve high calculation accuracy. Finally, the capability of proposed method for local defect evaluation was discussed and verified by measuring a cement paste sample with small air voids and two artificial defects.

REFERENCES

[1] D. M. Sheen, D. L. McMakin, T. E. Hall, "Three-dimensional millimeter-wave imaging for concealed weapon detection," IEEE Trans. Microw. Theory Techn., vol. 49, no.9, pp. 1581-1592, Sep. 2001.

[2] S. S. Ahmed, A. Schiessl, F. Gumbmann, M. Tiebout, S. Methfessel, and Lorenz-Peter Schmidt, "Advanced microwave imaging," IEEE Microwave Magzine, vol. 13, no. 6, pp. 26-43, Sept. 2012.

[3] M. T. Ghasr, M. J. Horst, M. R. Dvorsky, R. Zoughi, "Wideband microwave camera for real-time 3-D Imaging," IEEE Trans. Antennas Propagations, vol. 65, no. 1, pp. 258-268, Nov. 2016.

[4] T. Henriksson, N. Joachimowicz, C Conessa, J. Bolomey, "Quantitative microwave imaging for bread cancer detection using a planar 2.45 GHz system," IEEE Trans Instrum. Meas., vol.59, no. 10, pp. 2691-2699, April. 2010.

[5] N. K. Nikolova, "Microwave imaging for breast cancer,"IEEE Microwave Magazine, vol. 12, no. 7, pp. 78-94, Dec. 2011.

[6] M. Pastorino, "Microwave imaging," John Wiley & Sons, 2010.

[7] J. Y. Chung, K. Sertel, J. L. Volakis, "A non-invasive metamaterial characterization system using synthetic gaussian aperture," IEEE Trans. Instrum. Meas., vol. 57, no. 7, pp.2006-2013, July. 2009.

[8] Y. A. Lopez, M. G. Fernandez, R. Grau, F. Las-Heras, "A Synthetic Aperture Radar (SAR)-Based Technique for Microwave Imaging and Material Characterization" Electronics, vol. 7, no. 12, pp. 373-387, Dec. 2018.

[9] Y. Gao, M. T. Ghasr, R. Zoughi, "Saptial Mapping of Complex Permittivity from Synthetic Aperture Radar (SAR) Images", in Proc. IEEE Instrum. Meas. Technol. Conf. (I2MTC), Auckland, NZ. May 20-23, 2019.

[10] J. T. Case, M. T. Ghasr, R. Zoughi, "Optimum two-dimensional uniform spatial sampling for microwave SAR-based NDE imaing systems," IEEE Trans. Instrum. Meas., vol. 60, no. 12, pp. 3806-3815, Dec. 2011.

[11] M. T. Ghasr, D. Simms, R. Zoughi, "Multimodal solution for a waveguide radiating into multilayered structures-dielectric property and thickness evaluation," IEEE Trans. Instrum. Meas. vol. 58, no. 5, pp. 1505-1513, May. 2009.

[12] F. T. Ulaby, R. K. Moore, A. K. Fung, "Microwave dielectric properties of natural earth materials," in Microwave Remote Sensing Active and Passive: From Theory to Application, vol. 3. Appendix E, Norwood, MA, USA: Artech House, 1986.

[13] M. Fallahpour, J. T. Case, M. T. Ghasr, R. Zoughi, "Piecewise and Wiener filter-based SAR techniques for monostatic microwave imaging of layered structures," IEEE Instrumentation Measurement, vol. 62, no. 1, pp. 282-294, Jan. 2014.

[14] M. Kempin, M.T. Ghasr, J.T. Case, and R. Zoughi, "Modified Waveguide Flange for Evaluation of Stratified Composites" IEEE Transactions on Instrumentation and Measurement, vol. 63, no. 6, pp. 1524-1534, June 2013.

[15] R. Zoughi, "Microwave non-destructive testing and evaluation principles," Springer Science & Business Media, Feb. 2000.

[16] J. Baker–Jarvis, C. Jones, B. Riddle, M. Janezic, R. G. Geyer, J. H. Grosvenor, Jr., and C. M. Weil, "Dielectric and magnetic measurements: A survey of nondestructive, quasinondestructive, and process-control techniques," Research in Nondestructive Evaluation, vol. 7, pp. 117–136, Aug. 1995.

[17] K. Bois, A. Benally and R. Zoughi, "Microwave Near-Field Reflection Property Analysis of Concrete for Material Content Determination," IEEE Transactions on Instrumentation and Measurement, vol. 49, no. 1, pp. 49-55, February 2000.

[18] K. Bois, L. Handjojo, A. Benally, K. Mubarak and R. Zoughi, "Dielectric plug-loaded two-port transmission line measurement technique for dielectric property characterization of granular and liquid materials," IEEE Trans. on Instrum. and Meas., vol. 48, no. 6, pp. 1141-1148, December 1999.

SECTION

2. CONCLUSIONS AND FUTURE WORK

The objective of this dissertation is to advance microwave and millimeter wave reflectometry and synthetic aperture radar (SAR) imaging techniques for skin burn diagnosis. First, comprehensive analysis were performed through both simulations and measurements to illustrate the feasibility of using microwave and millimeter wave reflectometry and SAR imaging for burn degrees determination. The results showed that these techniques have the potential to distinguish healthy skin and burned skin with various severities. The fundamental principle of this diagnosis is that complex permittivity of skin is mainly determined by water content in the microwave and millimeter wave range, while the water content of healthy skin and burned skin are different. Thus, the proper knowledge of skin complex permittivity is critical for accurate electromagnetically modeling of skin. To this end, the commonly used *in vivo* skin complex permittivity measurement methods were reviewed, then a modified open-ended waveguide method was proposed to more accurately measured skin complex permittivity.

To accurately determine burn degrees through SAR imaging results, high quality images with quantitative information (i.e. complex permittivity) are necessary. In this study, the SAR imaging quality degradation effects cause by the translation position error was analyzed, and an effective compensation method was proposed to significantly improve the imaging quality. Furthermore, a novel method was proposed to extract complex permittivity from SAR imaging results. The proposed method can provide the

high-resolution distribution of complex permittivity and has the potential to be integrated with a SAR imaging system.

This work opens the gate for application of microwave and millimeter wave techniques for skin burn diagnosis. However, there are additional works that must be performed to improve the applicability of these techniques by leveraging the encouraging results in this work. First, more controlled animal and human measurements can be done to examine the feasibility in a more practical situation. Second, *in vivo* human skin permittivity for more subjects can be done in a wider bandwidth, so that a parametric model (e.g., Cole-Cole model) can be established. Third, a more proper SAR algorithm that considering the multiple reflections can be used to extend the proposed method to a general layer structure. In the end, the effects of the translational position error on extracting complex permittivity form SAR images can also be investigated.

REFERENCES

[1] World Health Organization, 2014. "Burns". [Online]. Available: http://www.who.int/mediacentre/factsheets/fs365/en/

[2] American Burn Association, 2015. "Burn Incidence Fact Sheet". [Online]. Available: http://www.ameriburn.org/resources_factsheet.php

[3] A. D. Jaskille, J. C. Ramella-Roman, J. W. Shupp, M. H. Jordan, J. C. Jeng. "Critical review of burn depth assessment techniques: part I. Historical review," J. *Burn Care. Res.*, vol. 31, no. 1, pp. 151-157, Jan. 2010.

[4] S. Monstrey, H. Hoeksema, J. Verbelen, A. Pirayesh, P. Blondeel. "Assessment of burn depth and burn wound healing potential." *Burns*, vol. 34, no. 6, pp. 761-769, Sep. 2008.

[5] F. Topfer, J. Oberhammer, "Millimeter-wave tissue diagnosis: the most promising fields for medical applications", *IEEE Microwave Magazine*, vol. 16, no. 4, pp. 97-113, May. 2015.

[6] Y. Gao, R. Zoughi, "Millimeter Reflectometry as an effective diagnosis tool for skin burn injuries." *IEEE international instrumentation and measurement technology conference proceeding*, Taipei, Taiwan, May. 2016.

[7] D. Oppelt, J. Adametz, J. Groh, O. Goertz, M. Vossiek, "MIMO-SAR based millimeter-wave imaging for contactless assessment of burned skin", *2017 IEEE MTT-S Internatioal Microwave Symposium (IMS)*, Honololu, HI, USA, June.2017.

[8] S. I. Alekseev, M. C. Ziskin, "Human Skin Permittivity Determined by Millimeter Wave Reflection Measurements," *Bioelectromagnetics*, vol. 28, no. 5, pp. 331-339, July 2007.

[9] C. Gabriel, "Compilation of the dielectric properties of body tissues at RF and microwave frequencies," July. 15. 2017. [Online]. Available: www.dtic.mil/get-tr-doc/pdf?AD=ADA303903

[10] C. Gabriel, T. Y. A. Chan, E. H. Grant, "Admittance models for open ended coaxial probes and their place in dielectric spectroscopy," *Physics in Medicine & Biology*, vol. 39, no. 12, pp. 2183-2200, Dec. 1994.

[11] N. Chahat, M. Zhadobov, R. Augustine. R. Sauleau, "Human skin permittivity models for millimeter wave range," *IET Electronics Letters*, vol. 47, no. 7, pp. 427, March 2011.

[12] Ganchev, S., N. Qaddoumi, S. Bakhtiari and R. Zoughi, "Calibration and Measurement of Dielectric Properties of Finite Thickness Composite Sheets with Open-Ended Coaxial Sensors," *IEEE Transactions on Instrumentation and Measurement*, vol. IM-44, no. 6, p. 1023-1029, December, 1995.

[13] Bakhtiari, S., S. Ganchev and R. Zoughi, "Analysis of the Radiation of an Open-Ended Coaxial Line into Stratified Dielectrics," *IEEE Transactions on Microwave Theory and Techniques*, vol. 42, no. 7, pp. 1261-1267, July, 1994.

[14] M. T. Ghasr, D. Simms, R. Zoughi, "Multimodal Solution for a Waveguide Radiating Into Multilayered Structures—Dielectric Property and Thickness Evaluation," *IEEE Trans. Instrumentation and Measurement*, vol. 58, no. 5, pp. 1505-1513, May 2009.

[15] G. L. Hey-Shipton, P. A. Matthews, J. McStay, "The complex permittivity of human tissue at microwave frequencies," *Physics in Medicine and Biology*, vol. 27, no. 8, pp. 1067-1071, Aug. 1982.

[16] D. K. Ghodgaonkar, O. P. Gandhi, M. F. Iskander. "Complex Permittivity of Human Skin in Vivo in the Frequency Band 26.5-60 GHz," *IEEE Anntenna and propagation society international symposium*, Salt Lake City, UT, USA, 2002, pp. 1100-1103.

[17] N. Tamyis, D. K. Ghodgaonkar, W. T. Wui, "Dielectric Properties of Human Skin In Vivo in the Frequency Range 20–38 GHz for 42 Healthy Volunteers, " *Proc. of the 28th URSI general assembly*, 2005.

[18] S. J-P. Egot-Lemaire, M. C. Ziskin, "Dielectric properties of human skin at an acupuncture point in the 50 - 75 GHz frequency range. A pilot study," *Bioelectromagnetics*, vol. 32, no. 5, pp. 360-366, July 2011.

[19] D. M. Sheen, D. L. McMakin, T. E. Hall. "Three-dimensional millimeter-wave imaging for concealed weapon detection." *IEEE Trans. Microw. Theory and Techn.*, vol. 49, no. 9, pp. 1581-1592, Sept. 2001.

[20] J. T. Case, M.T. Ghasr, and R. Zoughi, "Optimum two-dimensional uniform spatial sampling for microwave SAR-based NDE imaging systems." *IEEE Trans. Instrum. Meas.*, vol. 60, no. 12, pp. 3806-3815, Dec. 2011.

[21] G. Fornaro, "Trajectory Deviations in Airborne SAR: Analysis and Compensation," *IEEE Trans. Aerospace Electronic Systems*, vol. 35, no. 3, pp. 997-1009, July 1999.

[22] G. Fornaro, G. Franceschetti, Sperna, "Motion compensation errors: effects on the accuracy of airborne SAR images," *IEEE Trans. Aerospace Electronic Systems*, vol. 41, no. 4, pp. 1338-1352, Dec. 2005.

[23] M. G. Fernandez, Y. A. Lopez, B. G. Valdes, Y. R. Vagueiro, F. L. Andres and A. P. Garcia, "Synthetic aperture radar imaging system for landmine detection using a ground penetrating radar on board a unmanned aerial vehicle, " *IEEE Access*, vol. 6, pp. 45100-45112, Aug. 2018.

[24] M. Pastorino, "Microwave imaging", *John Wiley & Sons,* 2010.

[25] Y. A. Lopez, M. G. Fernandez, R. Grau, F. Las-Heras, "A synthetic aperture radar (SAR)-based technique for microwave imaging and material characterization," *Electronics*, vol. 7, no. 12, pp. 373-387, Dec. 2018.

[26] Y. Gao, M. T. Ghasr, R. Zoughi, "Spatial mapping of complex permittivity form synthetic aperture radar (SAR) images," in *Proc. IEEE Instrum. Meas. Technol. Conf. (I2MTC),* Auckland, NZ. May.20-23, 2019.

VITA

Yuan Gao was born in Heilongjiang, China. He received the Bachelor degree from Hefei University of Technology, Hefei, China, 2010 and the Master degree from Harbin Institute of Technology Shenzhen Graduate School, Shenzhen, China, in 2013, both in Electrical Engineering. He joined the Applied Microwave Nondestructive Testing Laboratory (*amntl*) at the Missouri University of Science and Technology in Fall 2015 as a Ph.D. student. In July 2019, he received his Ph. D. in Electrical Engineering from Missouri University of Science and Technology. From May 2018 to Aug. 2018, he was an EMC Design Engineering Intern with Apple. Inc., Cupertino, CA, USA. His research interests included microwave and millimeter wave imaging, antenna design, electromagnetic compatibility and materials characterization.

He was a recipient of the 2016 IEEE Instrumentation and Measurement Society Graduate Fellowship Award and 2018 IEEE Instrumentation and Measurement Technology Conference Student Travel Grant Award.